EFFECTS OF RESIDUAL STRESS AND MATERIAL GRADIENTS PRODUCED BY INDUCTION HARDENING ON ROLLING CONTACT FATIGUE

by

Hoa Ngan NGUYEN

THESIS PRESENTED TO ÉCOLE DE TECHNOLOGIE SUPÉRIEURE IN PARTIAL FULFILLMENT OF THE REQUIREMENTS FOR THE DEGREE OF DOCTORATE OF PHILOSOPHY
PH.D.

MONTREAL, AUGUST 27TH 2019

ÉCOLE DE TECHNOLOGIE SUPÉRIEURE
UNIVERSITÉ DU QUÉBEC

BOARD OF EXAMINERS

THIS THESIS HAS BEEN EVALUATED

BY THE FOLLOWING BOARD OF EXAMINERS

Pr. Philippe Bocher, Thesis Director
Mechanical Engineering Department at École de technologie supérieure

Pr. Annie Lavasseur, President of the Board of Examiners
Construction Engineering Department at École de technologie supérieure

Pr. Victor Songméné, Member of the jury
Mechanical Engineering Department at École de technologie supérieure

Pr. Salah Guenfoud, External Evaluator
Mechanical Engineering Department at University 8 mai 1945, Algeria

THIS THESIS WAS PRENSENTED AND DEFENDED

IN THE PRESENCE OF A BOARD OF EXAMINERS AND PUBLIC

JULY 17TH 2019

AT ÉCOLE DE TECHNOLOGIE SUPÉRIEURE

To love what one does is to be on the path of happiness, to be patient is to maintain love, to be persevering is to nurture confidence, to be open-minded is to approach the truth.

Hoa Ngan Nguyen

ACKNOWLEDGMENT

First and foremost, I would like to express my sincere gratitude to Professor Philippe Bocher for his supervision of this research; for all his inspiration, guidance, support, and confidence in my capacities with respect to this work. His passion and enthusiasm are contagious, and are inspiring to me, I am truly so honoured and privileged to have had him as supervisor.

I would also like to thank all Optimization of Aerospace Manufacturing Process Laboratory (LOPFA) group members for sharing friendly team moments with me. The same goes for the Mechanical Department laboratory staff for their support all through the many years I worked on this project. Special thanks to Professor Dao Thien My for his moral and material support in this experience, for his perseverance and encouragement.

I would like to thank the entire staff of the ÉTS Dean of Studies office, Mr. André Goyette and his supervisor for their understanding and all their efforts in helping me realize my dream.

Finally, I dedicate this work, in gratitude, to my father, Van Viet Nguyen; my mother, Thi Vang Tran; my daughter, Claudia My Ninh; my loving brother, Hoai Nam Nguyen; my sister, Titana Nguyen, and my nephew, Evan Nguyen for their precious time as I went through the particular experience of completing this work, and for being by my side with ever-ready help, moral support, care, affection and encouragement, all of which gave me the strength and courage to cope with the combined challenges of my academic and social life.

In short, I thank everyone who made it possible for me to complete this work.

Hoa Ngan Nguyen

Effets des gradients de contrainte résiduelle et de propriétés matériaux produits par durcissement d'induction sur la fatigue de contact

Hoa Ngan NGUYEN

RÉSUMÉ

Cette recherche a permis de mieux comprendre les effets du durcissement par induction sur la fatigue de contact de roulement (FCR) grâce à des simulations numériques par éléments finis. L'analyse par éléments finis a été développée en 3D pour estimer la charge maximale et les positions des sites de nucléation de fissure dans le cas de roulement pur au contact du cylindre. Le contact de roulement avec ou sans contrainte résiduelle de compression superficielle a été étudié et comparé. Le profil de contrainte résiduelle a été choisi pour simuler les effets d'un traitement de durcissement par induction sur un composant en acier AISI 4340 trempé à 48 HRC. Comme ce processus de durcissement génère non seulement un gradient de contrainte résiduelle dans la composante traitée, mais également un gradient de dureté (appelé région sur-revenue), les deux types de gradients ont été introduits dans le présent modèle. Des contraintes résiduelles en compression surfacique ont été générées dans la zone durcie (environ 60 HRC), des valeurs de tension ont été introduites dans la région sur-revenue, où une dureté aussi basse que 38 HRC a été définie. Afin d'estimer les charges maximales admissibles sur les cylindres en contact pour atteindre une durée de vie de 10^6 cycles, le critère de Dang Van multiaxial et une limite de fatigue en contrainte de cisaillement ont été utilisés respectivement dans les conditions hydrostatiques positive et négative, respectivement. Avec l'approche proposée, il a été montré que la composante durcie par induction avait une charge maximale admissible significativement supérieure à celle obtenue avec une composante non traitée, et il a été observé que le pic de contrainte de tension résiduelle trouvé dans la région sur-revenue limitait le facteur de durée de vie en fatigue. Plusieurs simulations ont été effectuées avec différentes profondeurs durcies et intensités de pic de contrainte résiduelle en tension dans la région sur-revenue afin de prédire leur effet sur la charge maximale admissible. Ceci permet également d'étudier la position des fissures. Il a été constaté qu'avec les hypothèses formulées dans cette étude, la profondeur durcie permettant de maximal la charge appliquée pour une vie de 10^6 cycles correspondant à une profondeur durcie d'environ 1,2 mm. La charge maximale est alors 375% supérieure à celle d'une pièce non traitée. Les résultats sont présentés en détail et discutés, et une recommandation pour le développement ultérieur du modèle est donnée.

Mots clés : induction, AISI 4340, contrainte résiduelle, dureté, couche durcie, région sur revenue, roulement, nucléation des fissures, la charge maximale, la pression maximale, cisaillement maximal de contrainte résiduelle, critère de Dang Van, limite de fatigue en cisaillement, cylindres en contact, pure roulement.

Effects of residual stress and material gradients produced by induction hardening on rolling contact fatigue

Hoa Ngan NGUYEN

ABSTRACT

This research was conducted to provide a better understanding of the effects of induction hardening on rolling contact fatigue (RCF), using a finite element analysis. The finite element analysis was developed in 3D to estimate the maximum loading and the positions of crack nucleation sites for cylinder rolling contact. Rolling contact, with or without surface compressive residual stress, was studied and compared. The residual stress profile was chosen to simulate the effects of an induction hardening treatment on a 48 HRC tempered AISI 4340 steel component. As this hardening process does not only generate a residual stress gradient in the treated component, but also a hardness gradient (called the over-tempered region), both types of gradients were introduced in the model. Residual stresses in compression were generated in the hard case (about 60 HRC), tensile values were introduced in the over-tempered region, where harnesses as low as 38 HRC were set. In order to estimate the maximum allowable loads in the rotating cylinders to target a life of 10^6 cycles, a multiaxial Dang Van criterion and a shear stress fatigue limit were used, under positive and negative hydrostatic conditions respectively. With the proposed approach, the induction-hardened component was found to have a significantly higher maximum allowable load than that obtained with a non-treated component and it was observed that the residual tensile stress peak in the over-tempered region could become a limiting factor for rolling contact fatigue life. Several simulations were run with various case depths and tensile residual stress peak intensities in the over-tempered region. The goal was to document their load performance in terms of maximum 10^6 cycles and the related locations at which cracks would appear. It was found that with the hypotheses set in this study, the case depth at which the rolling contact fatigue behaviour was maximized is around 1.2 mm and the maximum load is 375% higher than with a non-treated part. The results are presented in detail and discussed, and recommendations for further development of the model are made.

Key words: Induction hardening, AISI 4340, residual stress, hardness, case depth, over-tempering region, nucleation crack, maximal loading, maximal pressure, maximal residual shear stress, Dang Van criteria, torsional fatigue limit, cylinders in contact, pure rolling.

TABLE OF CONTENTS

Page

LIST OF TABLES

Page

LIST OF FIGURES

Page

LIST OF ABREVIATIONS

AISI:	American Iron and Steel Institute
CD:	Case-depth
CDT:	Case-depth thickness
ÉTS:	École de technologie supérieure
HRC :	Hardness Rockwell C
HV:	Hardness Vickers
LOPFA:	Optimization of Aerospace Manufacturing Process Laboratory
OT:	Overtempering
RCF:	Rolling Contact Fatigue
RS:	Residual Stress
XY:	Radial-axial plane perpendicular to surface contact and rolling direction
FEA:	Finite Element Analysis
OD:	Over-rolling direction

LIST OF SYMBOLS

$\sigma_H^{T\_RS}$	Tensile hydrostatic residual stress
$\sigma_H^{C\_RS}$	Compressive hydrostatic residual stress
$\tau_{max}^{RS\_XY}$	Maximal residual shear stress on the plane of XY
$\tau_{max}^{C\_RS\_limit}$	Maximal residual shear stress in compression limit
$\tau_{max}^{T\_RS\_limit}$	Maximal residual shear stress in tension limit
$\tau_{max}^{RS\_CD\_XY}$	Maximal residual stress of case depth in plane XY (plane of maximal shear stress due to rolling loading)
$\tau_{max}^{RS\_OT\_XY}$	Maximal residual stress of over-tempering region in plane XY (plane of maximal shear stress due to rolling loading)
F_{max}	Maximal loading
HRC	Hardness Rockwell scale, C
α	Fatigue material constant
β	Fatigue material constant
τ_e	Elastic limit (by simple torsion) (MPa)
τ_f, τ_{limit}	Torsional fatigue limit (MPa)
po	Maximum pressure (GPa)
p_o^{limit}	Maximal contact pressure limit
p_o/τ_e	Shakedown ratio value
E	Young's modulus (MPa)
μ	Poisson's coefficient
τ_{max}	Maximum allowable shear stress
σ_H	Hydrostatic stress
$d_{i,d}$	Damage degree at position i and at angular position θ
d_i	Maximum degree of damage value
$l_{i,\theta}$	Distance from each point *i* at rotation angle θ during a revolution to the Dang Van limit

l_{min}	Minimum distance of a revolution to Dang Van limit
Ac3	Finish temperatures of austenite formation

INTRODUCTION

In the automotive and aerospace sectors, gears are generally of high quality and must be high performing and provide long service life. Accordingly, once damage is observed on a gear, the latter must be replaced. It is therefore essential to predict the maximum allowable load of these gears for a given fatigue requirement. In a gear, the contact surfaces that support rolling loads can be degraded in different ways, with crack initiation being the most frequent. This degradation may result in surface spalling, and damage may occur as a result of contact fatigue between the teeth of the gear and pinion. After a certain number of rolling cycles, cracks appear on the flank surface.

To ensure long gear life, it is important to apply surface treatments on them, to improve their mechanical and fatigue properties at the contact surface. To this end, two methods can be used, namely, chemical methods (nitriding and carburation) and thermal methods, such as induction or flame. For this research, induction hardening was the chosen technique. This process uses in aeronautic field to treatment gear. The induction hardening generates a multilayer material, very hard at surface to resist the wear and contact fatigue, soft in transition layer from the surface to core to absorb the shock. The prediction of the maximum allowable loading of an induction hardening-treated gear raises the problem of modeling and analyzing the influence of residual stresses on the gear's contact fatigue resistance. With contact crack initiation being very frequent, it is also necessary to estimate the maximum allowable loading, where the first nucleation crack will be seen in the part.

The main objective of this study is to analyze the influence of induction residual stresses and material gradient on gear performance; in order to improve contact fatigue life, and predict the maximum allowable load and the nucleation crack region in the part. Currently, in induction processing, there is no procedure for predicting the influence of residual stresses on contact fatigue or their effect on the maximum allowable load. In our case, we developed a new contact fatigue analysis procedure for typical induction-treated gears. This new methodology helps predict the maximum allowable loading of the pure rolling contact which could be present at

the pitch line on the gear flank contact. This will be the first item to be validated by the model, in order to determine the optimal induction hardening recipe for use in the aeronautical safety domain.

The study begins by examining the correlation between experimental residual stress measurements and residual stress simulation. The correlation is then followed by an analysis of the effect of residual stress on the maximum allowable load for two cases: non-treated induction and treatment by induction hardening. Lastly, an analysis of the effect of residual stress and the case depth thickness is made, in order to determine pressure limits and nucleation crack conditions.

This research project is divided into two parts:
- A study of the effect of residual stress on maximum loading, for a 0.8 mm case depth and 200 MPa maximum tensile hydrostatic residual stress $\sigma_H^{T_RS}$peak;
- A study of the effect of case depth thicknesses (0.5; 0.8; 1.0; 1.2; 1.8 mm) and residual stresses (150, 200 and 250 MPa under maximum tensile hydrostatic residual stress $\sigma_H^{T_RS}$peaks) on maximal loading, with the aim of defining the pressure p_o^{limit} and maximal residual shear stress limits for a general case.

This research project studies on the prediction of maximal load as well as the nucleation crack position of induction surface materials followed by quenching and will thus help to optimize the design of heat treatment process validating tests for parts used under rolling contact fatigue conditions. The finite element analysis of the induction residual stress effect under pure rolling contact will help in predicting the maximal load and residual stress limit. It is crucial to simulate the optimization of the residual stress profile resulting from induction hardening, in order to predict and validate contact fatigue tests through an experimental test plane.

CHAPTER 1

REVIEW LITTERATURE

1.1 Introduction

This chapter presents a scientific literature review on residual stress and hardness due to induction hardening. Then, a general analysis of typical gear movements under rolling contact are described; the necessity of the pure rolling study on rolling contact fatigue and especially for the case of heat treatment by induction hardening is highlighted. This section presents an overview of rolling contact fatigue, subsurface and surface crack nucleation mechanisms, and the effect of pure rolling/sliding on rolling contact fatigue. This section mentions the method chosen for predicting RCF by multiaxial fatigue criteria. Finally, a research objective and outline was proposed.

1.2 Induction hardening

Induction hardening is a very successful method of utilizing the hardenability of a medium carbon steel to produce core strength, as well as to produce a fairly hard case that can withstand wear and maintain contact resistance. The procedure involves uniformly heating, quenching and tempering a forged gear blank to a machinable hardness of 30-38 HRC (finish-machine and cut the teeth), and induction hardening of the tooth surface to 50 HRC-65 HRC.

The induction heat treatment by quenching, which aims to improve hardness and wear resistance properties on the surface of the part, is also a green procedure (i.e. environment friendly). Induction heating systems do not burn traditional fossil fuels; induction is a clean, non-polluting process that will help protect the environment. An induction system improves working conditions for your employees by eliminating smoke, waste heat, noxious emissions and loud noise. Heating is safe and efficient with no open flame to endanger the operator or obscure the process. With this technology, an axisymmetric ferromagnetic piece is placed in a

coil, called an inductor. A frequency current is applied in the inductor to create a magnetic field around the part. The currents induced inside the treated piece produce a concentrated Joule heating on the surface layers (Savaria, 2013). After a very short period (about one second), the piece is cooled by immersion in a polymer liquid or by a shower liquid bath. Since the surface steel has been heated above the transformation temperature, Ac3, quenching at this point results in the formation of a fresh martensitic layer on the surface. This extends to a depth of up to several millimeters. A multitude of parameters in the process (power, current frequency, heating time, type of quenching, form of inductor, etc.) can be varied, thus producing different hardness and residual stress profiles.

1.2.1 Induction hardening hardness profile

A typical micro-hardness profile of a cylinder is also shown in Figure 1-1. A detailed, microscopic optical analysis of a layer of AISI 4340 steel treated by induction generally identifies three areas: a hardened zone (case depth), an over-tempering zone of low hardness and the core of the piece that is unaffected by surface treatment (Savaria, 2013).

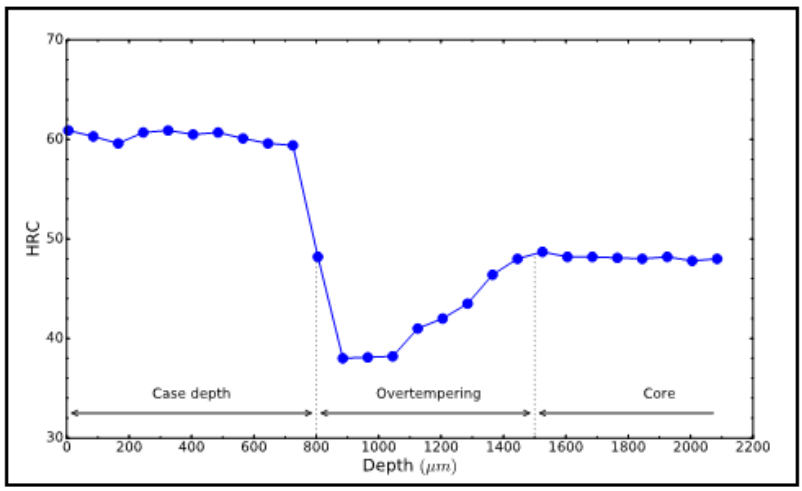

Figure 1-1 Typical hardness profile of AISI 4340 treated by induction hardening, (Savaria, 2013)

1.2.2 Residual stress resulting from induction hardening

Residual stresses due to induction hardening originate from two sources: the strong thermal gradient during heating, and the cooling creating thermal stresses and a phase change located on the surface, which causes an increase in volume (Savaria, 2013; Durban, 1997; Rudnev et al., 2003; Markegard and Kristoffersen, 2007; Grum, 2007). Thermal stresses tend to plastically deform the surface of the piece during treatment. These permanent deformations, combined with local increases in volume, create an incompatibility with the core of the piece which remains cold during induction. For the surface to remain physically bound to the core of the part, a field of compressive residual stress in depth and tensile residual stress in core is generated to respect the geometric compatibility principle. The residual stress profile shown in Figure 1-2 is conventionally observed after induction in the long gear tooth, in the tangential and axial directions.

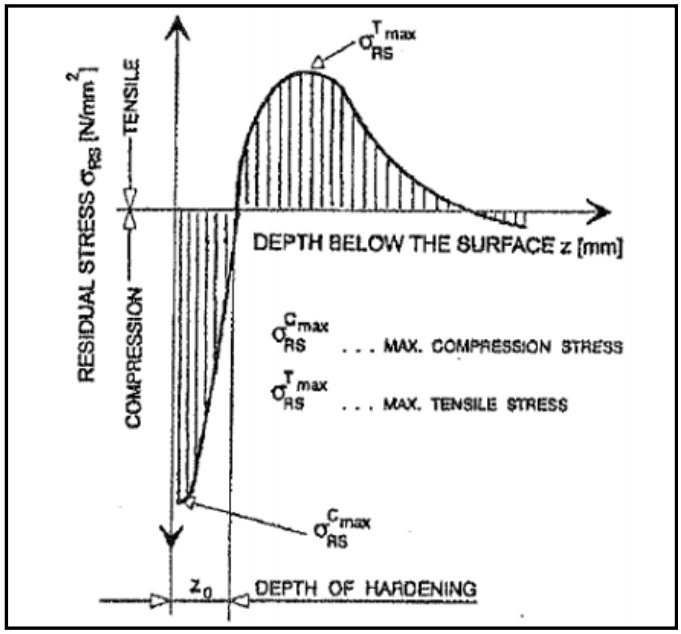

Figure 1-2 Residual stress profile after induction hardening, (Grum, 2007); Residual stress profile following depth direction z

A typical residual stress profile in Figure 1-2a is characterized by the maximum tension below the surface, the distance from the compression transition to the tension, the slope between the minimum and maximum residual stress (the gradient) and the maximum residual compression near the surface. The level of surface compression generally drops as the hardened depth increases (Savaria, 2013; Denis, 1997; Tjernbeg, 2002).

Grum et al. (2007) carried out three residual stress measurements (axial z, tangential T and radial r) on the gear by applying the induction process. They showed that once rapid quenching is complete, the tangential and axial compressive residual stresses at the surface reach about -1600 MPa and the axial tensile residual stress at the core reaches about 1000 MPa. Figure 1-3 shows the distribution of the individual residual stress components, where σ_z is the axial stress, σ_T is the tangential stress, and σ_r is the radial stress. The axial and tangential surface compression stresses rise to -1600 MPa. The axial and tangential compressive stresses at the surface are of the same amplitude at the surface. Both stresses show decreasing amplitude with an increased depth. At 20 mm, these stresses stop being compressive and become tensile, and reach maximum amplitudes of 500 MPa (σ_T) and 1000 MPa (σ_z). The radial stress is zero at the surface, but increases gradually with depth, reaching a maximum of 500 MPa.

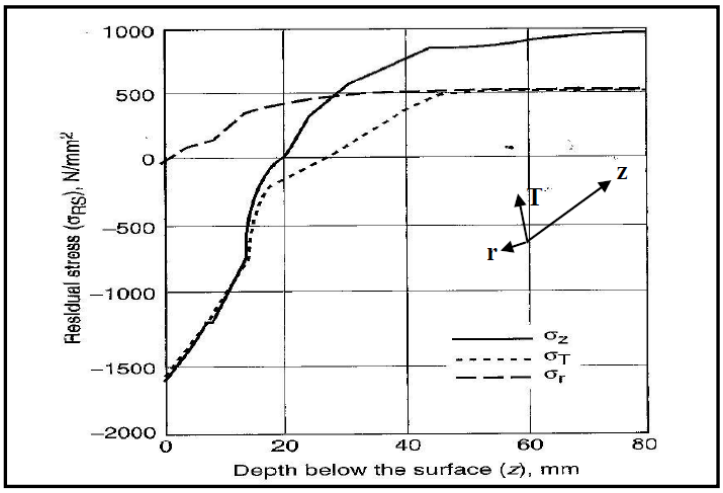

Figure 1-3 Residual stresses due to induction hardening, (Grum et al., 2007): σ_z is the axial stress, σ_r is the radial stress, and σ_T is tangential stress

Savaria (2013) studied residual stresses and their impacts on the initiation of bending fatigue cracks in aeronautical hardening by induction in AISI 4340 steel. The author measured the axial residual stress of an AISI 4340 steel cylinder with the following characteristics: 48 mm diameter with peaks in tensile residual stress (RS) of 300 to 400 MPa, a compressive RS of -500 to -600 MPa, and a case depth of 0.48 to 0.88 mm, (see Figure 1-4).

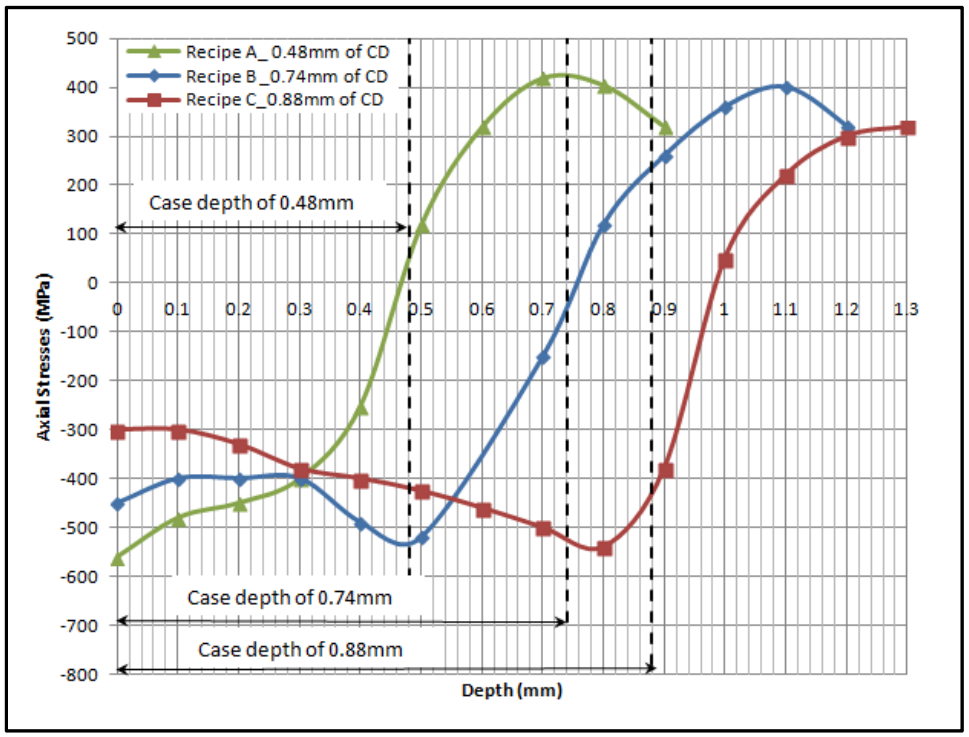

Figure 1-4 Axial residual stress measurement of some heat induction hardening recipes in an AISI 4340 cylinder: Recipe A with case depth of 0.48 mm; Recipe B with case depth of 0.74 mm; Recipe C with case depth of 0.88 mm, (Savaria, 2013)

Recipe A has significant compressive residual stresses, a relatively low gradient in the tensile transition zone. The change in stress sign is very close to the measured case depth. As for recipe B, the case depth stresses are completely compressive. C is the recipe with the lowest compression and tension in general. These recipes showed that the thicker the case depth, the more the compressive residual stress decreases.

In the RS measurements done by previous authors, the measured tensile axial residual stress reaches a maximum ranging from 400 MPa to 1000 MPa, just after induction hardening. And in the Yonetani and Isoda (1989) study on the induction hardening of steel, the axial tensile residual stress reached 600 MPa after induction. In the relaxation, a before load tensile hydrostatic residual stress of 330 MPa is reached. After a hundred thousand cycles the tensile hydrostatic stress is relaxed and stable at 250 MPa, (see Figure 1-5). Thus, the varying of tensile hydrostatic stress in this study will be limited in range of 100 to 250 MPa because the 300 MPa of tensile hydrostatic stress is also the damage limit of AISI 4340, as estimated by testing fatigue properties in LOFFA laboratory.

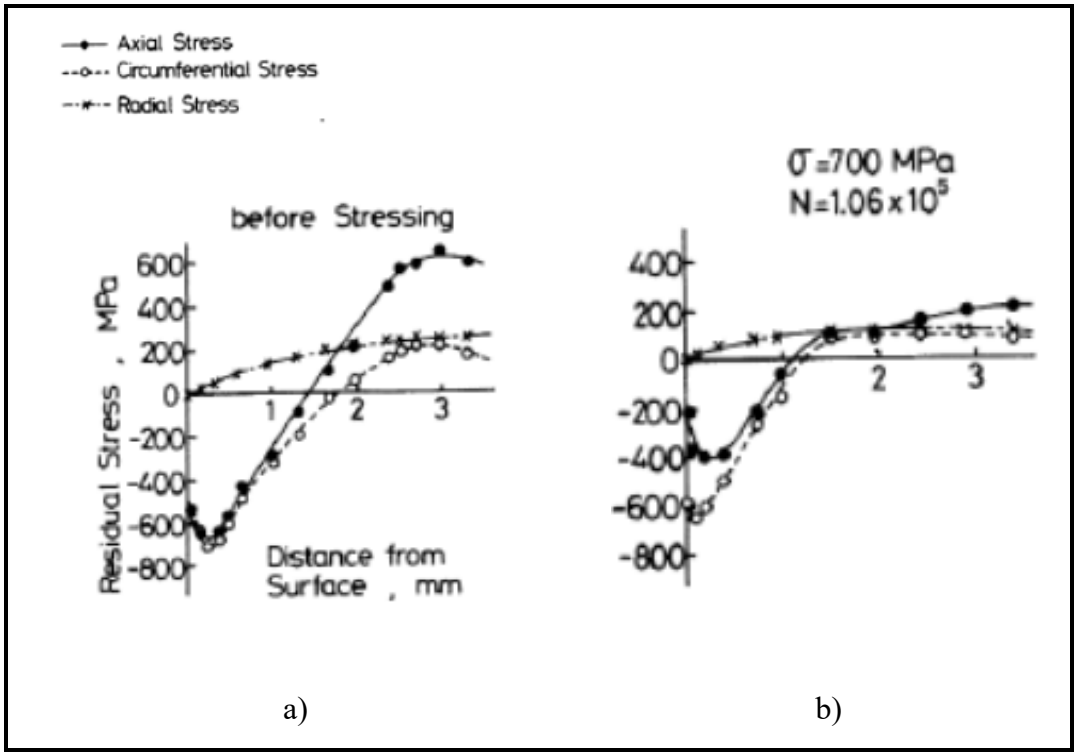

Figure 1-5 Residual stresses observed in low carbon induction hardened steel (Yonetani and Isoda, 1989): a) before stressing; b) stressing below the endurance limit

1.3 Rolling contact fatigue

The fatigue failure of the gear systems can be of different types: bending fatigue; sliding contact fatigue; rolling contact fatigue; thermal fatigue; fatigue of the other components of the transmission system (shaft, bearing, gear). An analysis of 1500 gear failures showed that bending fatigue is the most common, at 32% (Alban, 1986). However, under certain conditions, contact fatigue may become more important than bending fatigue. Contact fatigue can manifest itself in different forms depending on the applied loads and: surface pitting; spalling; and cracking, in increasing order, (Fernandes et al., 1997).

Rolling contact fatigue (RCF) can take place even after a number of cycles greater than what is usually considered as the endurance limit, that is, at above 10^9 cycles with bearing. However, with some typical gears, rollers, RCF reach with a range of 10^7 to 10^8 cycles (Glaeser et al., 1996), as the nucleation mechanisms in this range are similar (crack nucleation from hard particles or inclusions). RCF is characterized by two types of crack nucleation: surface and subsurface. Micro-pitting can be generated on the contact surface, while subsurface cracking may form and propagate, remaining invisible from the surface until large surface defects are generated (Tallian, 1982; Halme and Andersson, 2009; Sadeghi et al., 2009). Rolling contact fatigue is a type of failure at the surface and subsurface region. It is commonly found in ball or rolling bearings or metal alloys, (see Figure 1-6). It is caused by varying contact pressures on the surface of rotating contacting parts. Elastic deformations resulting from contact loading are multiaxial, and the maximum value (elastic deformation) is found at a certain distance below the surface. The fluctuating stress varies according to the loading mode and lubrication conditions, affecting the fatigue performance of the power transmission. The rolling contact stress is concentrated in a small volume of material and produces intense stress. Thus, cracks are generally initiated and concentrated in this subsurface region, where shearing is maximum, (Cavallaro, 1995). The propagation of cracks due to contact causes losses of material, in a process called "pitting" (see Figure 1-6a). The pitting is initiated in a defect: either an inclusion or a microcrack. Pitting progresses throughout the operation of the gear and forms cracks that can join and release much larger pieces of material to the surface; it is a

phenomenon called "spalling", (see Figure 1-6b). The cavities thus formed generate a large concentration of stress which favours cracking through the tooth, due to the bending load, (see Figure 1-6c).

Figure 1-6a, shows a typical example of initial pitting. Pitting has started in the dedendum section of a wide face width gear. The relative directions of surface sliding and movement of the contact load in the gear teeth affects the surface crack direction and propagation, (Alban, 1985).

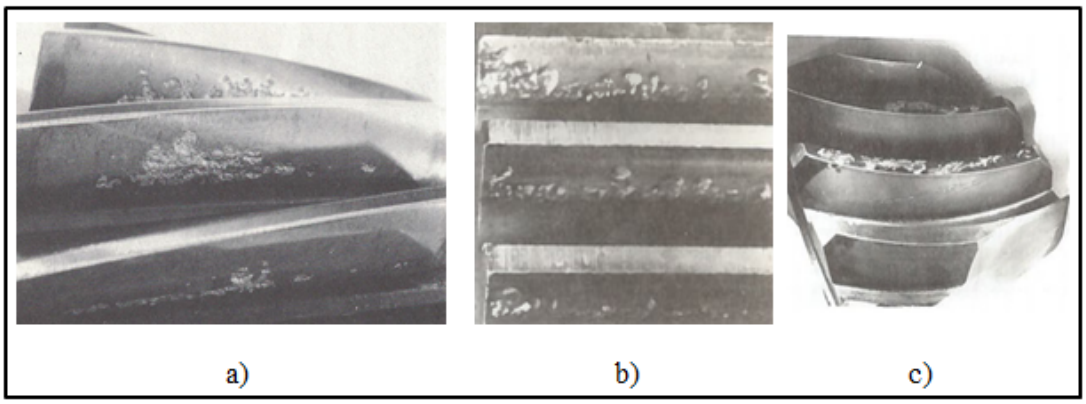

Figure 1-6 Three pitting types of rolling contact fatigue on gear: a)Initial pitting along the pitch line and just above the pitch line of helical gear teeth, (Alban, 1985); b)Destructive pitting, (Guichelaar et al., 1974); c)Spalling pitting, (Guichelaar et al., 1974)

Figure 1-6b shows destructive pitting in a gear from 1045 material heat treated to 38 HRC. The dedendum section is first to experience damage. However, as the pitting continues, the area along the pitch line usually pits away and then addendum pitting becomes prevalent (the gear from 1045 material heat treated to 38 HRC), (Guichelaar et al., 1974). Figure 1-6c shows case crushing of hardened gear which is a type of surface contact fatigue associated with cracks that originate in the core material. Cracks often propagate along the case to core boundary and then move perpendicularly to the surface. When several cracks reach the surface as shown, large elongated chunks of material are removed. Often failure may occur on one or two teeth in a pinion or gear with the remainder of the teeth undamaged, (Guichelaar et al., 1974).

In gear tooth failure, the initial pitting type is in the range of 0.4-0.8 mm in depth (Alban, 1985). It occurs in overstressed areas and can be reduced by improving the surface quality to obtain more evenly distributed polishing. Sometimes spalling occurs when the pits originate in a case-hardened pinion at or near the transition line between the hard case and the softer core material. Spalling also can be formed by destructive pittings breaking into each other, leaving wide voids (Glaeser, 1996).

With unhardened gears or medium hard gear (32 HRC), pitting often occurs as run-in processes due to bedding action (the distortion due to thermal treatment and ungrounding before meshing stay on the contact surface, including misalignment and minor profile errors). Such pitting often heals and the gear flank can become smooth again after a certain number of rotations. Pitting of this nature will tend to start during the first few hundred hours of running. The pitting could stop, in which case the pitted surface begins to polish up and burnish over.

Any pitting of hardened gears is generally a cause for alarm since the problem is unlikely to improve with time. Particularly, with case hardened gears if the case is thin or the core material weak, the case may be crushed and flaked off, leaving large pits in the surface. Case hardened gears operating at high loads and low speeds also sometimes show pitting at their pitch lines. This appears to be associated with the reversing surface sliding shear stresses which occur at this position and subject the hardened case to local fatigue failure (see Figure 1-6b), (Guichelaar et al., 1974).

1.3.1 Surface/subsurface crack initiation mechanics

As seen earlier, pitting can be of either surface origin or subsurface origin. The surface origin pits are usually associated with a thin oil film effect and surface irregularities. These could be flaws or inclusion at or very near the surface, tool marks, or imbedded debris. Figure 1-7a shows an arrow head type pit associated with surface initiated pitting, and is an example of the type of pits associated with the surface nucleation cracks.

Figure 1-7b shows subsurface cracks joint to contact surface. It shows that subsurface pits are often initiated by a maximum amplitude shear below the surface and inclusions. When a crack is formed by a frequently repeated stress, the crack propagates from the point of inhomogeneity in the material and progresses towards the surface in two directions; either parallelly or radially to the surface (see Figure 1-7b and Figure 1-8). When several radial cracks join a lateral crack below the surface, a certain volume of material will be detached, (Guichelaar et al., 1974).

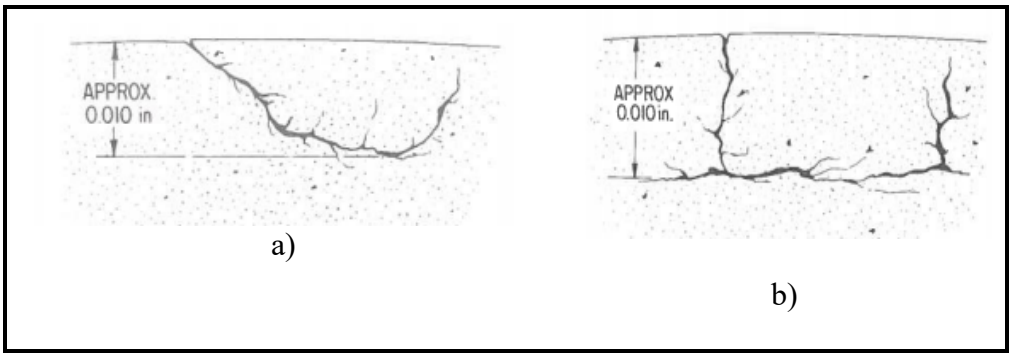

Figure 1-7 Surface/Subsurface pitting type, (Guichelaar et al., 1974):
a) Surface origin pitting; b) Subsurface origin pitting

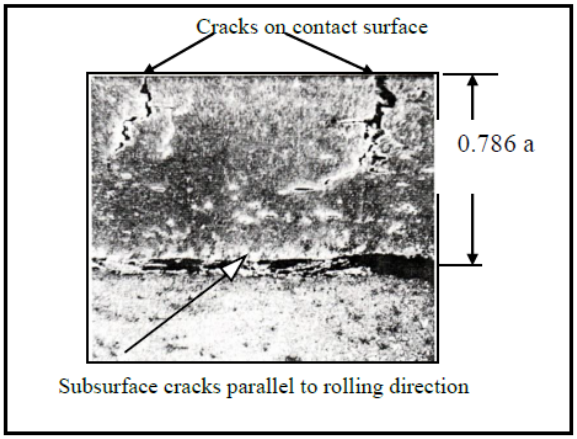

Figure 1-8 Origin crack on surface and at subsurface, (Norton, 2006)

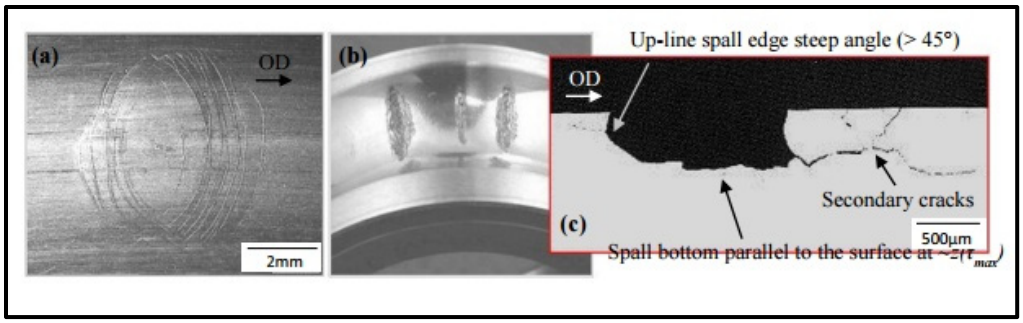

Figure 1-9 Subsurface of bearing contact fatigue of roller contact, (Crehu, 2015): a) Bearing cracks at surface; b)spalling at bearing surface; c) Spall bottom parallel to surface. OD: Over-rolling direction

As opposed to surface initiated spalls, subsurface initiated spalls present an oval shape and are most often deep, as they initiate around the maximum shear stress depth z(τ_{max}) , (see Figure 1-8). Moreover, when observed on a circumferential cross section they present steep angled edges and a flat bottom, which is mostly parallel to the surface, (see Figure 1-9c). Subsurface initiated spalls tend to propagate in the direction of rolling and secondary cracks preferentially develop on the down-line spall edge, (Crehu, 2015).

1.3.2 Pure rolling contact effect on nucleation crack region

To better understand this mechanism, analysis of the stresses, which is a prerequisite for fatigue analysis, must be done. Gear tooth stresses have been analyzed by many researchers. When gear pinion teeth are in action, the teeth roll and slide against each other in the meshing. This creates sliding contacts between the surfaces. The meshing movement generates normal and tangential forces that induce compressive and shear stresses at points in repetitive contact. When the gear is in engagement contact with the pinion, each point of contact is considered as the contact point of two parallel cylinders in contact with their equivalent radii of curvature. This section summarizes the pure rolling contact effect on gear nucleation cracks. This study designed a parallel cylinder model to simulate pure rolling at the gear pitch line.

1.3.3 Surface motion analysis

When the wheel and pinion fit together, they produce contact points on the action line as a base circle (see Figure 1-10). The teeth number decides a half angle of teeth, θ. In the tangent line with base circle, a distance of a correspondent circumference segment L is the distance from the point in base circle to involute line (gear form). The direction of the force acting at the contact point of the gears with involute curves is constantly along the common tangent (z).

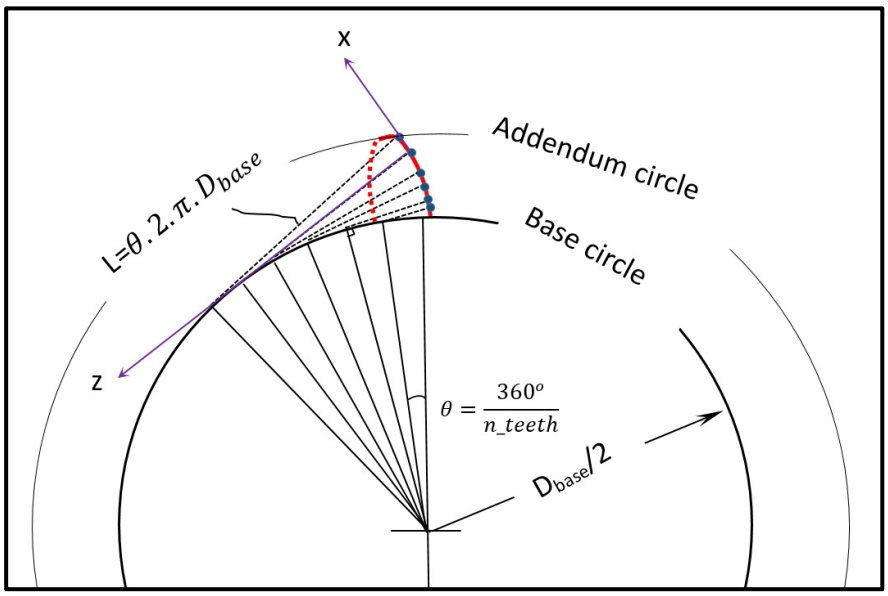

Figure 1-10 Base circle and involute line of gear

Depending on the position of the contact points, the surface movement can be in the form of two actions: rolling and sliding. Pure rolling creates normal pressure and pure sliding produces friction on the contact surface. At the pitch line, there is only pure rolling, while elsewhere, there is a combination of rolling and sliding.

When observing some cases of surface wear, it can be noticed that there are two distinct abrasive surface regions on the gear tooth flank, (see Figure 1-11a) and an intact surface in the middle. The intact surface is adjacent to the pitch line. It can thus be deduced that the abrasive surfaces are caused by sliding, combined with the rolling effect, and that the neighbouring

surface of the pitch line is intact because there is only pure rolling around it. Figure 1-11b shows some representative contact points in the flank tooth: A, B, C, D, and E (point C is the point of the pitch line). There is only pure rolling at the primitive line (point C) while at other points (A, B, D, E); there is a combination of rolling and sliding.

In other words, the pure rolling is based on point C, which forms a kind of normal parabolic pressure at the contact point, and at other representative points. The contact pressure forms an inclined parabolic pressure, due to the rolling and sliding combination of normal pressure distribution (p (x)) and slip (q (x)), along rolling direction (x).

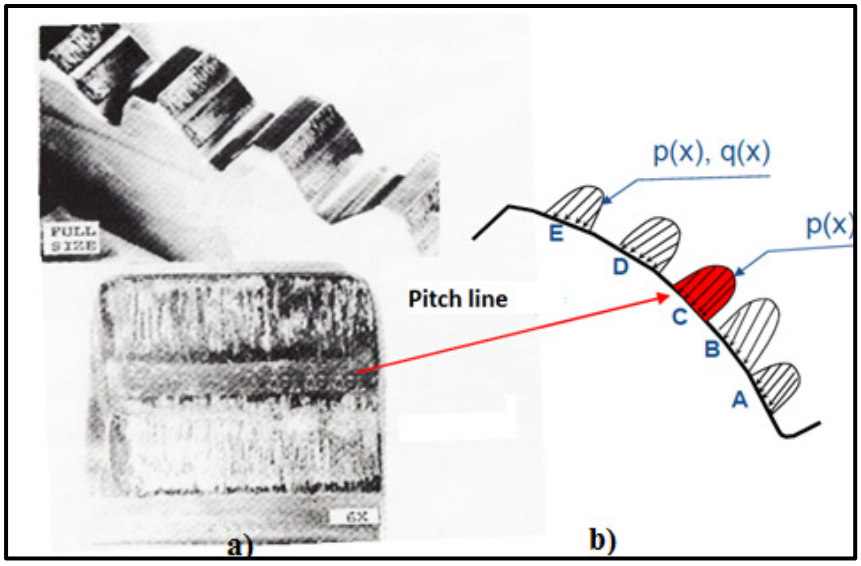

Figure 1-11 Abrasive areas in the vicinity of pitch line at tooth flank in motion: a) wear at pitch line; b) rolling and sliding combination along contact line, (Alban, 1986)

The normal pressure p(x) and sliding q(x) equation is presented by Coulomb's law expressed by a friction coefficient, μ:

$$q(x) = \mu . p(x) \tag{1.1}$$

where x is the distance from the contact center to the end of the contact width in the rolling direction, $q(x)$ is the sliding at the contact surface, and $p(x)$ is the normal pressure at the

contact surface. In this study, the pure rolling point at the contact line was investigated by a similar approach using cylinders in contact.

1.3.4 Rolling contact cylinders modeling

Almost all methods regarding static contact stress are based on the analytical solution of Hertz (1881). Since the Hertz contact stress is calculated in the case where only normal pressure is present, it is a static stress. The stresses at the contact point are calculated by Hertz's theory. It is assumed that contacts between a pair of gear and the pinion teeth are represented by two parallel cylinders in contact**, (**see Figure 1-12). In this study, which examines the influence of the residual stress profile on rolling fatigue contact, the pitch point was chosen with a pure rolling effect and a residual stress profile that can enable understanding of how to prevent wear by rolling contact fatigue. Figure 1-12 shows the concept of converting contact gears to two parallel cylinders at contact at pitch point, where F_N is the normal load, p_0 is the maximal pressure at the center contact, a is the semi width contact length, R is the radii of contact cylinder.

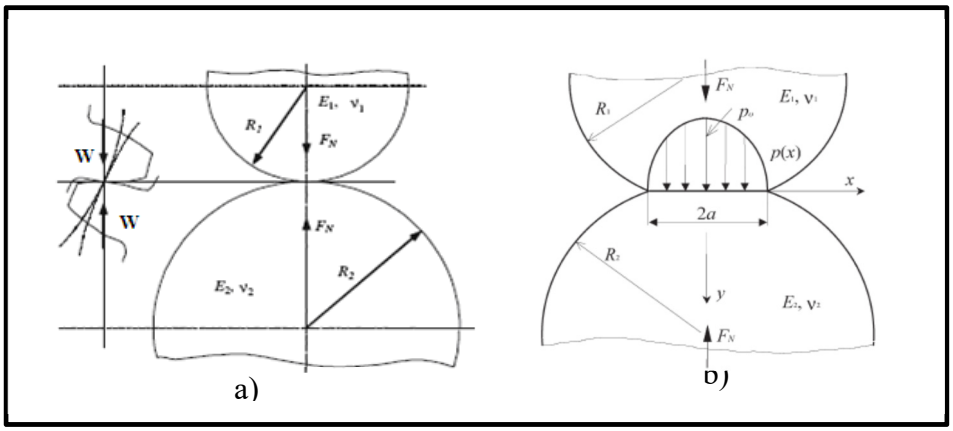

Figure 1-12 Normal pressure at contact region: a) Model transformation of meshing gears to the equivalent model of two cylinders for the contact point, b) the normal pressure at contact point presented as parabolic form, (Sraml, 2007)

1.3.5 Effects of sliding on rolling contact fatigue

To introduce dynamic contact, a combination of the two movements, rolling and sliding, must be considered. For a period of 24 years, Morrison (1968) conducted tests on copper, steel, bronze, aluminum and non-metallic materials to obtain surface fatigue resistance data using pure rolling and combined rolling and sliding with different slip percentages. He obtained that the relative rotational roll speed on the pitch line of the contact interface causes wear by contact rolling at the pitch region.

Thus, the normal stresses do not change in intensity but the tangential stress is modified by adding sliding. The distributions of maximum shear stress adjusted in dynamic contact in case of subsurface pure rolling, pure sliding and combined rolling and sliding are illustrated in Figure 1-13. In pure rolling, the shear stress reaches maximum peaks at a point deeper than is the case of combined rolling and sliding, (see Figure 1-13).

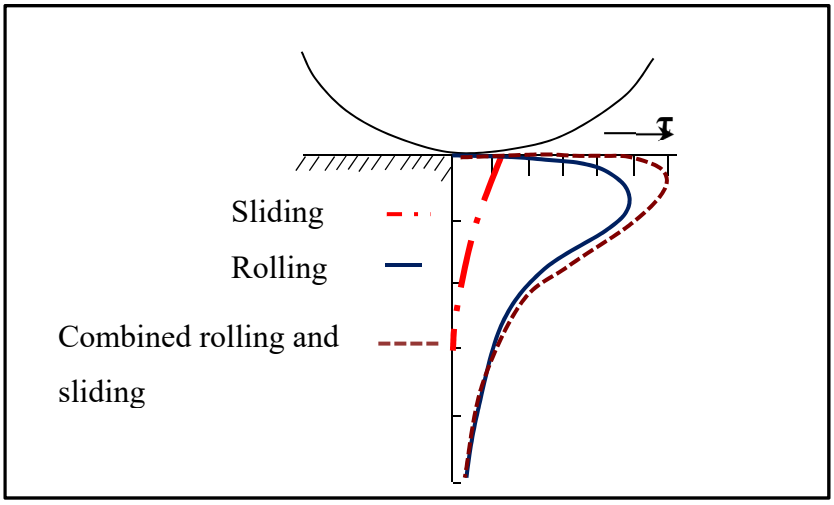

Figure 1-13 Maximal shear stress distribution in contacting surface due to pure rolling, pure sliding and combined rolling and sliding, (Alban, 1985)

An analysis of the influence of friction in rolling-sliding contact by Broszeit (1977) shows that this effect offers another possibility to shift the maximum shear stress close to the surface while

the friction increases, (see Figure 1-13). The maximum shear stress τ_{max} increases with surface friction, and the position changes from $0.786a$ for the contact surface (a is the semi length contact).

The sliding generates maximal shear stress peaks closer to contact surface and change the distribution of maximal shear stress in the subsurface, from the surface to a depth of $1.25\ a$ (a is semi contact length) and increases the value from $0.2\ p_0$ to $0.5\ p_0$ at contact surface by increasing the friction coefficient from 0 to 0.4, (see Figure 1-14). Thus, the sliding effect does not reach deeper than in the hardening surface study. With significant case depth, the sliding effect favours nucleation crack occurrence much closer to the contact surface (small pitting risk). This effect is an interesting prospect for a future study.

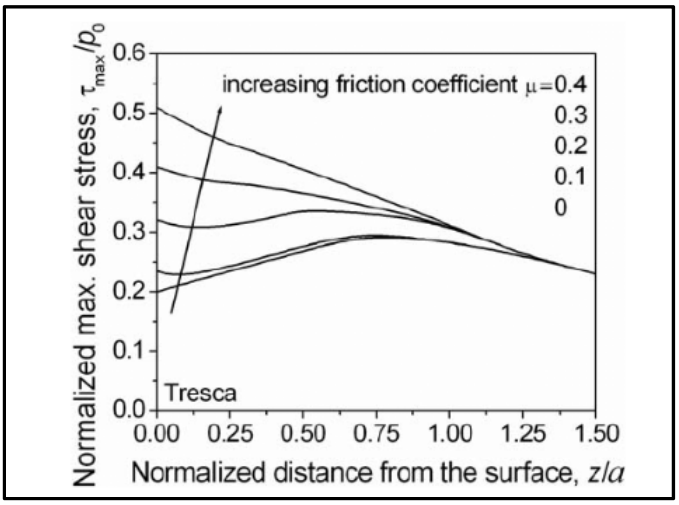

Figure 1-14 Maximum shear stress by Tresca variation in depth as a function of friction coefficient, (Broszeit, 1977)

On the other hand, most experimental tests show that pitting occurs mostly in the pitch region where the pure rolling load applies. Following Alban's (1985) work on gear failure, the mechanics of subsurface pitting by pure rolling contact fatigue in normally loaded gear teeth mostly depend on the maximum shear stress τ_{max} plane, below the surface at a depth ranging from 0.18 mm to 0.31 mm, ahead of the pure rolling contact point (pitch line-free sliding). For a heavy load, this distance of maximum shear stress is deeper and the crack propagation tends

to turn to inward. The cracks continue under repeated stress until heavy pitting or spalling takes place.

In many procedures, such as carburization, nitriding, and induction hardening, case-heat treatment is used to introduce compressive residual stress in case depth, which covers these distances of maximum shear stress area. These surface heat treatments have been experimentally shown to delay crack nucleation; thereby allowing heavier loading. The crack initiation mechanics depend on the maximum shear stress plane, but some spalling originates below the case/core transition zone, (see Figure 1-15, Figure 1-16), (Alban, 1985).

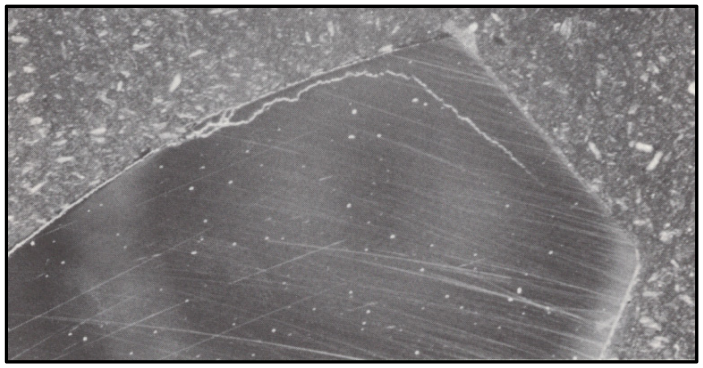

Figure 1-15 Spalling-a subsurface fatigue failure originating at case/core interface, at transition of carburized case of gear tooth, (Alban, 1985)

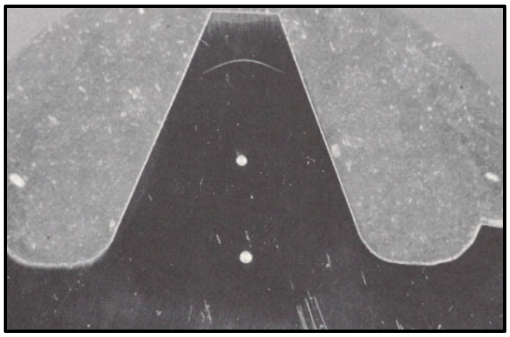

Figure 1-16 An internal rupture in a gear tooth at the case-core transition zone which does not reach the surface, (Alban, 1985)

Fernandes (1997) confirmed that surface contact fatigue is the most common cause of frequent failure mode in gears. There are three modes of surface failure resulting from surface fatigue; these modes depend on the distribution of stress on the surface: the rolling contact fatigue occurs along the pitch line of gear flank and leads to nucleation cracks; spalling is the cause of wide and deep nucleation cracks on contact surfaces. This failure is either due to pure rolling or a combination of continuous sliding and rolling or cracks at the interface between case depth and the gear core.

As mentioned in the preceding paragraph, Alban (1985) and Fernandes (1997) worked on nucleation cracks below the contact surface 0.18 mm to 0.31 mm below the case/core transition region. Their study focuses on pure rolling case and the effect of residual stress on pure rolling contact fatigue and trying to predict the nucleation crack by FEA modeling base on this remark reference of nucleation region. It also aims to see how the residual stress profile influences nucleation cracks on the surface and subsurface of treated parts. Our study will explain these mechanics base on stress analysis by multiaxial criteria in the next chapter.

1.4 Prediction of rolling contact fatigue

In the past decades, a number of investigators have attempted to predict RCF by experimental or analytical methods. Most authors based their study on the analysis of rolling contact stress to describe the RCF process. This chapter presents some theories on RCF analysis.

For rolling contact analysis and modeling of homogeneous metal parts under elastic contact loading conditions, many approaches use the Hertz stress distribution theory to calculate the maximum shear stress on the orthogonal plane, in order to predict the maximum allowable loading needed to prevent RCF, (Hertz, 1881; Johnson, 2004). The orthogonal shear stress reaches a maximum in two planes below the surface simultaneously: one parallel and one perpendicular to the contact surface, (Zaretsky et al., 1965). The Lundberg-Palmgren theory postulates that the most critical stress factor for fatigue damage is described by the maximum subsurface orthogonal shear stress and that fatigue failure is always initiated by the maximum

orthogonal shear stress at the depth where it occurs, and it can be used to predict the maximum allowable loading and fatigue life, (Lundberg and Palmgren, 1952). Following these approaches, many authors have successfully predicted fatigue life, as well as the maximum allowable loading in the rolling contact fatigue life of homogeneous metal, (Sadeghi et al., 2009; Lundberg and Palmgren, 1952, Coy et al., 1975; Harris et al., 1999, Zaretsky et al., 1995; Harris et al., 1996).

For analysis and heterogeneity modeling of heat treated metal, heterogeneity is introduced. Models based on the assumption of homogeneity are no longer valid for surface treated parts as significant heterogeneity is present in the part. Heat surface treatments, such as induction hardening, carburization, and nitriding improve rolling contact fatigue performance. Many approaches have taken into account the need of generating heterogeneities in the microstructure to increasing hardness, as well as to induce residual stress gradients, (Savaria, 2014, Savaria et al., 2016; Palin-Luc et al., 2011). Alternative methods have been proposed to estimate the RCF life of components, including a linear combination of Hertz theory and heterogeneity gradient measurements, (Muro et al., 1975; Pazdanowski, 2014; Morison, 1968) and experimental approaches, (Koibuchi et al., 1982; Shipley, 1974; Townsend, 1995; Akata et al., 2004).

To control the RCF of a treated component, numerous authors have developed their own mathematical models and experimental methods to evaluate the effect of residual stress on RCF predictions. The residual stress intensity has been recognized as the most important parameter for controlling crack nucleation, (Muro et al, 1975; Pazdanowski, 2014; Morrison, 1968). Based on the Lundberg-Palmgren theory, Zaretsky et al. (1995) showed that the orthogonal shear stress in the perpendicular plane-to-surface contact is not significantly affected by either hoop or residual stresses. They suggested that in the presence of residual stress, the maximal shear stress on a plane (45- to 90-degree (horizontal) range), τ_{45} (Tresca stress) or octahedral stress (Von Mises stress) parameters should be used to analyze the rolling contact fatigue life.

In situations where high compressive hydrostatic stresses are present, the Dang Van criterion will overestimate the maximum allowable loading (Flavenot et al., 1984; Lefebvre, 1989), as this criterion cannot consider the possibility of exceeding a certain plastic limit in the compressive hydrostatic domain. In particular, plastic deformation may take place due to material kinematic hardening or softening, (Johnson, 2004), resulting in a shakedown process.

To keep the model as simple as possible, this kinematic behaviour will not be used in the present work; however, this study does not use the multiaxial Dang Van criterion in compressive hydrostatic conditions but rather a critical shear stress value (taken as the material torsional fatigue limit). This critical shear stress is used as the torsional fatigue limit and kinematic hardening is not considered. This represent an idealised material within yields elastic behaviour (Johnson, 2004). Several authors, including Desimone et al. (2006) and Bernasconi et al. (2005), have successfully predicted the allowable loading for RCF in the presence of residual stress using the Dang Van criterion, as well as a given stress fatigue limit in compressive hydrostatic conditions. While these works provided convincing results, they did not predict or discuss the positions of nucleation sites. Moreover, they did not consider any material property gradient in the rolling parts. These two aspects will be discussed in the present study, and represent the main novelty of the work.

1.4.1 Multiaxial fatigue criteria

Another approach is to consider a high hydrostatic stress gradient. Crossland (1954) has shown that hydrostatic stress does not seriously affect yield criteria, but may influence the strain required to cause fatigue failure. In particular, tensile stress favours this mechanism, whereas hydrostatic compressive stresses help to restrain it, (Harris et al., 1996; Palin-Luc et al., 2011; Muro et al., 1975; Pazdanowski, 2014; Flavenot et al., 1984; Lefebvre, 1989; Nemkov et al., 2013). In the presence of the RS case, many authors, such as Crossland, Sine, and Dang Van use multiaxial stress analysis criteria (including hydrostatic stress effect) as an effective critical stress for predicting rolling contact fatigue, (Sadeghi et al., 2009; Palin-Luc et al., 2011; Flavenot et al., 1984; Dudragne et al., 1981; Ekberg et al., 1995; Kim et al., 2014). In rolling

contact, the contact region stress distribution is multiaxial (also called non-proportional) as the shear stress and normal stress are out of phase. The Dang Van criterion is particularly interesting in the case of RCF because values are calculated using the shear and hydrostatic stresses at any "time"; especially as this allows for non-proportional behaviour. As a consequence, Dang Van criterion will be used in the present work, and further details will be provided as the work proceeds.

1.4.2 Dang Van criterion

The superposition of rolling contact loading on a residual stress field results in a permanently varying multiaxial stress state. Dang Van proposed a multiaxial fatigue limit based on a mesoscopic scale approach. With Papadopoulos, they proposed a multiaxial fatigue damage theory covering both the unlimited fatigue life (fatigue limit criterion) and the limited fatigue regime (multiaxial Wöhler curve, multi-level cyclic loading).

As cracks usually occur in transgranular slip bands, the local shear acting on these planes is an important parameter. Moreover, the normal stress acting on these planes accelerates damage formation. For this reason, hydrostatic stress is preferred because it is much easier to use, being an invariant scalar. Furthermore, it can be interpreted as the mean value of the normal stresses acting on all the planes that pass through the point considered in the structure. Based on these remarks, Dang Van (1993) chooses for a stress function f(σ) relation between the local shear stress τ_{max} and the local hydrostatic stress σ_H. The simplest criterion that can be conceived is a linear relationship between these quantities:

$$f(\sigma) = \tau_{max} + \alpha\sigma_H - \beta \tag{1.2}$$

where α and β are material parameters; α is the limit angle of Dang Van limit line, which present the tensile hydrostatic stress effect on fatigue (rad), β is the torsional fatigue limit value (MPa). The safety domain (no fatigue crack initiation) is delimited by two straight lines in Figure 1-17, which can be determined by experiments such as uniaxial tests of tension-

compression and torsion on classical fatigue test machines. The elastic shakedown has been assumed that in the high cycle fatigue regime, at least for loading paths equally the corresponding fatigue limit.

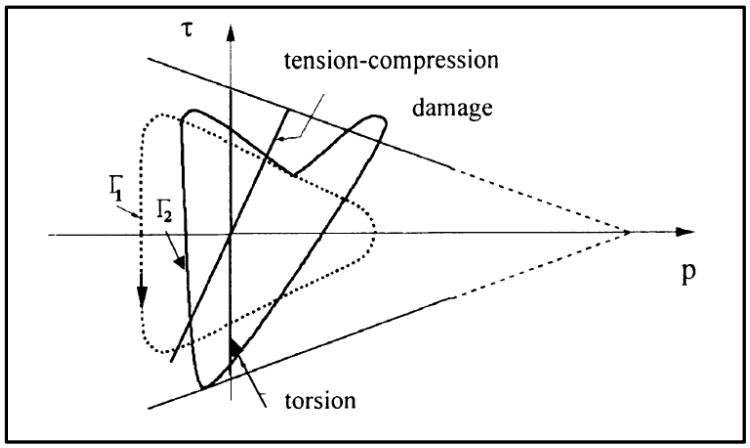

Figure 1-17 Fatigue limit domain and typical loading path, (Dang Van, 1999)

Figure 1-17 shows the internal hydrostatic stress (p) and maximal shear stress (τ) path of one studied point, the Γ_1 path is safe in the no-damage region. The Γ_2 path crosses the damage limit line. Therefore, the studied point of Γ_2 path is damaged by cracking.

1.5 Research objectives and outline

The main objective of this research is to develop a new approach to predict the maximum allowable loads of multilayer materials produced by induction hardening taking into account the significant tensile residual stresses below the surface. By combining residual stress and material gradients, this model is more complex than the one available in the literature. The non-proportional behaviour of the multiaxial stress during rolling contact problem will also be taken into consideration. This will allow us to better understand the role of RS in enhancing rolling contact fatigue performance. A finite element modeling method was developed, based on research methodology, to predict the maximum allowable load in contact with an induction-treated cylinder. This procedure will enable the study of hardened material behaviour by

examining the elastic limit and hardness of three different layers (case depth, over-tempering region and core) as well as three materials of different mechanical properties.

Four specific steps can help to inform the main objective:

(1) Use experimental measurements of residual stresses in an induction heat treated part for the purpose of superimposing them in the numerical model;

(2) Build a numerical model using the finite element method (FEM) to simulate two parallel cylinders in contact under pure rolling conditions. The model should be expandable to include sliding contact conditions;

(3) Quantify the influence of rolling contact fatigue generated residual stresses on maximum allowable loading (F_{max}), nucleation crack position; pressure limit (p_o^{limit}), maximum residual shear stress limit, in both the compressive region ($\tau_{max}^{C\_RS\_limit}$) and the tensile region ($\tau_{max}^{T\_RS\_limit}$);

(4) Optimize the case depth thickness.

CHAPTER 2

METHODOLOGY

2.1 Introduction

This chapter presents the heterogeneities typically found in an induction treated AISI 4340: micro hardness profile and the related fatigue properties of each correspondent material found in the part. The analysis theory of contact is then presented followed by the maximal pressure of non-conform cylinder bodies in contact and a convergence study on a FEA model. Finally, the geometry and property-modeling is detailed to introduce RS in the part.

Two strategies are then proposed to reach the defined objective. The first strategy investigates the effect of hardness gradient and RS on the maximum rolling contact load with a RS profile having a case depth of 0.8 mm and a 200 MPa in tensile hydrostatic residual stress peak. The second strategy studies various case depths and RS profiles to maximise the allowable load. A multiaxial fatigue criteria-based approach is proposed to predict the maximal load by RCF.

2.2 Material and Hardness

The material used, AMS 6414 (similar to AISI 4340), is a martensitic low alloy steel (with 0.4 %C). Typical applications for 4340 alloy steel include structural use, such as in aircraft landing gears, power transmission shafts and gears. 4340 alloy has good hardenability, allowing parts made with it to be fully hardened and later tempered to the desired hardness. A hardness of 48 HRC provides a good compromise between fatigue strength and toughness, but is not hard enough for contact fatigue applications. However, thanks to induction hardening, the surface of a 48 HRC tempered martensitic part can be transformed to a hard martensitic phase of around 60 HRC, providing excellent wear resistance to the manufactured part.

A surface region reaches austenitic temperature and upon quenching becomes hard martensite. The high heat flow generated by induction treatment generates an underlying “over-tempering”

region with a lower hardness than the initial one. The hardness of this region can be significantly lower than the bulk hardness and a value of 38 HRC was chosen as a representative hardness for this homogeneous layer in this study. A typical hardness profile is shown in Figure 2-1 for a case depth of 0.8 mm. Here, three different zones can be identified: case hardening (60±2 HRC) with a thickness of 0.8 mm, the over-tempering zone (as low as 38±2 HRC) over 0.7 mm, and the core region below (48±3 HRC). Table 2-1 presents the material and fatigue parameters of the different regions present in induction treated parts as characterized by Savaria (2014, 2016). This typical profile was used as the material gradient in the present model.

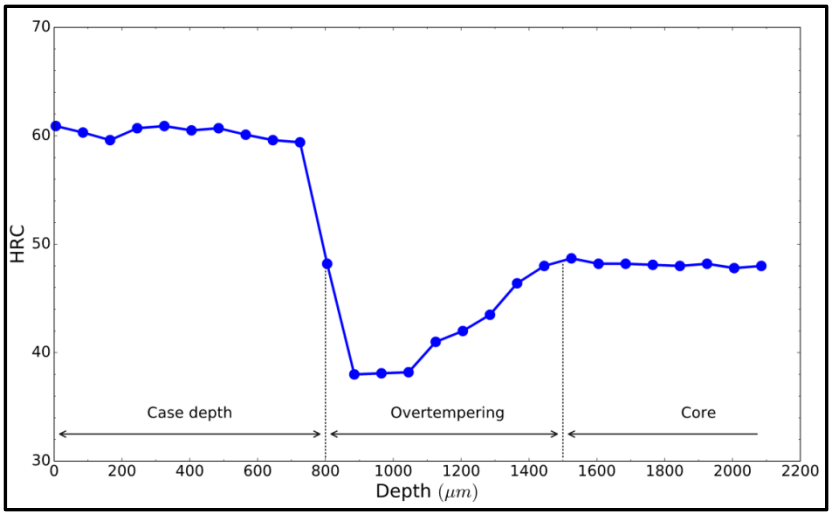

Figure 2-1 Hardness profile of induction treatment from the surface to the core

The hardness gradient generated in the part results in a corresponding gradient in the elastic, plastic and fatigue properties of the material. For example, the Young's modulus of the material was found to vary with steel hardness, being lower for higher hardness (Reitinger et al., 2008). However, the variations were only by a few percentage points (about 5%) (Savaria, 2014; Moghaddama et al., 2014) making them somewhat insignificant in terms of strain heterogeneities. For the sake of simplicity, these heterogeneities were not taken into account in the present version of the model. On the other hand, the gradient in plastic and fatigue

properties was considered and simplified as a superposition of 3 layers of materials with the properties provided in Table 2-1.

Table 2-1 Hardness, thickness, and material fatigue parameters of different material conditions present in induction hardened parts from Savaria (2013) and Savaria et al. (2016)

Layers	**Case depth**	**Over-tempering (OT)**	**Core**
Hardness (HRC)	60±2	38±2	48±3
Thickness (mm)	From 0 to 0.8	From 0.8 to 1.5	>1.5
τ_e yield stress in simple test (MPa)	801	546	630
σ_y yield strength (MPa)	1570	1132	1370
Fatigue Dang Van parameters			
α (for 10^6 cycles)	0.688051	0.808051	0.616051
β (MPa) (for 10^6 cycles)	801	440	529

2.3 Finite element modelling

2.3.1 FEA model validation by static contact stress in 3D description

An analytical solution helps to validate a finite element analysis (FEA) model by ANSYS software. This consists in the comparison of simulation results. Hertzian theory on the contact of elastic solids has been summed and is commonly used to solve contact problems. The contact area and stress distribution are determined by the contact geometry, the load, the material properties and the elastic body deformation. Contact geometry depends on the contact surface, which could be convex or a combination of flat, convex and concave. The shape of the contact area depends on the curvature of the bodies' contact. In many practical contact body engineering applications, to control the axis of rolling, the gear flank or contact surface of the cylinder will be machined to be tightly elliptical in the axial direction to allow contact

control. Thus, in the contact surface analysis in this modeling approach, the couple of parallel cylinders will be considered as a non-conform cylinders (Figure 2-2). The maximum contact pressure obtained by analysis will be compared to that obtained with the finite element method to validate the model (APPENDIX I).

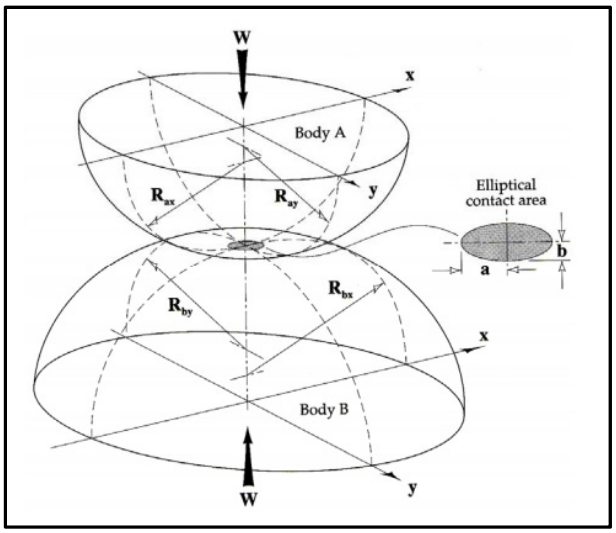

Figure 2-2 Elliptical contact area for a non-confirming contact; for each contact wheel, there are two radii in the axial and tangential directions; p_{max} is the maximum contact pressure, a and b are the half-width of the elliptical contact, (Antoine et al., 2006)

Regarding contact between bodies of homogeneous material, the subsurface stress generated by loading contact limited by the high macroscopic Hertzian stresses in a region is called a Hertzian zone (this region contains the maximum local Tresca shear stress). According to Lundberg and Palmgren (1952), fatigue life is limited by the behaviour of this zone, and the Tresca stress is the most significant factor impacting the RCF.

2.3.2 Maximum contact pressure in 3D

The formulas for subsurface stress and maximum contact pressure in a non-conform cylinder contact are developed in the following section. The solution for elastic stresses in polar

coordinates for a circular contact patch was given by Huber (1904). Dimensions are normalized to the contact radius, R_e:

$$\frac{\sigma_{\theta\theta}}{p_0} = -\left[\frac{1-2v}{3r^{*2}}\left\{1-\left(\frac{z^*}{u^{1/2}}\right)^3\right\} + \frac{z^*}{u^{1/2}}\left\{2v + \frac{(1-v)u}{1-u} - (1+v)u^{1/2}tan^{-1}\left(\frac{1}{u^{1/2}}\right)\right\}\right] \tag{2.1}$$

$$\frac{\sigma_{rr}}{p_0} = \frac{1-2v}{3r^{*2}}\left\{1-\left(\frac{z^*}{u^{1/2}}\right)^3\right\} + \left(\frac{z^*}{u^*}\right)^3 + \frac{u}{u^2+z^{*2}} + \frac{z^*}{u^{1/2}}\frac{(1-v)u}{1+u} + (1+v)u^{1/2}tan^{-1}\left(\frac{1}{u^{1/2}}\right) \tag{2.2}$$

$$\frac{\sigma_{zz}}{p_0} = -\left(\frac{z^*}{u^{1/2}}\right)^3\frac{u}{u^2+z^{*2}} \tag{2.3}$$

$$\frac{\tau_{rz}}{p_0} = -\frac{r^*z^{*2}}{u^2+z^{*2}}\frac{u^{1/2}}{1+u} \tag{2.4}$$

$$\tau_{r\theta} = \tau_{z\theta} = 0 \tag{2.5}$$

where

$$\text{u}=\frac{1}{2}\left[r^{*2}+z^{*2}-1+\left\{\left(r^{*2}+z^{*2}-1\right)^2+4z^{*2}\right\}^{1/2}\right] \tag{2.6}$$

where r is the radial direction; θ is the hoop direction; z is the axial direction, and p_0 is the maximum pressure.

For principal stress at the contact center of an elliptical contact, Greenwood (1967) proposed direct stresses along the Cartesian axes (radial, axial and hoop stresses) as the principal stresses:

$$\sigma_z = p_o \tag{2.7}$$

$$\sigma_x = 2\nu.p_o + (1-2\nu)\frac{b}{a+b} \tag{2.8}$$

$$\sigma_y = 2\nu.p_o + (1-2\nu)\frac{a}{a+b} \tag{2.9}$$

x is axial direction, z is radial direction and y is hoop direction, a and b are contact semi-length, ν is Poisson's coefficient.

To obtain the maximum pressure at the contact center of a non-conformal contact, Greenwood et al., (1967) and Brewe et al. (1977) have shown a validated method calculated from an equivalent radius Re, load W, Young model:

$$p_0 = \frac{1}{\pi}\left(\frac{6WE^{*2}}{R_e^2}\right)^{1/3} \tag{2.10}$$

where p_0 is the maximum pressure at the contact center, W represents the contact loads (N), E^* is the equivalent Young's modulus, and R_e is the effective radius.

To determine the effective radius R_e of the relative principal curvatures of contact (A, B):

$$R_e = \left[A.B\left(\frac{A+B}{2}\right)\right]^{-1/3} \text{ with } A = \frac{1}{R_1} + \frac{1}{R_2}; B = \frac{1}{R_1'} + \frac{1}{R_2'} \tag{2.11}$$

R_1 and R_2 are contact cylinder radius

In the case where $B \approx A$, Hamrock and Brewe recommend:

$$k = \frac{a}{b} \approx \left(\frac{B}{A}\right)^{\frac{2}{\pi}};\ \varepsilon \approx 1 + \left(\frac{\pi}{2} - 1\right)\left(\frac{A}{B}\right);\ \frac{1}{E^*} = \frac{1-\vartheta_1^2}{E_1} + \frac{1-\vartheta_2^2}{E_2} \tag{2.12}$$

$$a = \left(\frac{3k^2\varepsilon W R_e}{\pi E^*}\right)^{1/3}, b = \left(\frac{3\varepsilon W R_e}{\pi k E^*}\right)^{1/3} \tag{2.13}$$

ν_1 and ν_2 are Poisson's coefficients of two cylinders.

The authors also proposed calculating the semi-axis lengths of elliptic contact *a, b* by *c* as the effective radius of circular contact by an area of πc^2 in:

$$p_0 = \frac{3W}{2\pi c^2} \text{ and } c = \sqrt{ab} \tag{2.14}$$

The formula (2.14) was used to study the convergence of ANSYS modelling as a function of the mesh contact size. See APPENDIX I for simulation error versus analysis solution.

2.3.3 Maximal shear stress in 2D

The maximal shear stress is a major factor of nucleation cracking under critical loading as mentioned by some authors, (Morrison, 1968; Muro et al., 1975; Lundberg-Palmgen, 1952; Zaresky et al., 1995; Norton, 2006). It is necessary to review this factor under rolling loads. This factor will be used to analyze the maximal residual shear stress. 2D analysis is always needed to understand contact load-induced stress variation in a critical plane. The distribution of stress created below the contact surface by the transmission of load W from one gear tooth to a pinion tooth, (see Figure 2-3), is expressed by the following formula.

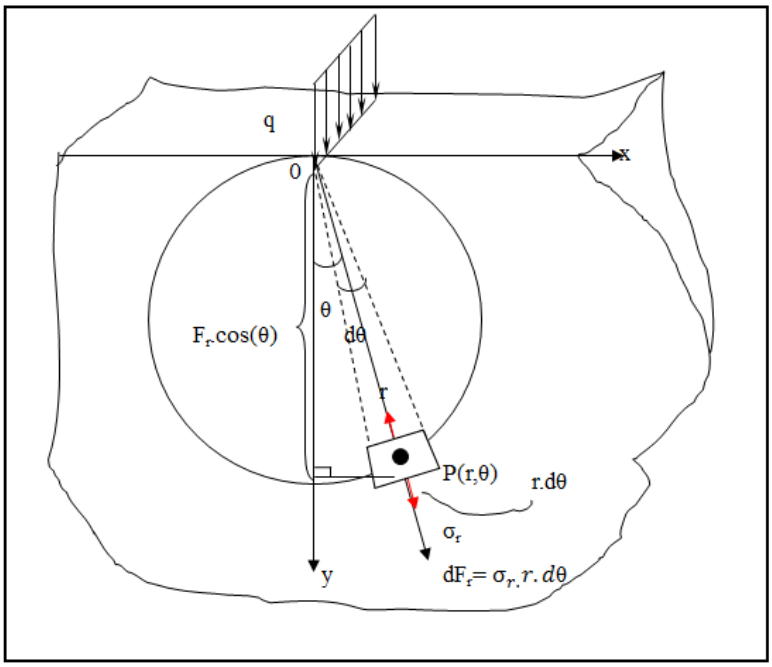

Figure 2-3 Stresses generated due to transmission load W, (Jonhson, 2004)

The stresses in perpendicular plane to rolling direction and surface contact are expressed by, see APPENDIX VIII:

$$\sigma_x = \sigma_r \, sin^2(\theta) = -\frac{2W}{L\pi}\frac{x^2 y}{(x^2+y^2)^2} \tag{2.15}$$

$$\sigma_y = \sigma_r \cos^2(\theta) = -\frac{2W}{L\pi}\frac{y^3}{(x^2+y^2)^2} \tag{2.16}$$

$$\tau_{xy} = \sigma_r \sin(\theta)\cos(\theta) = -\frac{2W}{L\pi}\frac{xy^2}{(x^2+y^2)^2} \tag{2.17}$$

In the Hertz theory, with the cylinder contact, the normal pressure contact is presented as a parabolic pressure form at the pitch line's gear, the principal stresses due to normal pressure could be used by the derive from the (2.1), (2.3) and (2.4), are expressed by:

$$\sigma_{x=-p_o}\left\{\left(1+\frac{2y^2}{a^2}\right)\left(1+\frac{y^2}{a^2}\right)^{-\frac{1}{2}}-\frac{2y}{a}\right\} \tag{2.18}$$

$$\sigma_y = -p_o\left(1+\frac{y^2}{a^2}\right)^{-\frac{1}{2}} \tag{2.19}$$

The maximal shear stress is:

$$\tau_{max} = \frac{\sigma_{max}-\sigma_{min}}{2} = \frac{\sigma_x-\sigma_y}{2} \rightarrow \tau_{max=p_o}\left\{\frac{y}{a}-\frac{y^2}{a^2}\left(1+\frac{y^2}{a^2}\right)^{-\frac{1}{2}}\right\} \tag{2.20}$$

The maximal shear stress reaches maximum value in depth at z:

$$\tau_{max} = 0.3p_0 \text{ at y= } 0.786 \text{ a} \tag{2.21}$$

At the contact surface (y=0), the stresses are:$\sigma_x = -p_0,\ \sigma_y = -p_0$, and $\tau_{max} = 0$.

Figure 2-4 illustrates the distribution of the principal stresses absolute values (from 2.18, 2.19 and 2.20 formulations) under the contact surface center and explains the fatigue initiation mode for untreated gears (homogeneous material): at the contact surface which undergoes cyclic loading, the contact-alternating stress can reach a large figure and, after a number of cycles, cause subsurface cracks. In the homogeneous body, some researchers, such as Hertz (1881),

Johnson (1987), Norton (2006), Shipley (1974), found that at a depth of 0.786a, where the maximum shear stress reaches $0.3p_0$, the nucleation crack at this critical depth can develop into lateral cracks, in the maximum shear stress plane.

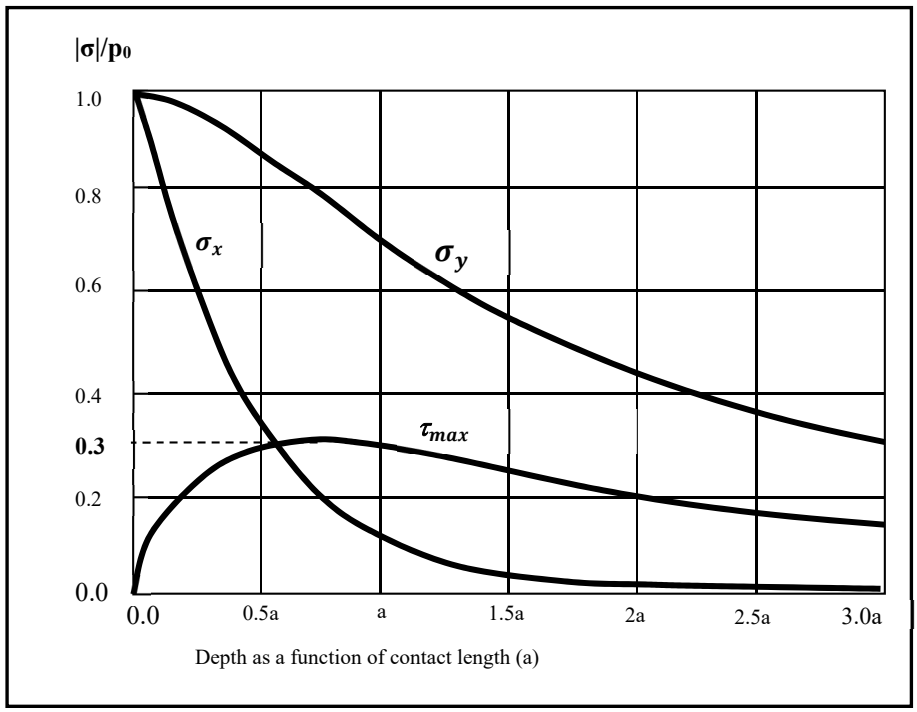

Figure 2-4 Maximal shear stress as a function of maximal pressure evaluated at the center line below the contact centre, a is semi length contact

2.3.4 Geometry and rolling contact properties

Two cylinders in contact were modeled in the present work. A 3D model was developed assuming perfect cylinder geometries, frictionless contact and an elastoplastic material. This allowed the problem to be resolved in a static way by considering fixed cylinders pressing on each other to represent the actual rolling of the two cylinders on each other. While this significantly simplified the real problem, it allowed some major contact-related issues to be addressed, as shown in Kadin (2015). With such a model, the loading path can then be deduced by varying the angular position of the investigated point. As a singular stress concentration appears at the edges of the contact formed by two straight parallel cylinders according to

Shipley (1974). In order to relocate the stress concentration to the center of the rolling contact one of the cylinders (the top one) was an elliptic crowned cylinder. Figure 2-5 presents the 3D models of the contact cylinders. The studied cylinder is the flat one at the bottom (A), while the top elliptic crowned cylinder (B) was used to transfer the load to cylinder A. The two cylinders had an outer diameter of 48 mm. The cylinder models had a hollow core, with the top one having an inner diameter of 16 mm and the bottom one an inner diameter of 11 mm. Both cylinders were 6 mm thick. The elliptic cylinder on top had a crowned shape, with a 1 mm semi-minor axis and a 3 mm semi-major axis.

The top cylinder was characterized by zero displacement in the axial direction, but was free in the vertical (radius) direction versus the loading direction. For its part, the bottom cylinder, which was the one studied, had a fixed inner radius; a vertical load applies at the inner radius of the top cylinder, causing the top cylinder to press the bottom cylinder. The Young's modulus E for the 3 martensitic phases present in an induction hardened AISI 4340 part (fresh, tempered and over-tempered) were considered equal to 205 GPa, and the Poisson's coefficient μ was set to 0.3. The elastic limits of the 3 materials were introduced in the finite element analysis (FEA) elastoplastic model, assuming a perfectly elastoplastic material as shown in Table 2-1. However, care was taken to ensure that the maximum loading simulated did not exceed the initial yield load. In this study, a multiaxial criterion is used to estimate the maximum loading in the presence of high hydrostatic stress (caused by RS), with the maximum shear stress being below the torsional fatigue limit (which is usually smaller than the yield stress).

The surface contact element is defined as surface-surface contact under frictionless conditions. The finite element model was generated by 3D meshing, with SOLID186 elements (8 nodes).

The typical elliptic/cylinder bodies in contact loading generate stress and deformation below the contact surface, local mesh refinement was needed in this area. A mesh convergence was run, (see APPENDIX I), in order to optimize the meshing strategy, and a convergence was achieved with a mesh refinement of 0.08 mm in the region below the surface, and this value

was used in the present work. With 0.08 mm, the 3D model achieves a total of 352 127 brick elements and 1 462 312 nodes.

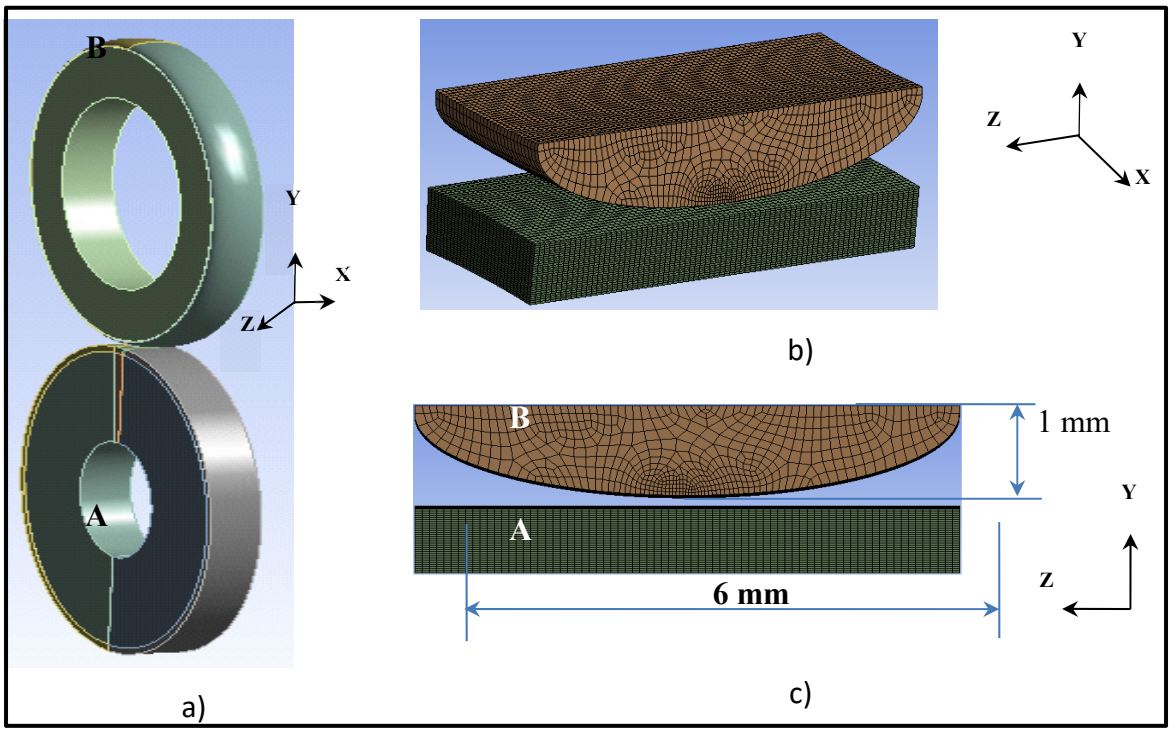

Figure 2-5 Schematic representation of the mesh at contact zone: a) global view of flat cylinder A and elliptic cylinder B; b) fine meshing in the spaces of elliptic center and flat cylinders in contact; c) zoom of contact zone showing the fine mesh of 0.08 mm of YZ plane

The hardness gradient in Figure 2-1 is simplified in 3 regions and the elasticity variation limits are introduced in the FEA model. In the current case, the fatigue stress limits the load imposed by the plasticity and that imposed by the yield limit. These data are summarised in tables 3-1, 3-2 and 3-3. The maximum shear stress/material elastic limit ratios, called shakedown limit ratio were added to support the fact that no onset of plasticity was predicted in the FEA, in the limit of 4.7 from Johnson (2004).

2.3.5 Residual stresses modeling

This work devised to 2 modules. A first module was built to validate the modeling by inserting the experimental RS measurement. This module aimed to compare the effect of RS on maximum allowable loading with that of an untreated part in investigation of effect of RS and hardness on RCF. The case depth used is 0.8 mm. A secondary module was made in which the applied temperature was varied to produce peak tensile hydrostatic stresses set at 100 MPa, 200 MPa and 250 MPa as a function of case depth variation for 0.5; 0.8;1.0; 1.2 and 1.8 mm including a special case of 2.4 mm for 250 MPa in tensile hydrostatic residual stress peaks. This module aims to find the optimum induction hardening case and also the effect of case depth and RS on the pressure limit, the nucleation crack region in the part.

2.3.6 Case depth of 0.8mm with a tensile hydrostatic stress peaks of 200 MPa

The typical residual stress profile shown in Figure 2-6 was generated by applying a thermal gradient in the part using a thermal expansion coefficient equal to $1.2x10^{-5}$(1/°C). A temperature of 260 °C was applied at the circumference, a temperature of 110 °C at the case depth of 0.8 mm, and a temperature of 20 °C in the core.

The residual stress gradients generated by thermal variations in the cylinder are shown in Figure 2-6 as 2D cross-sections. It can be observed that hoop and axial residual stresses vary from compressive in the transformed region, to tensile, in the over-tempering region, and drop to zero in the core. One example of simulated residual stresses over the cross-section is maximal at the center, and varies not only from the outer layer to the core of the cylinder, but also from its edge to its center. Similar heterogeneities typical of residual stress profiles found on gear teeth were also found experimentally and by simulation after induction hardening (Nemkov et al., 2013; Reitinger et al., 2008; Kadin, 2015).

The simulated residual stress profile is compared to the experimental one measured by Savaria (2014) in Figure 2-6d. The simulation results underestimate the residual stress at the surface

below 200 microns; however, these regions are not the ones generating fatigue damage. This underestimation was then ignored. Some other discrepancies are found in the region between 200 and 400 microns but the high hydrostatic stress associated with this region of the material prevents any significant effect on the fatigue predictions. As will be seen later, it is the intensity of the shear stress that drives the crack nucleation in such conditions. Axial stress was used because tensile hydrostatic stress directly affects multiaxial fatigue, (Savaria, 2014; Palin-Luc et al., 2011; Flavenot et al., 1984; Ciavarella et al., 2006).

It should be noted that the stress profiles are quite uniform in the region of interest (where contact stress will be applied and RCF studied at about 200 μm). At the 200 μm in depth, the experimental measurement and simulated results of axial stress reach similar values. This depth is typical of crack nucleation points (as shown in the next chapter). Despite the conservative (lower) axial stress obtain in the FEA compare to the measurement results from surface to 200 μm in depth, no nucleation was predicted in this region, confirming that the discrepancies in that part of the curve can be ignored. The FEA results shows that the maximum compressive stress is about 535 MPa in the axial direction at 380μm below the surface. The maximum tensile value of 360 MPa is identified in the axial direction, at 1050μm below the surface, almost at the center of the over-tempered region (Figure 2-6d).

The built model allows a virtual study of material and hardness gradient parameters for a given case depth (0.8 mm) and the residual stress gradient (Figure 2-6d), in addition to the role of residual stresses on the RCF. The following section will present results obtained for various combinations obtained by varying intensities of parameters such as peak tensile hydrostatic stress and case depth.

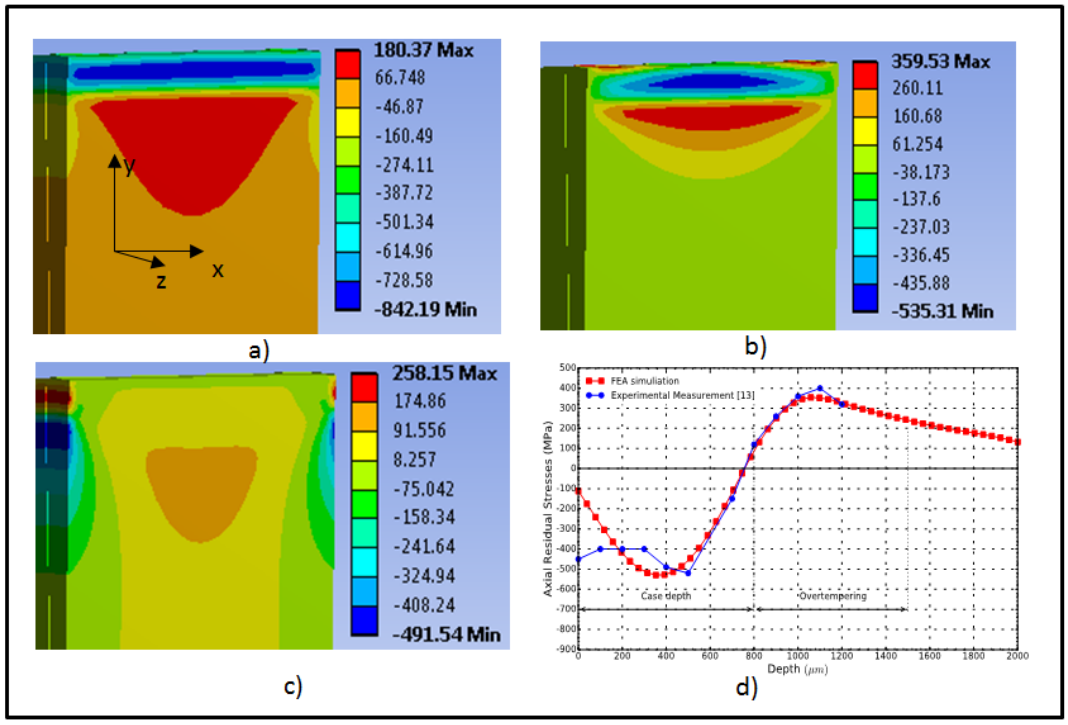

Figure 2-6 Residual stress distributions introduced in straight cylinder A according to the 3 directions (in MPa): a) hoop stress; b) axial stress; c) radial stress; d) the correlation between the FEA simulation and an experiment measurement of axial residual stress

During the very short duration of the treatment (less than a second), the surface temperature gradients and the martensitic transformation temperature generates high compressive residual stresses in a fresh martensitic layer. The residual stress profile typically associated with such a hardness profile is shown in Figure 2-7: the compressive residual stresses are not maximal at the surface. Instead, the maximum is reached at a depth of about 0.38 mm, i.e., in the middle of the case depth region. The tensile residual stress balances out these compressive residual stresses and remains mainly confined to the over-tempering region. The compressive peak axial residual stress varies between -500 and -900 MPa while the tensile peak residual stress varies between 200 and 400 MPa, as in Savaria (2014). These measured RS profiles were used as a reference by Savaria (2014) for generating the profile for finite element analysis.

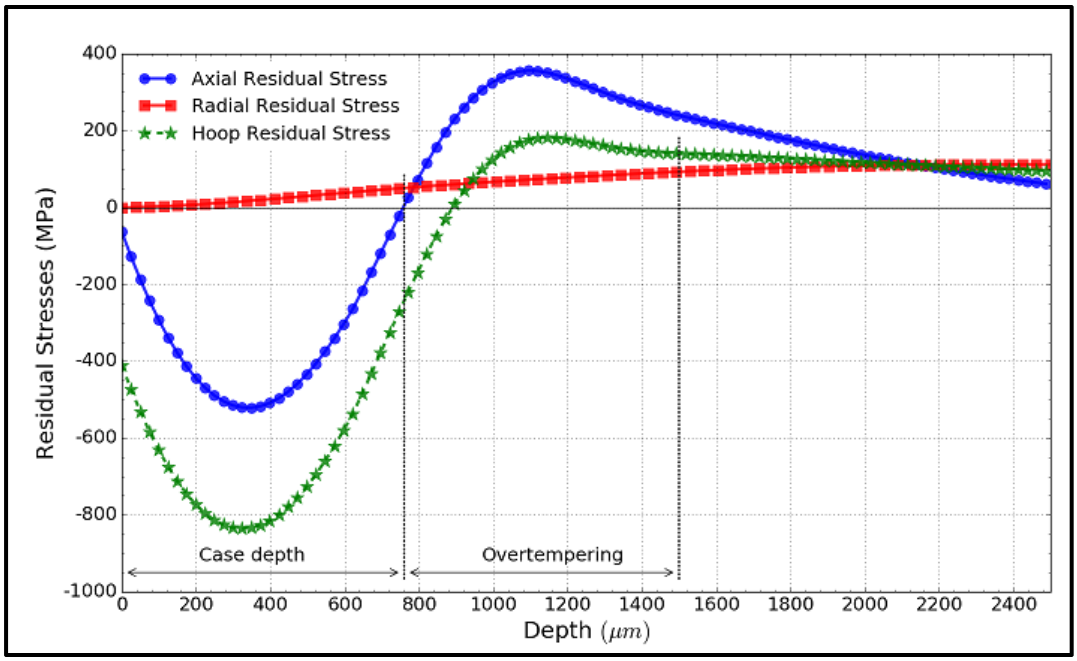

Figure 2-7 Typical profile by FEA: residual stresses in axial, hoop, and radial directions

Figure 2-8 shows the variation of the hydrostatic stress induced by the residual stress from the surface to the core of the cylinder. Compressive hydrostatic stresses are found in the case depth, whereas their tensile equivalents are present in the over-tempering region. In the proposed example, the tensile hydrostatic stress reaches a maximum of 200 MPa at 1.0945 mm below the surface. The presence of this maximum hydrostatic stress could promote the degradation mechanisms related to the Dang Van criterion. In the present case, this is not the main concern due to the selection of a conservative fatigue limit in compressive hydrostatic conditions. The limit of case depth is almost validated with measurement of microhardness. The change of stress sign near the case depth value, the transition to tension stress occurs about 90 µm before the case depth limits (Savaria, 2014).

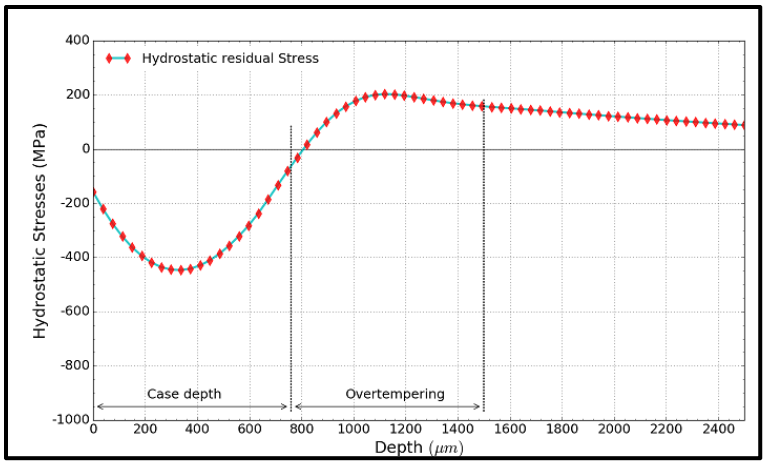

Figure 2-8 Hydrostatic residual stress in depth (MPa) and tensile residual stress peak of 200 MPa at depth of 1.0945 mm, by FEA results

2.3.7 Residual stress simulations for case depth of 0.5, 0.8, 1.0, 1.2 and 1.8 mm and tensile hydrostatic stress peaks of 100, 200, 250 MPa

To study the effect of residual stress on the initiation nucleation crack, the new residual stress profile will be modified to generate the tensile residual hydrostatic stress of 100, 200, 250 MPa. For each tensile residual hydrostatic stress level, case depths thicknesses were varied from 0.5, 0.8, 1, 1.2, and 1.8 mm, (see APPENDIX III). The new residual stress profile extends to 1.8 mm of case depth, in a condition that maintains a full residual stress under compression at the surface. The typical residual stress profile shown in Figure 2-9 was generated by applying a thermal gradient in the part using a thermal expansion coefficient equal to 1.2×10^{-5}(1/°C). Temperatures varying from 110 °C to 360 °C were applied at the circumference, a temperature of 110 °C at the case depth, and a temperature of 20 °C in the core.

An example of the residual stress profiles as a function of case depth for a fixed peak tensile hydrostatic stress of 200 MPa is shown in Figure 2-9. It can be seen that when the case depth increases, the compressive stress intensity decreases (less compressive at surface).

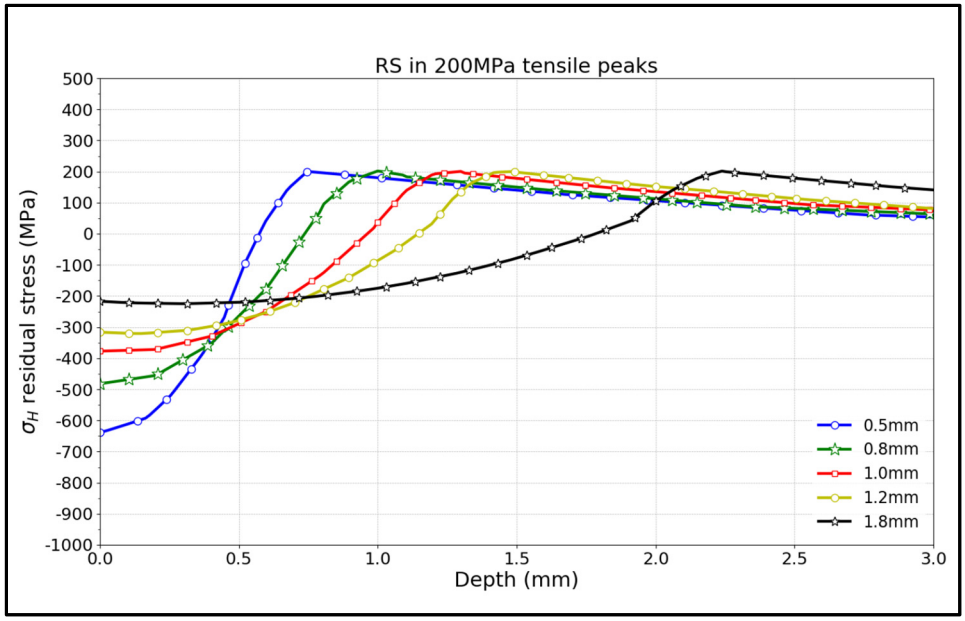

Figure 2-9 Hydrostatic stress at 200 MPa as a function of case depth, by FEA results

Dang Van criteria were used to analyze the maximum allowable loading for each case of these combinations. In chapter 4, these residual stresses are studied with the goal of determining their effect on case depth, tensile RS peaks to the nucleation crack positions and maximal loading.

2.4 Multiaxial fatigue criteria

This section provides a detailed presentation of the criteria used to predict RCF. They consist of a combination of the Dang Van criterion and a maximum allowable loading (set as the torsional fatigue limit) in conditions where a high compressive hydrostatic stress is present.

The multiaxial Dang Van criterion is defined as a boundary for the maximum shear stress and hydrostatic stress below which no propagating cracks are found in the material before a certain number of fatigue cycles. The fatigue performance of a material can be quantified by the equivalent stress value evaluated by the weighted sum of the local maximum shear stress (τ_{max}) and the hydrostatic stress (σ_H) (Palin-Luc et al., 2011; Flavenot et al., 1984; Desimone et al., 2006; Bernasconi et al., 2005; Ferguson et al., 2012; Hömberg et al., 2016; Van Lieshout

et al., 2017 and Ciavarella et al., 2006). If this equivalent state of stress is lower than a maximum equivalent stress, called β, the Dang Van multiaxial criterion predicts that damage will not take place, as described by:

$$\tau_{max} + \alpha\sigma_H \leq \beta \tag{2.22}$$

where α and β are material constants as specified in Table 2-1 (Savaria, 2014; Savaria et al., 2016). Although the RCF rises to between 10^7 to 10^8 cycles (Glaeser et al., 1996), and because fatigue data for such high numbers of cycles are confidential for the three material conditions considered in the present study, fatigue data for 10^6 cycles will be used to demonstrate the potential of the proposed model (the values are actually not significantly different). This equation shows that the hydrostatic compressive stresses increase the maximum allowable shear stress τ_{max}, that is, if a compressive hydrostatic stress (negative value) occurs, the maximal shear stress has to reach high value (positive value) to obtain a effective stress which reaches the β limit. It is usually represented on a graph with the hydrostatic positive stress on the x-axis and shear stress on the y-axis, as can be seen in Figure 1-17.

2.5 Loading path distance to Dang Van limit and torsional shear limit

As presented in the previous chapter, the crack nucleation point in a part is identified as the location where the combination of the maximum shear stress point and hydrostatic stress reaches the Dang Van limit. In order to capture the severity of each instant in the loading cycle for RCF, the damage for each "moment" of the cycle should be evaluated. The proportional relationship τ versus σ_H can be rewritten to define a potential damage degree, $d_{i,\theta}$, that can be defined for each angular position θ and position i in the part as:

$$d_{i,\theta} = \frac{\tau_{i,\theta} + \alpha\sigma_{H_{i,\theta}}}{\beta} \leq 1 \tag{2.23}$$

Hence, d_i is defined as the maximum damage degree value for a full turn; τ is the maximal shear stress at point *i*; $\sigma_{Hi,\theta}$ is the hydrostatic stress at point *i* and angle θ.

When undergoing a specific cyclic loading, the shear stress τ and the hydrostatic stress σ_H of a given point are not necessarily proportional. Thus, a complex "non-proportional" τ versus σ_H behaviour can occur in some areas of the part. In this case, the high damage may not coincide with the maximum shear stress point τ_{max}. Hence, the minimal distance to the Dang Van limit defined by equation (2.24) can be calculated and the loading condition for which this distance is zero will provide the nucleation condition. The distance from each point i at the rotation angle θ to the Dang Van limit during a revolution can be defined as follows:

$$l_{i,\theta} = \frac{1}{\sqrt{2}}\left(1 - \frac{\tau_{i,\theta} - \alpha \times \sigma_{H_{i,\theta}}}{\beta}\right) \tag{2.24}$$

It is important to point out that with this convention, the value of $l_{i,\theta}$ is positive if the $\tau - \sigma_H$ curve is below the Dang Van limit line, i.e., the studied point i is in the fatigue safe zone.

$$l_{min} = \min_{i,\theta}\left(l_{i,\theta}\right) \text{ where all } l_{i,\theta} \geq 0 \tag{2.25}$$

The loading conditions under which crack initiation takes place correspond to the condition under which $l_{i,\theta} = 0$. The region of the part for which this value is reached will be identified as the critical nucleation region.

On the other hand, it is known that the Dang Van criteria do not properly describe the material behaviour in the presence of significant negative hydrostatic pressures (Desimone et al., 2006; Dang Van et al., 2002; Romanowicz, 2017). A simple constant limit has been introduced in the present work, in order to keep the model simple even though more complex approaches likely exist in the literature.

The amplitude shear stress τ_{max} used in the yield criterion is based on Tresca's criterion. This fatigue limit τ_f is defined here as the fatigue limit for 10^6cycles, which corresponds to the constant β obtained from pure torsion fatigue tests: $\tau_f = \beta$. This value actually represents the intersection of the Dang Van line and the vertical axis (amplitude of shear stress) for zero

hydrostatic stress. In the present work, based on the historical work of Crossland (1954) and Burn et al. (1964), the critical shear fatigue is chosen to be independent of hydrostatic stress for the negative hydrostatic region of the multiaxial graph. This choice is conservative as one could expect this critical value to increase somewhat following the Dang Van behaviour for low compressive hydrostatic stress values. As will be discussed later in this study, documenting the critical behaviour of the material in this region of the multiaxial graph precisely is critical for developing robust RCF models. However, this requires the development of complex tests and must be carefully tuned from the experiments. In the present work, the critical shear stress for crack nucleation will be kept constant and equal to the pure torsion fatigue critical stress τ_f .

The fatigue criteria used are then defined as follows: a propagation cracking point is considered to be nucleated at 10^6 cycles when at least one of the two equalities corresponding to Dang Van criterion A or shear fatigue limit B is reached.

$$\begin{bmatrix} \text{A: } l_{min} = 0 \\ \text{B: } \tau_{max} = \tau_f \end{bmatrix} \tag{2.26}$$

CHAPTER 3

EFFECT OF INDUCTION HARDENING ON MAXIMUM ALLOWABLE LOADING

3.1 Introduction

This chapter analyzes the origins of the advantage resulting from induction hardening treatment on the maximum allowable load. A comparison is made between a case without induction hardening and a case depth of 0.8 mm with tensile hydrostatic stress peaks of 200 MPa simulations. The magnitude of maximum loads and the position of the nucleation crack region are discussed. This chapter investigates the effect of hardness and residual stress on the maximal loading of RCF.

3.2 Effect of residual stress on maximal allowable load

To better understand the properties controlling the RCF behaviour of an induction hardened cylinder, parameters such as the homogeneous/heterogeneous hardness, residual stress, case depth thicknesses will be studied to determine the maximum allowable load. These simulations present a cylinder which will generate cracks after 10^6 cycles and the position at which these cracks are expected to nucleate. The first case of simulation is a cylinder of homogeneous hardness, at 48 HRC (untreated). This exercise aims to understand the effect of hardness on RCF, two other simulations with induction hardening induced hardness gradients for different layers of 38 HRC and 60 HRC. Finally, the main simulation of a multilayer cylinder with a heterogeneous hardness of induction hardening with generated residual stress was done. The latter was compared to the non-treated case to find out the maximum load, which increases significantly with induction hardening.

3.2.1 Location of potential nucleation crack point for homogenous 48 HRC part (reference part)

The stress distribution inside a homogeneous 48 HRC cylinder A was calculated for the condition representing the maximum allowable load according to equation (2.26). No microstructure gradient or residual stress profiles were introduced. The simulation shows the condition of an untreated part and sets a reference state.

The maximum possible loading was found to correspond to 580 N, leading to a surface pressure of 1.68 GPa, see Figure 3-1 and Table 3-1. At this load, criterion B in equation (2.26) is reached as a maximum shear stress of 529 MPa and is found 200 µm below the surface. The part is then shown to generate cracks due to excessive shear stress and the cracks are expected at 200 µm in the case depth. Figures 3-1a and 3-1b show the results of the minimal distance l_i below the contact region, and it is clear that the Dang Van criterion has not been reached as the minimum width is 0.4125 (undimensional). However, Figure 3-2 shows that a region with an 80 µm width and 17 µm thickness present shear stress values higher than 525 MPa. These regions are the typical susceptible nucleation crack areas.

Table 3-1 Maximum loadings in homogenous parts of 48 HRC

Loads (N)	580
Maximum pressure, p_0 (GPa)	1.68
Maximum shear stress, τ_{Max} (MPa)	529
Nucleation depth (mm) at B criterion	0.199
l_{min}	0.4125
l_{min} position (mm) in depth	0.373
Shakedown ratio value, $\frac{p_o}{\tau_e}$	2.77
Nucleation crack region at τ_{Max} =529 MPa (Width x Thickness) (µm x µm)	(80x17) τ_{Max} =529 MPa

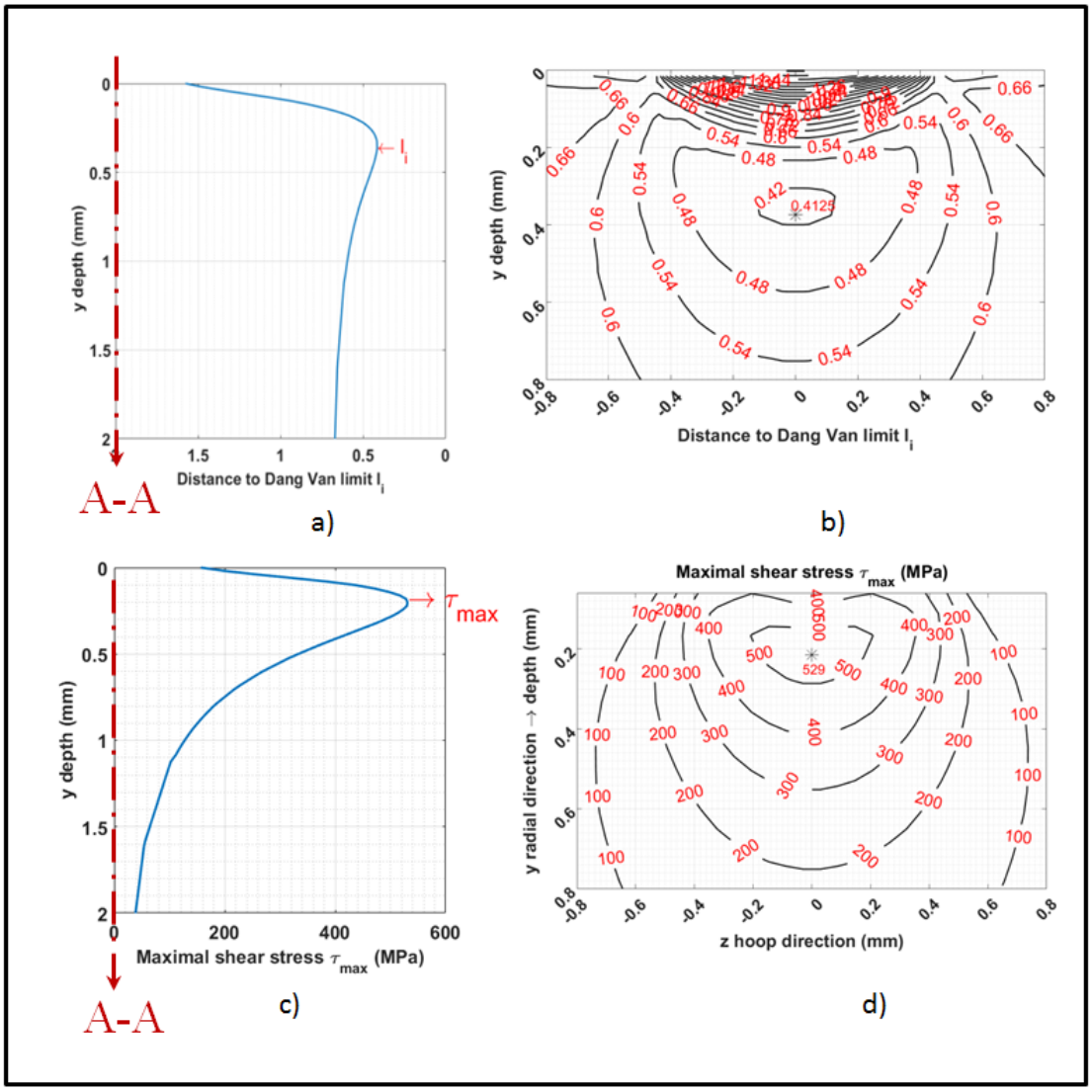

Figure 3-1 Critical Dang Van distance and maximum shear stress under maximum loading conditions corresponding to a maximum loading of 580 N on a 48 HRC part: a) Distance to the Dang Van criterion along the A-A-axis below the contact point; b) 2D map with contour lines representing the distance to Dang Van criterion below the surface contact; c) Shear stress along the axis, along the A-A-axis below the contact point; d) 2D contours for shear stress on the plane orthogonal to the contact surface at which $\tau_{max} = \tau_f$

The numeric simulation shows that the minimum damage distance calculated in accordance with the Dang Van criterion remains large when the maximum shear stress reaches its limit. It is possible that the present criterion used for the maximum shear value (condition B in equation

(2.26) is too conservative, and needs to be experimentally determined; however, the present model is able to predict subsurface crack nucleation adequately, compare with the results on nucleation site of Alban (1986).

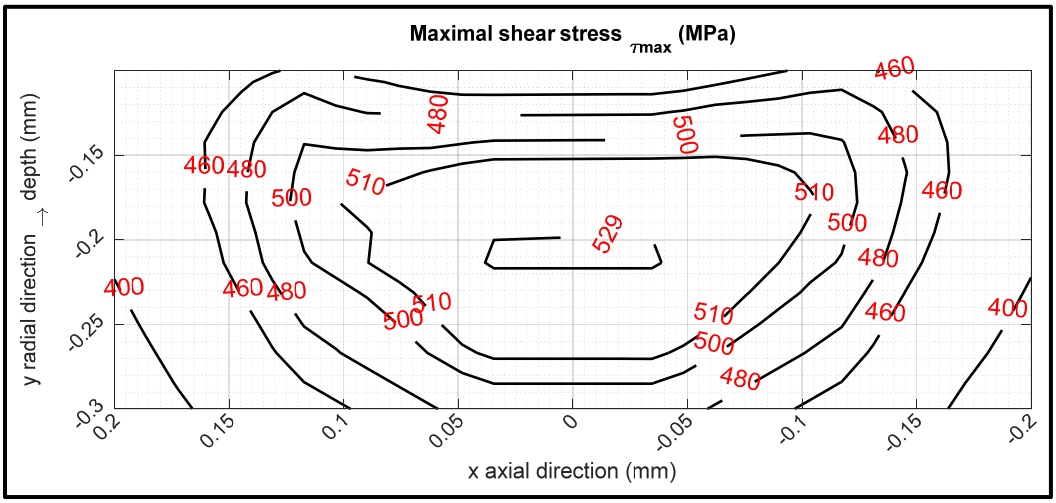

Figure 3-2 Zoom out of maximum shear stress of 529 MPa

3.2.2 Effect of the hardness in homogenous parts

The material properties of the homogeneous part were modified using the two other material properties used in this work, as defined in Table 2-1. The consequences on the corresponding applied loads and positions of the nucleation sites are reported in Table 3-2, and provide a set of references that can be used for comparison with the more realistic model developed in the following sections. The higher the hardness, the higher the maximum load and the deeper the nucleation sites. Going from 48 HRC to 60 HRC, the maximum load increases by 128 % and the nucleation depth increases by 50 µm. All parts fail according to criterion B (maximum shear stress value reached). The different loading paths are plotted on the Dang Van diagram in Figure 3-3, and show that the maximum shear stresses reach the fatigue limit in the compressive hydrostatic stress region.

Table 3-2 Maximum loadings in homogenous parts of 38 HRC, 48 HRC and 60 HRC without RS

	Hardness cases, without residual stress		
	38 HRC	**48 HRC**	**60 HRC**
Loads (N)	420	580	1320
Maximum pressure, p_0 (GPa)	1.39	1.68	2.56
Maximum shear stress, τ_{Max} (MPa)	440	529	801
Nucleation depth (mm)	0.174	0.199	0.248
l_{min} value	0.502	0. 415	0.447
l_{min} position (mm) in depth	0.372	0.373	0.452
Shakedown ratio value , $\frac{p_o}{\tau_e}$	2.55	2.67	3.19
Failure criterion	B	B	B
Nucleation crack region (Width x Thickness) (µm x µm), see APPENDIX II.	At 440 MPa 90 x 22.5	At 529 MPa 80 x 17	At 800 MPa 110 x 67.5

As the maximum shear stress point τ_{max} was found at 0.248 mm below the surface for a 60 HRC part, the target induction hardening depth was chosen at a significantly deeper point at 0.8 mm, representing more than 3 times the critical depth. This study, which examines the effect of hardness on rolling fatigue contact resistance, serves as a reference for the interpretation of future results. Variations of three hardness cases represent 3 different layers generated by induction hardening (38 HRC (OT), 48 HRC (core) and 60 HRC (case depth)). The study of hardness without RS will help provide an understanding of the role of RS in rolling contact fatigue resistance (through hardening without RS and case hardening with RS).

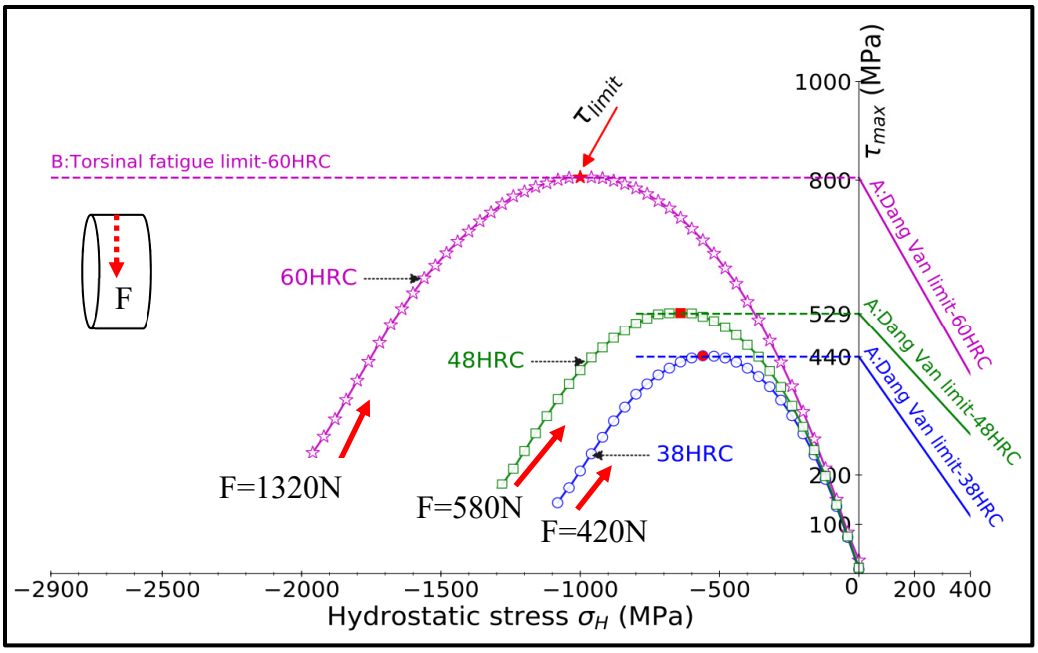

Figure 3-3 Evolution of stresses in the Dang Van diagram when applying critical loading conditions on homogeneous 38, 48, and 60 HRC cylinders (without residual stress), corresponding to maximum of 420 N, 580 N, and 1320 N, respectively

In the homogeneous case and without the RS presence, only the compressive hydrostatic stress produced by rolling load contribute to RCF. The harder the material, the higher the maximum loading, the surface point move toward higher compressive hydrostatic direction, the nucleation point move deeper in depth direction. The nucleation type is the maximal shear stress nucleation (B criterion) and crack appears near the contact surface. In this case (without of RS) the Dang Van limit is inactive (A criterion).

3.2.3 Effect of residual stress in homogenous parts

Even though this should have been a theoretical exercise, the residual stress gradient of introduced by the induction hardening process as Figure 2-7 on parts with homogeneous hardnesses was added to the models developed above. Its effects on the maximum loads and nucleation are given in Table 3-3. Due to the residual stress, the maximum allowable loads increased significantly by a factor of 2.0, 1.95, and 1.77 for hardnesses of 38, 48, and 60 HRC,

respectively. Failures were still predicted according to criterion B in equation (2.26); however, the loading paths were closer to the critical Dang Van limit, as can be seen in Figure 3-4, especially for the 38 HRC case were the minimum distance was found to be below 0.01. These shifts were due to the presence of the positive hydrostatic stresses in the residual stress profiles, which moved the critical path to the right of the diagram. The depths at which the crack nucleation was predicted were found to be similar, with or without a residual stress profile. However, the harder material, for which a deeper value was found (25 μm deeper), was the exception.

Table 3-3 Simulation results for homogeneous hardness and residual stress

	Hardness cases, with residual stress		
	38 HRC	**48 HRC**	**60 HRC**
Loads (N)	840	1130	2331
Maximum pressure, p_0 (GPa)	2.09	2.41	3.34
Maximum shear stress, τ_{Max} (MPa)	440	529	801
Nucleation depth (mm)	0.174	0.199	0.256
l_{min}	0.092	0.171	0.248
l_{min} position (mm) in depth	1.043	0.993	1.019
Shakedown ratio value , $\frac{p_o}{\tau_e}$	3.83	3.83	4.17
Failure criterion	B	B	B
Nucleation crack region (Width x Thickness) (μm x μm), see APPENDIX II.	(87.5 x 12) $\tau_{Max} = 440\ MPa$	(97.5 x 25) $\tau_{Max} = 529\ MPa$	(87.5 x 22) $\tau_{Max} = 801\ MPa$

In the case homogenous combined with induction typical RS, under the loading contact, the behaviour line generated a tensile hydrostatic stress parts, correspond to the RS in tension in subsurface of induction case, move the behaviour line approach to Dang Van limit. In the presence of compressive RS near the surface, the behaviour line near contact surface extends to a higher compressive hydrostatic stress, and then receives a higher maximal loading. In the

homogeneous case, the tensile RS under surface do not strong enough to produce the nucleation of Dang Van limit (see Figure 3-4).

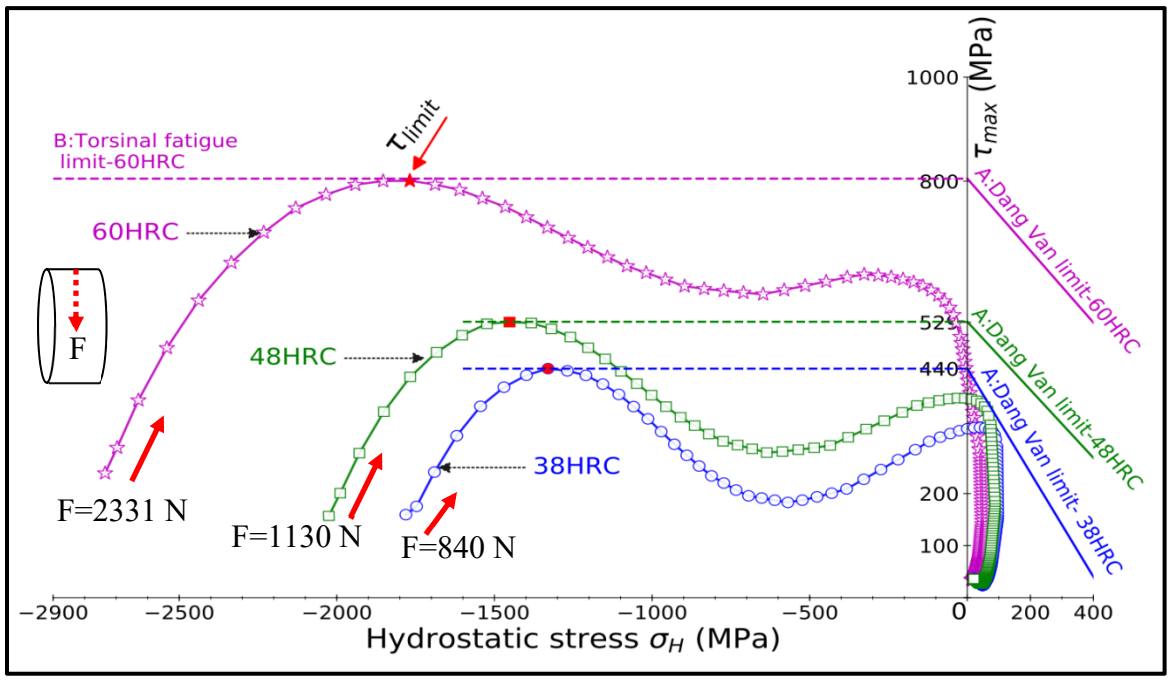

Figure 3-4 Evolution of stresses in the Dang Van diagram when applying critical loading conditions on homogeneous 38, 48, and 60 HRC cylinders with the residual stress gradient typical of induction hardening, corresponding to maximum loadings of 840 N, 1130 N, and 2345 N, respectively

The presence of induction typical RS in material increase the maximal loading by two compare to the case without RS (Figure 3.3). This induction typical RS has the compressive residual stress below the contact surface and in tension below a depth of 0.8 mm. The compressive residual reduces the maximal shear stress under contact surface resulting in a significant increase of the maximal possible load. The surface point moves toward more compressive hydrostatic stress. The nucleation point stays in the same region than in the case without RS. Crack nucleates at the maximal shear stress position. Nucleation according to Dang Van conditions (A criterion) are unlikely.

3.2.4 Multilayer and residual stress gradient

When the multilayer aspect of induction hardening was introduced in the model, a maximum loading of 1420 N was found and criterion B was still the one driving the failure, even where the loading path approached the Dang Van limit in the 38 HRC regions as shown in Figure 3-5. Even though the obtained maximum load may have been lower than the maximum obtained in the homogeneous 60 HRC cylinder, with the residual stress found in Table 3-4, it is still 145 % larger than one predicted for a homogeneous 48 HRC cylinder without residual stress, as illustrated in Table 3-1 as well. The nucleation site is predicted in the over-tempering region at 0.894 mm below the surface, i.e., 100 μm below the hardened region.

Given the presence of residual stresses, and particularly the resulting positive hydrostatic stress in the tensile portion of the profile, the distance to the Dang Van criterion becomes very small in the multilayer case, with a value of 0.00273. This suggests that if the proposed criterion B is conservative, cracks may nucleate according to criterion A. In this case, the nucleation still takes place in the over-tempering region, but at a deeper distance (at about 1.0 mm below the surface). The maximum load will only be slightly higher than the one calculated here. This shows how sensitive the fatigue model is to the proper tuning of criterion B, since if τ_f is greater than the torsion fatigue limit, failure will be controlled by the residual stress profile and not the fatigue properties of the material (of the core or the over-tempering region). The presence of tensile residual stress below the transformed region and the fatigue performance of this region is of particular importance.

Figure 3-6 shows the zoom view of over-tempering region where the stress path reached the maximum shear stress of the elastic shakedown limit ($\tau_{max} = 440\, MPa$) and the minimal distance approach the zero ($l_{min} = 2.73\, 10^{-3}$), suggesting the possibility of nucleation cracks in this two regions.

Table 3-4 Simulation results for multilayer material with induction hardening case

Loads (N)	1420
Maximum pressure, p_0 (GPa)	2.68
Maximum shear stress, τ_{Max} (MPa)	440
Nucleation depth (mm) (criterion B)	0.894
l_{min}	$2.73\ 10^{-3}$
l_{min} position (mm) in depth	1.043
σ_H max on loading (MPa)	88
σ_H max position in depth (mm)	1.59
Shakedown value , $\frac{p_o}{\tau_e}$	3.35
Failure criteria	A or B
Nucleation crack region under criterion B, (Width x Thickness) (µm x µm), see APPENDIX II.	(90x47) $\tau_{Max} = 440\ MPa$
Nucleation crack region under criterion A, (l_{min}=0.005) (Width x Thickness) (µm x µm), see APPENDIX II.	(150 x 40) (l_{min}=0.005)

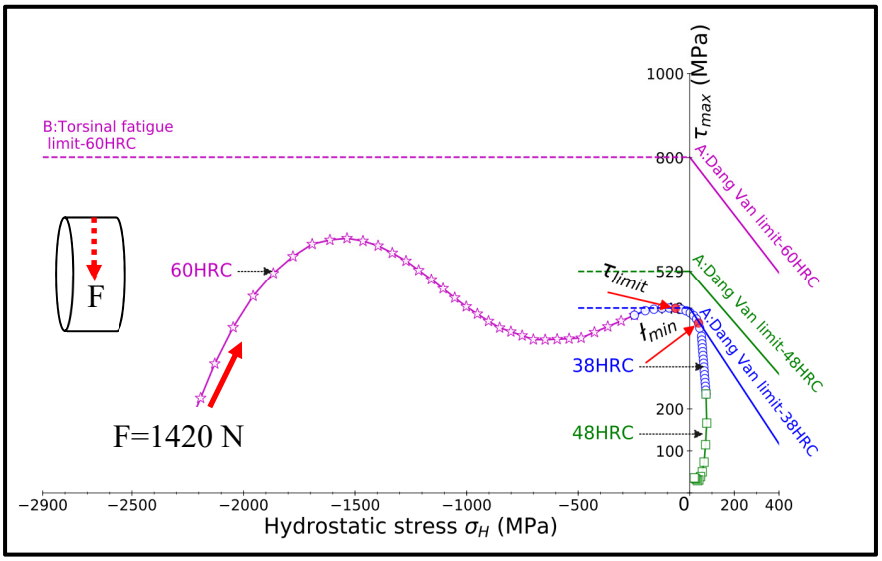

Figure 3-5 Evolution of stresses in the Dang Van diagram when applying the critical loading condition on a multilayer cylinder with the residual stress gradient typical of induction hardening, corresponding to maximum loadings of 1420 N

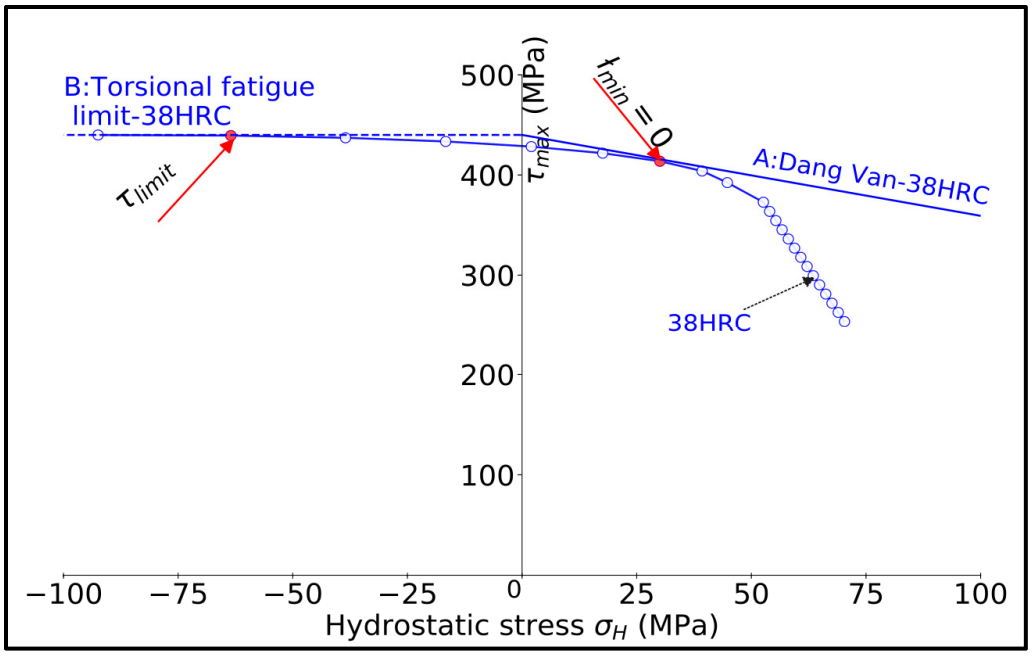

Figure 3-6 Under a load of 1420 N, the zoom views the case where the evolution line reaches the elastic shakedown and the Dang Van limit

In the multilayer case presenting the 3 different hardness materials and a RS profile, the compressive hydrostatic residual stress in case depth helps to increase the maximal loading higher but the tensile hydrostatic stress due to RS and low fatigue performance of the softer material move the behaviour curve toward the Dang Van limit in the over-tempered region. The combination of low hardness layer and the presence of tensile residual stress in this same layer can generate a nucleation crack. In this case, nucleation can either be driven by the torsional fatigue limit or/and Dang Van limit (see Figure 3-6).

3.3 Residual stress effect on the multiaxial failure criteria and nucleation crack plane

To understand the effect of residual stress on the multiaxial failure criteria and the nucleation crack position, the maximal shear stress in the plane XY, $\tau_{max}^{XY\_Fmax}$(XY is radial-axial plane which is perpendicular with contact plane and rolling direction) was studied and the homogeneous 48 HRC case was compared with heterogeneous multilayer case with the same

load of 580N. Figure 3-7 shows that the maximal shear stress in this plane XY, $\tau_{max}^{XY\_Fmax}$, is negative in the case depth (from 0.0 mm to 0.8 mm) and positive in the over-tempering region (from 0.8 mm to 2.2 mm), (blue line). In the homogenous case, under the maximal 580N loading, $\tau_{max}^{XY\_Fmax}$ reaches maximum at a depth of 0.22 mm, (see Figure 3-8). In in the heterogeneous case (multilayer) under the same 580 N loading, the $\tau_{max}^{XY\_Fmax}$ reaches two peaks, one in the case depth (0.16 mm) and one in the over-tempering region (1 mm in depth), (see Figure 3-9). This means that the maximal residual shear stress from rolling loads $\tau_{max}^{XY\_RS}$ reduces the $\tau_{max}^{XY\_Fmax}$ in the case depth and increases the $\tau_{max}^{XY\_Fmax}$ in the over-tempering region.

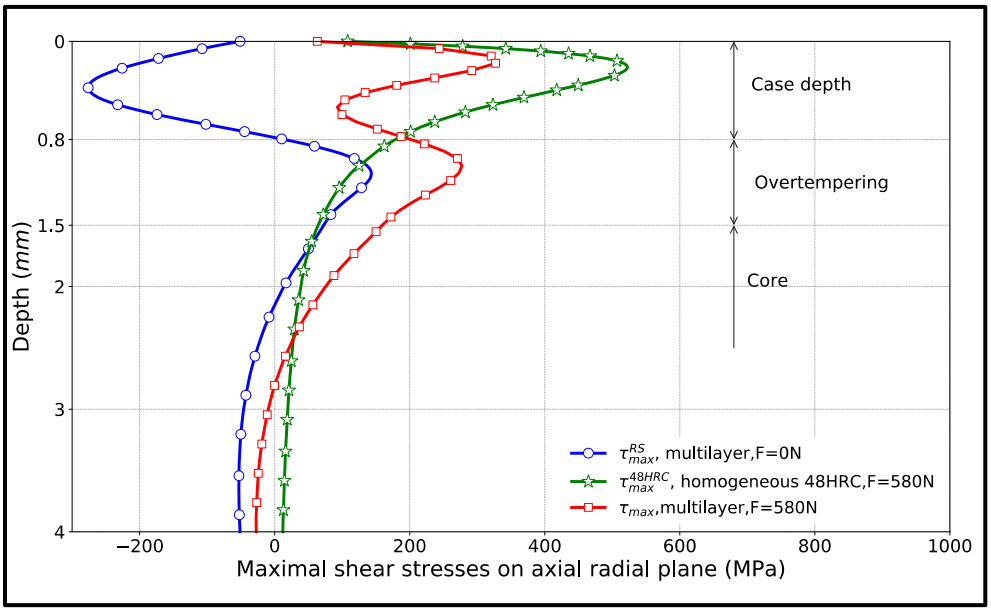

Figure 3-7 Effect of residual stress on nucleation crack point at a maximal shear stress 580 N

Figure 3-8 zooms the effect of shear residual stress in the case depth region: the maximum residual shear stress at 0.4 mm in depth, the maximal residual shear stress $\tau_{max}^{XY\_RS}$ reduces the positive maximal shear stress amplitude due to loading of 580 N to less than 529 MPa. It also reduces the position of maximum shear stress peaks relative to the contact surface.

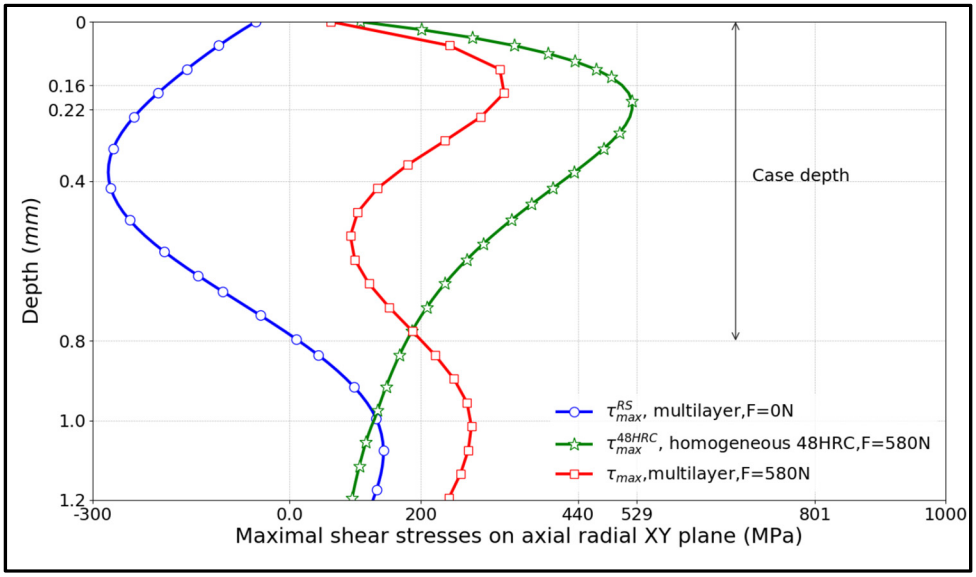

Figure 3-8 Zoom out of maximal shear stress on XY plane profile
in case depth region equivalent

The effect of residual shear stress in the over-tempering zone is shown in Figure 3-9. The residual shear stress is positive (blue line) and increases the shear stress due to loading; it reduces the distance between the maximum shear stress peaks and the over-tempering zone / case depth. This means that the maximal residual shear stress peaks reach depths of 1.09 mm; the maximal effective shear stress peaks reach 0.99 mm in depth. This latter case has a shallower case depth/over-tempering region (0.8 mm). At the maximal tensile effective shear stress peak position (0.99 mm), the effective maximal shear stress is 278 MPa, is approximatively sum of maximal residual stress (134 MPa) and maximal loading shear stress (134 MPa), (see Figure 3-9).

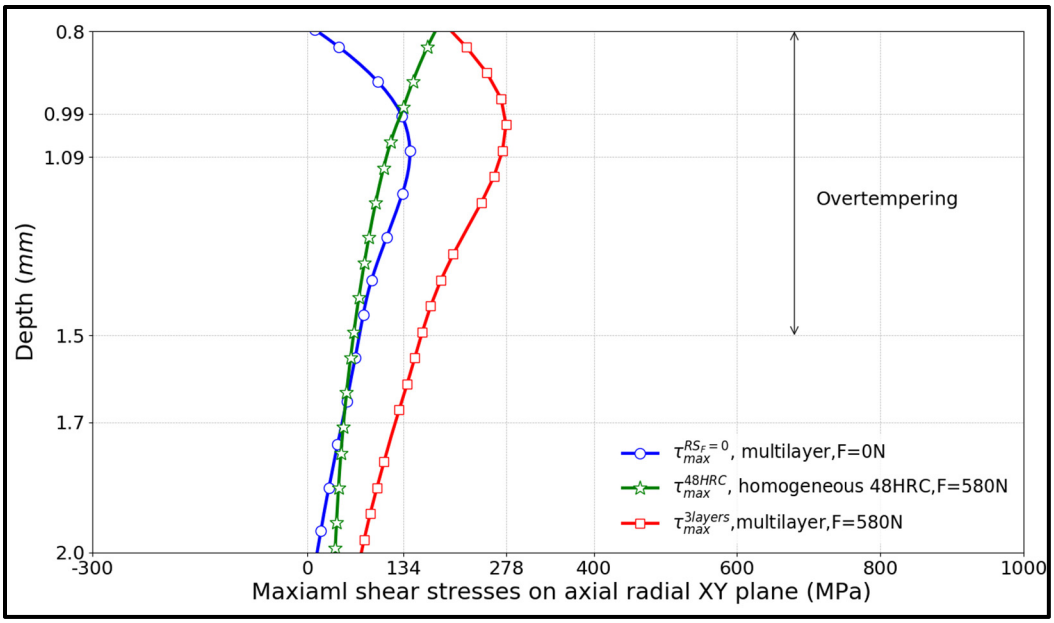

Figure 3-9 Maximal shear stress on axial radial XY plane profile in the over-tempering region equivalent

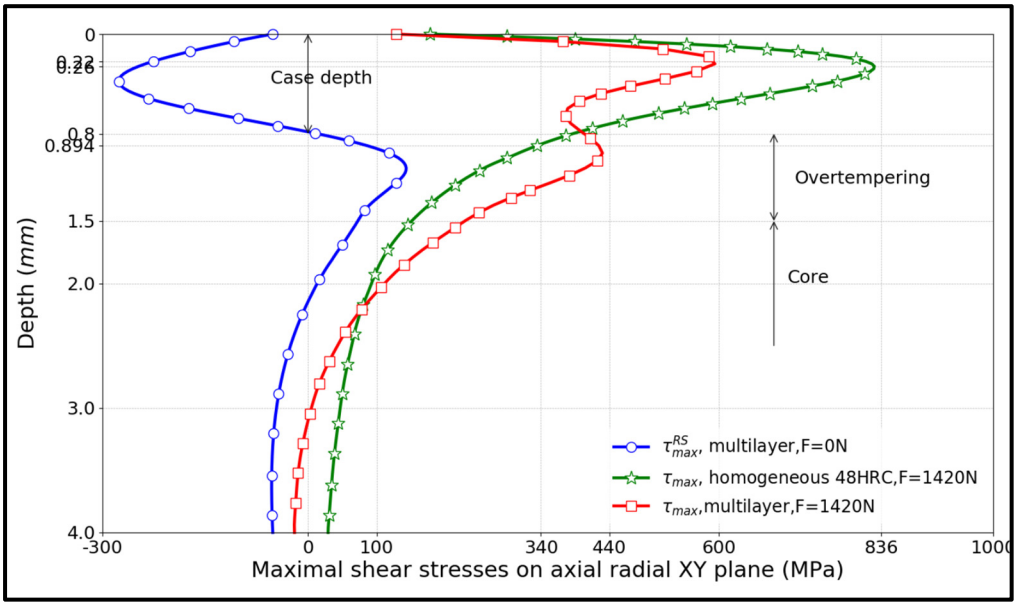

Figure 3-10 Maximal shear stress on axial radial XY plane, in multilayer without load (blue line), and under a 1420 N loading case (red line); compared with homogenous case under a maximal loading of 580 N (green line)

The blue line shows the maximal residual shear stress $\tau_{max}^{RS\_XY}$ profile in the axial radial plane. In determining the maximal load for the multilayer case, the multiaxial criteria (2.26) have to be used to find the layer by layer failure point. The Figure 3-10 shows the case under a 1420 N load, which corresponds to the maximal load for multilayer cases. The green line shows the maximal shear stress in axial radial plane of the untreated part of 48 HRC under 1420 N loading conditions. The green line shows that $\tau_{max}^{Fmax\_XY}$ the maximum shear stress of 836 MPa on the homogeneous part, at a case depth (0.0-0.8 mm), exceeds the 48 HRC shear stress limit (529 MPa) as well as the 60 HRC shear stress limit (801 MPa). Under this high loading condition (1420 N for the multilayer case), the red line shows that the $\tau_{max}^{C\_RS\_XY}$ (the compressive maximal residual shear stress in the axial radial plane) generated in case depth, reduces the $\tau_{max}^{Fmax\_XY}$ due rolling from 836 MPa to 600 MPa, but the $\tau_{max}^{T\_RS\_XY}$ generated shear in the over-tempering zone increases the $\tau_{max}^{Fmax\_XY}$ from to 180 MPa to 440 MPa. This effective maximal shear stress then reaches the fatigue limit as torsional fatigue (see Figure 3-10), at a depth of 0.894 mm. This nucleation point remains in the over-tempering region, below the case depth of 0.9 mm. This residual shear stress due to induction help to move the maximum shear stress peak in case depth to approach the contact surface (from 0.26 to 0.22 mm in depth), (see Figure 3-10). At a depth of 0.894 mm, the effective maximal residual stress of 440 MPa is the sum of maximal residual stress (100 MPa) and maximal rolling load shear stress (340 MPa).

The compressive residual stress in case depth helps to reduce the maximum shear stress peaks and reduce the rolling load induced hydrostatic tensile stress at contact surface, pushes the nucleation crack towards the contact surface, reduces the volume of the spalling material in case depth (if spalling does appear).

The tensile residual shears stress $\tau_{max}^{T\_RS\_XY}$ in the over-tempering region increases the loading induced maximum shear stress $\tau_{max}^{Fmax\_XY}$ in this region by adding their value to effective shear stress and generates a maximal shear stress that reaches the torsion limit of this softer layer. This $\tau_{max}^{T\_RS\_XY}$ pushes the location of maximum shear stress higher, bringing it closer to the adjacent of over-tempering region /case depth.

Effective maximal residual shear is depending on case depth thicknesses, tensile hydrostatic stress peaks, and compressive residual stress peaks. These factors will influence the maximum load and the position of nucleation cracks. Therefore, in the next chapter, case depth thickness and tensile hydrostatic stress peak variations will be studied.

3.4 Conclusions

This chapter demonstrated the effects of hardness and RS on the maximal loading and nucleation crack position. The harder the material, the higher the maximum possible loading. The compressive RS in case depth helps to increase the maximal loading; however, the balancing tensile RS corresponding to the over-tempering region and both factors (hardness and tensile RS) reduce the maximal loading capacity. The combination of low hardness and the presence of tensile RS will nucleate crack by maximal shear stress or/and Dang Van criteria. In the case depth region, where high compressive hydrostatic stress presence, the maximal shear stress will control the nucleation. In the over-tempering region, where the effect of compressive hydrostatic stress is reduced, the presence of RS in tension and low hardness will enhance the nucleation of crack at this region.

As the maximal shear stress due to rolling contact load is produced in axial-radial plan, it is in this plan that the RS should be considered and quantified. The contribution of RS in this maximal shear stress plan explains the increase or decrease of the maximal possible loading: the compressive residual stress produced by induction in case depth is will reduce the maximal shear stress, increasing the maximal loading; the tensile residual stress in the over-tempering region will increase the maximal shear stress, decreasing the maximal loading.

CHAPTER 4

EFFECT OF CASE DEPTH AND TENSILE HYDROSTATIC RESIDUAL STRESS ON ROLLING CONTACT FATIGUE

4.1 Introduction

The residual stress profiles mentioned in section 2.3.7 combine different case thicknesses and tensile residual stress peak variations (all profiles are presented in APPENDIX III). These profiles were introduced in the model used in chapter 2, in order to finding the optimum case depths to maximize the possible loads.

4.2 Residual stress and case depth thickness variations

In the multilayer case, the over-tempering region has a lowest hardness and smallest fatigue properties. In this weak layer, the Dang Van criterion limit the maximal hydrostatic stress to 300 MPa. The maximum hydrostatic tensile residual stress ($\sigma_H^{T\_RS}$) will then be chosen for 100, 200 and 250 MPa with case depth from 0.5 to 1.8 mm. A special case of 2.4 mm of case depth thickness and 250 MPa of tensile RS peak was extended to observe the optimum load. An example, as Figure 4-1, shows three profiles of hydrostatic residual stress σ_H^{RS} for a case depth thickness of 1.2 mm in depth direction, with the tensile hydrostatic stress $\sigma_H^{T\_RS}$ peaks of 100 MPa, 200 MPa and 250 MPa. When the $\sigma_H^{T\_RS}$ peaks increase, the compressive hydrostatic residual stress $\sigma_H^{C\_RS}$ increases, when the case depth thickness increases, the compressive hydrostatic residual stress $\sigma_H^{C\_RS}$ peak decreases.

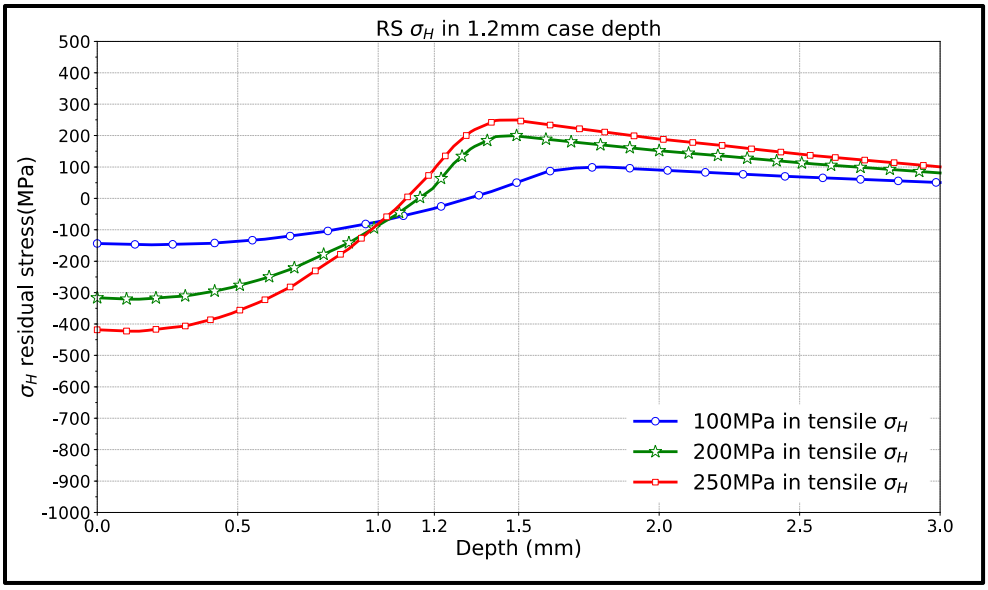

Figure 4-1 Variation of hydrostatic residual stress in case depth of 1.2 mm with 100 MPa, 200 MPa and 250 MPa of tensile hydrostatic residual stress peaks

All compressive hydrostatic residual stress $\sigma_H^{C\_RS}$ peaks of all combined cases are presented in Table 4-1.The compressive hydrostatic residual stress $\sigma_H^{C_RS}$peaks as a function of case depth thickness and tensile hydrostatic $\sigma_H^{T\_RS}$ peaks of 100, 200 and 250 MPa are presented as Figure 4-2. If the residual compressive stress at surface increases, the tensile residual stress in over-tempering zone also increases.

Table 4-1 Hydrostatic compressive residual stress variation by tensile residual hydrostatic stress $\sigma_H^{T\_RS}$ peaks (MPa) and case depth thickness (mm)

	RS in tension $\sigma_H^{T\_RS}$ peaks (MPa)		
Case depth thickness (mm)	**250**	**200**	**100**
0.5	-773	-638	-265
0.8	-625	-482	-194
1.0	-500	-377	-177
1.2	-418	-316	-143
1.8	-256	-217	-102

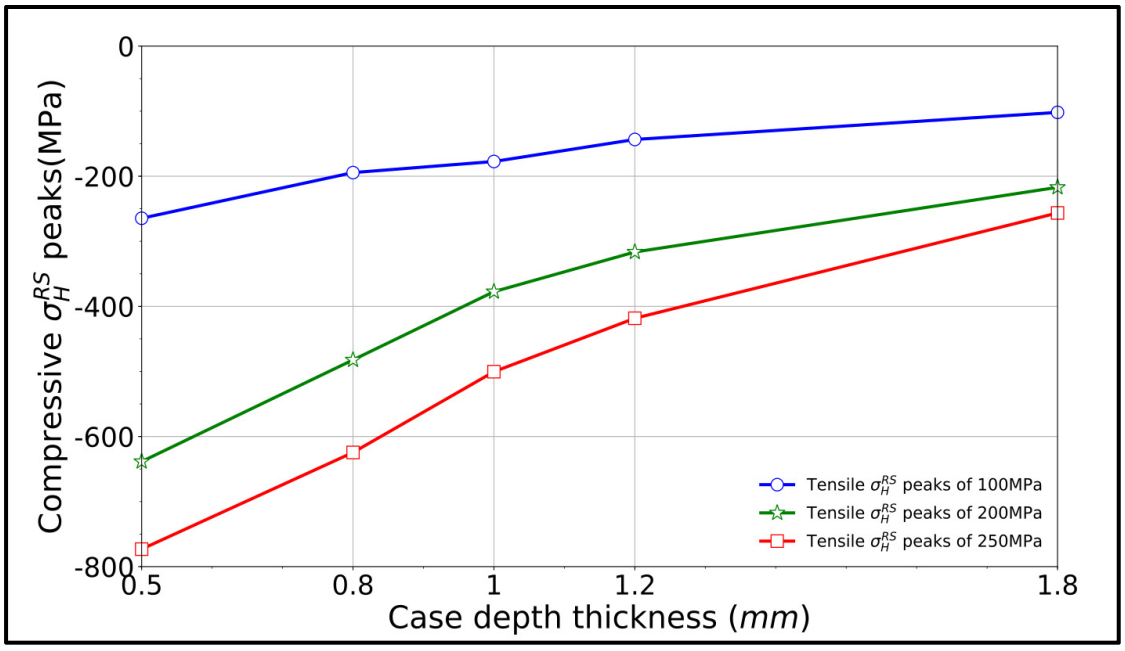

Figure 4-2 Compressive hydrostatic residual stresses $\sigma_H^{C_RS}$peaks as a function of case depth thickness for each tensile hydrostatic residual stress $\sigma_H^{T\_RS}$ peaks (100, 200 and 250 MPa)

4.3 Maximal residual shear stress in axial-radial plane XY (maximal shear stress due to rolling load plane)

The multiaxial fatigue (as two composed multiaxial criteria (2.26)) is based on maximal shear stress and hydrostatic stress. To obtain the damage limits, the effects of these two mentioned stresses on rolling contact fatigue have to be studied. Each type of stress had a different impact on the fatigue limit following the analysis. There are two states of stresses which must be distinguished: one originates from initial residual stress and the other is due to the loading state (without RS). In general, the effective stresses are the sum of residual and loading stress. When RS is present in the part, the residual stress will adjust its value to the sum of maximal shear stresses resulting from rolling loading in the same plane for each figure. Under maximal loading conditions, the rolling induced maximal shear stress is much higher than the maximal shear stress resulting from residual stress, thus the plane of the rolling induced maximal shear stress is an active plane, where nucleation cracks are likely to occur. As such, our modeling shows that the axial radial plane is the active plane where the maximal shear stress due to

rolling reaches the maximum. Along this active plane, the effect of residual stress will be analysed by two forms: the maximal residual shear stress and the maximal radial hydrostatic stress. In the axial radial plane, the maximal residual shear stress $\tau_{max}^{RS\_XY}$ directly influences the effective maximal shear stress value, $\tau_{max}^{RS+Fmax}$ by a linear addition. This effective shear stress $\tau_{max}^{RS+Fmax}$ fully corresponds to one of two criteria (as equation 2.26 shows) when loading increases.

In the case depth, this maximal residual shear stress along the XY plane $\tau_{max}^{RS\_XY}$ is negative. This value reduces the effective maximal shear stress $\tau_{max}^{RS+Fmax}$, and helps to increase the maximum loading. On the other hand, this value is tensile in the over-tempering region, which increases the effective maximal shear stress $\tau_{max}^{RS+Fmax}$ and reduces the maximum possible loading in that region.

4.4 Maximal loading and nucleation crack locations

According to the Alban (1986) work on gear fatigue tests, the nucleation crack risk in case depth appears at depths varying from 0.18 mm to 0.31 mm. In the following steps, the value of $\tau_{max}^{RS\_XY}$ at the nucleation crack, a range of $\tau_{max}^{RS\_XY}$ in the case depth from 0.18 mm to 0.31 mm, and a range of $\tau_{max}^{RS\_XY}$ at over-tempering region with a depth ranging from 0.18-0.31 mm below the case depth will be observed.

Table 4-2 presents the computational results of all cases of case depth variation, from 0.5 mm, 0.8 mm, 1.0 mm, and 1.2 mm to 1.8 mm and combined with tensile hydrostatic stress peaks of 100 MPa, 200 MPa, 250 MPa and one case depth of 2.4 mm with 250 MPa of $\sigma_H^{T\_RS}$ peaks specially adjusted to show the local optimum of maximum loading in case of 250MPa peaks. In this table, the results determined the criteria attained for maximum pressure, maximum loads, and nucleation crack positions.

The nucleation crack positions are predicted most of the time at the maximal residual shear stress on the axial–radial plane. Nucleation cracks occurred in depths ranging from

0.25-0.31 mm in case depth or in the over-tempering region just below the case depth thickness (0.10-0.31 mm below); see column (f) and (a) in Table 4-2.

The case depth of 1.2 mm with the maximum load of 2170 N reaches two criteria at the same time. In the depth of 0.308 mm, the A criterion, in case depth, reaches the depth of 1.44 mm, the B criterion reaches the over-tempering region.

Table 4-2 shows that the 1.2 mm of case depth with the maximum load of 2170 N reaches two criteria at the same time. At a depth of 0.31 mm, the A criterion is reached in case depth, while at a depth of 1.44 mm, the B criterion is reached in the over-tempering region.

In the induction hardened case, nucleation crack positions will be observed under maximal loading conditions. Under this critical load, the maximal residual shear stress on the axial–radial plane was observed with the aim of determining a maximal residual shear limit. The nucleation cracks remained at depths of 0.24-0.31 mm in the case depth; in over-tempering region, the nucleation cracks occurred in depths ranging from 0.10-0.31 mm below the case depth, (see column (f) and (g), Table 4-2).

By observing the $\tau_{max}^{C\_RS\_XY}$ of column (i) and (k), a limit of $\tau_{max}^{C\_RS\_limit}$ is proposed at -100 MPa to prevent nucleation in the case depth. It means that if a compressive maximal shear stress in the area of 0.18-0.31 mm below the contact surface is higher than -100 MPa, the case depth is not the most critical region and the nucleation crack will have occurred in depth ranging from 0.10-0.31 mm below the case depth in the over-tempering region.

Table 4-2 Results: Summary of all simulations for residual stress variation by $\sigma_H^{T\_RS}$ peaks (MPa) and case depth thicknesses (mm)

CDT-Case depth (thickness (mm))	$\sigma_H^{T\_RS}$ in tensile peaks (MPa)	$\sigma_H^{C\_RS}$ in compressive peaks (MPa)	F_{max},Maximum loading, (N)	p_0,Maximum pressure, (GPa)	Nucleation cracks positions (mm) in depth	Nucleation cracks layers	Reached criterion	$\sigma_H^{RS\_XY}$ at nucleation crack	$\tau_{max}^{RS\_XY}$ at nucleation crack	$\tau_{max}^{RS\_CD\_XY}$ at 0.18-0.31 mm (MPa)	$\tau_{max}^{RS\_OT\_XY}$ at (case depth to CD+	Cases number
(a)	(b)	(c)	(d)	(e)	(f)	(g)	(h)	(j)	(i)	(k)	(l)	
0.5	100	-264	-875	2.21	0.51	OT*	B**	50	48	-150 -100	48 80	(1)
0.8	100	-194	-1675	2.87	0.81	OT	B	-14	-2	-106 -100	-2 75	(2)
1.0	**100**	**-177**	**-1760**	**2.91**	**0.26**	**CD**	**B**	**-170**	**-88**	**-88 -87**	**0 63**	(3)
1.2	**100**	**-143**	**-1720**	**2.80**	**0.29**	**CD**	**B**	**-145**	**-59**	**-57 -60**	**-23 -24**	(4)
1.8	**100**	**-102**	**-1750**	**2.63**	**0.27**	**CD**	**B**	**-112**	**-20**	**-17 -23**	**-27 -3**	(5)
0.5	200	-638	-545	1.76	0.74	OT	A	200	167	-370 -300	-56 168	(6)
0.8	200	-482	-1080	2.46	0.98	OT	A	198	146	-270 -240	69 146	(7)
1.0	200	-377	-1816	2.99	1.24	OT	A	197	125.5	-194 -190	31 126	(8)
1.2	**200**	**-316**	**-2170**	**3.14**	**0.31 (B)** 1.44(A)	**CD (B)** OT (A)	**B** A	**-310** 198	**-150** 113	**-145** -150	**23** 115	(9)
1.8	**200**	**-217**	**-1691**	**2.75**	**0.24**	**CD**	**B**	**-225**	**-58**	**-53 -63**	**-34 56**	(10)
0.5	250	-773	-320	1.35	0.80	OT	A	250	203	-442 -356	-97 203	(11)
0.8	250	-625	-355	1.40	0.99	OT	A	247	182	-352 -309	129 185	(12)
1.0	250	-500	-825	2.16	1.24	OT	A	248	156	-261 -248	75 161	(13)
1.2	250	-418	-1345	2.70	1.44	OT	B	249	142	-197 -200	55 143	(14)
1.8	**250**	**-256**	**-2070**	**2.75**	**0.30**	**CD**	**B**	**-280**	**-62**	**-45 -62**	**-57 10**	(15)
2.4	**250**	**-220**	**-1280**	**2.64**	**0.22**	**CD**	**B**	**-190**	**2**	**8 -12**	**-63 -15**	(16)

** A is the Dang Van criterion; B is the torsional fatigue limit criterion; * OT: Over-tempering region; CD: Case-depth

$\tau_{max}^{RS\_CD\_XY}$: Maximal residual stress of case depth in plane XY (plane of maximal shear stress due to rolling loading)

$\tau_{max}^{RS\_OT\_XY}$: Maximal residual stress of over-tempering region in XY plane (plane of maximal shear stress due to rolling load).

On the other hand, if the tensile maximal residual shear stress $\tau_{max}^{T\_RS\_XY}$ is greater than 110 MPa under tension, the nucleation cracks will appear at the over-tempering region too.

By observing the $\tau_{max}^{RS\_OT\_XY}$ of column (l) and (g), a limit of $\tau_{max}^{T\_RS\_limit}$ is proposed at 110 MPa to prevent nucleation in the over-tempering region, at a depth of 0.10-0.31 mm below the case depth (in the over-tempering region). This means that if a maximal residual shear stress $\tau_{max}^{RS\_OT\_XY}$ in the area of 0.1-0.31 mm below case depth is greater than 110 MPa, then nucleation will occurred in the over-tempering region and in the depth, including 0.10-0.31 mm below the case depth.

If the maximal residual shear stress $\tau_{max}^{RS\_XY}$ in the case depth is greater than -100MPa under compression (0.25-0.31 mm in case depth) and greater than 110 MPa in the over-tempering region (0.10-0.31 mm below case depth), the nucleation crack will occurred in the over-tempering region first and possibly at case depth (case (9): 1.2 mm in case depth and 200 MPa in $\sigma_H^{T\_RS}$ peak). If the maximal residual shear stress $\tau_{max}^{RS\_XY}$ in the case depth is smaller than -100MPa under compression (0.25-0.31 mm in the case depth) and smaller than 110 MPa in the over-tempering region (0.10-0.31 mm below case depth), the nucleation crack will occurred at the case depth (case (10)-1.8 mm in case depth and 200 MPa in $\sigma_H^{T\_RS}$ peak). The analysis of nucleation crack position and the maximal loading as a function of case depth thickness and residual stress follows in the next section.

4.4.1 Nucleation crack positions as a function of maximal residual shear stress

4.4.1.1 Nucleation cracks at case depth

For all cases, this section concentrates on nucleated cracks in the case depth with some remarks on some $\tau_{max}^{RS\_XY}$ condition limits and case depth. These conditions concern large case depths (greater than 1.0 mm).

Table 4-3 shows results for nucleation cracks in case depth. In all cases, the depth at which the cracks take place is between 0.24-0.31 mm below the surface contact. It can be said that the higher compressive maximal residual shear stress $\tau_{max}^{RS\_XY}$ is, the deeper the nucleation crack location. In the case of (10) and (15), for which the maximal pressure p_0 is in the same range (2.75 GPa) and for the same case depth, the $\tau_{max}^{RS\_XY}$ is different and the nucleation point locations are different. In case (10), $\tau_{max}^{RS\_XY}$ is lower (absolute value) than in (15). Therefore, the nucleation point of (10) is closer to the contact surface than in (15) (0.24 mm compared to 0.31 mm, respectively).

In the case of a homogenous material, the Hertz theory predicts that higher pressure results in deeper nucleation cracks, but in the presence of RS this rule does not apply anymore, as seen in case (3) and case (4). For case (3) with a maximal pressure of 2.91 GPa, the nucleation crack depth is 0.26 mm; for case (4) with a maximal pressure of 2.80 GPa, the nucleation crack depth is 0.29 mm, and therefore lower than for case (3). These results may be caused by the decreasing $\tau_{max}^{RS\_XY}$ in case depth (-59 MPa compare to -88 MPa, respectively).

The same can be said for the case depth, a deeper case depth does not necessary result in a shallower nucleation points. An overview of all cases shows that case (4) compares to case (5); case (9) compares to (10); and case (15) compares to case (16). Case (4) has a lower case depth than case (5) (1.2 mm compared to 1.8 mm, respectively) and the nucleation crack position of case (4) is deeper than that of case (5) (0.29 mm compared to 0.27 mm respectively). The same remark repeats for case (9) /case (10) comparison, (case depth of 1.2 mm/1.8 mm and 0.31 mm/0.24 mm as nucleation crack depth). These results mean that when there is a maximal residual shear stress influence on nucleation cracks, the more case depths are thinner, the more the maximal residual shear stresses in case depth increase (from -58 MPa to -150 MPa, case (10) compared to case (9)) and that this value reduces the more the effective maximal shear stress increases. The maximal load can increase to a greater level (maximal load increases from -1691 N (case 10) to -2170 N (case 9)) while reducing the case depth thickness from 1.8 mm to 1.2 mm. The maximal loading increases from case (10) to case (9) then the nucleation crack moves deeper, that is farther from contact surface.

Table 4-3 Limit of nucleation points at case depth

CDT-Case depth thickness (mm)	$\sigma_H^{T\_RS}$ in tensile peaks, (MPa)	$\sigma_H^{C\_RS}$ in compressive peaks (MPa)	F_{max},Maximum loading (N)	p_0,Maximum pressure (GPa)	Nucleation cracks positions (mm)	$\sigma_H^{RS\_XY}$ at nucleation crack point	$\tau_{max}^{RS\_XY}$ at nucleation crack point	$\tau_{max}^{RS\_CD\_XY}$ at 0.18-0.31 mm	$\tau_{max}^{RS\_OT\_XY}$ at (case depth to CD+0.31 mm)	Cases number
(a)	(b)	(c)	(d)	(e)	(f)	(j)	(i)	(k)	(l)	
1.0	100	-177	-1760	2.91	0.26	-170	-88	-88 -87	0 63	(3)
1.2	100	-143	-1720	2.80	0.29	-145	-59	-57 -60	-23 -24	(4)
1.8	100	-102	-1750	2.63	0.27	-112	-20	-17 -23	-27 -3	(5)
1.2	200	-316	-2170	3.14	0.31	-310	-150	-145 -150	23 115	(9)
1.8	200	-217	-1691	2.75	0.24	-225	-58	-53 -63	-34 56	(10)
1.8	250	-256	-2070	2.75	0.30	-280	-62	-45 -62	-57 10	(15)
2.4	250	-220	-1280	2.64	0.22	-190	2	8 -12	-63 -15	(16)

When RS is present in the rolling part, the amplitude $\tau_{\max}^{\mathrm{RS\_XY}}$ directly affects the maximal shear stress and the maximal shear stress affects the maximal loading, especially in case depth. In this region, where there is a high compressive residual stress, coupled to high compressive hydrostatic stress resulting from loading and residual stress, the maximal shear stress directly affects the fatigue criterion (criterion B). The greater the residual compressive maximal shear stress $\tau_{\max}^{\mathrm{RS\_XY}}$, the more the effective shear stress $\tau_{max}^{(RS+Fmax)\_XY}$ fails to reach criterion B. This observation explains case (9) where the maximal compressive residual shear stress $\tau_{\max}^{\mathrm{RS\_XY}}$ (-150 MPa) is the highest of all simulated cases. Thus this case (9) has the highest maximal load (-2170 N or 3.14 GPa as maximal pressure).

4.4.1.2 Nucleation cracks at over-tempering region

Similarly, nucleation crack results appearing in the over-tempering region are discussed below. These conditions are related to low case depths (lower than 1.0 mm).

Cases (1), (2), (6-9), (11-14) are displayed in Table 4-4. As mentioned in the section before, a limit of maximal tensile residual shear stress $\tau_{max}^{T\_RS\_limit}$ is proposed at 110 MPa to prevent nucleation in the over-tempering region, at a depth of 0.10-0.31 mm below the case depth adjacent (over-tempering region). Upon observation of column (i) and (l), these remarks are validated for all cases, except case (1) and (2). The particular cases (1) and (2) with $\tau_{\max}^{\mathrm{T\_RS\_XY}}$ less than 110 MPa under tension in the over-tempering region are relevant: their $\tau_{\max}^{\mathrm{C\_RS\_XY}}$ in the case depth are enough and reach the limit of 100MPa under compression, thus the nucleation crack still occurred in the over-tempering region.

Table 4-4 Limit of nucleation points in the over-tempering region

CDT-Case depth thickness (mm)	$\sigma_H^{T\_RS}$ in tensile peaks (MPa)	F_{max},Maximum loading , (N)	p_0,Maximum pressure , (GPa)	Nucleation cracks positions (mm) in depth	$\sigma_H^{RS\_XY}$ at nucleation crack point (MPa)	$\tau_{max}^{RS\_XY}$ at nucleation crack point (MPa)	$\tau_{max}^{RS\_CD\_XY}$ at 0.18-0.31 mm (MPa)	$\tau_{max}^{RS\_OT\_XY}$ at (case depth to CD+ 0.31 mm)	Cases number
(a)	(b)	(d)	(e)	(f)	(j)	(i)	(k)	(l)	
0.5	100	-875	2.21	0.51	50	48	-150 -100	48 80	(1)
0.8	100	-1675	2.87	0.81	-14	-2	-106 -100	-2 75	(2)
0.5	200	-545	1.76	0.74	200	167	-370 -300	-56 168	(6)
0.8	200	-1080	2.46	0.98	198	146	-270 -240	69 146	(7)
1.0	200	-1816	2.99	1.24	197	125.5	-194 -190	31 126	(8)
1.2	**200**	**-2170**	**3.14**	**1.44**	**198**	**113**	**-145 -150**	**23 115**	(9)
0.5	250	-320	1.35	0.80	250	203	-442 -356	-97 203	(11)
0.8	250	-355	1.40	0.99	247	182	-352 -309	129 185	(12)
1	250	-825	2.16	1.24	248	156	-261 -248	75 161	(13)
1.2	250	-1345	2.70	1.44	249	142	-197 -200	55 143	(14)

For the same case depth, case (1), case (6), case (11) with increasing tensile residual hydrostatic stress σ_H^{RS} peaks from 100, 200 to 250 MPa, the higher the σ_H^{RS} peaks and lower the maximal pressures (from 2.21 GPa to 1.35 GPa, comparing case (1) with case (11)). The same

observations are made for a case depth of 0.8 mm (case (2), (7), (12)), and for a case depth of 1 mm (case (8) and (12)).

By observation of column (i) and column (a) for each tensile residual hydrostatic stress σ_H^{RS} peaks of 100, 200 and 250 MPa, the more the case depth increases, the more the maximal residual stress in the over-tempering region decreases under tension, the more the maximal pressure increases. For example, in case (6) and case (7), column (i) shows decreasing maximal residual shear stress under tension in the over-tempering region. This tension reduces slightly, from 167 MPa to 146 MPa. Thus the effective maximal stress could be increased by a greater margin and this leads to a maximal load increase from -545 N to -1080 N, and the nucleation crack position is deeper (0.74 mm compare to 0.9 mm, respectively).

In all cases, (6-9), (11-14), the nucleation crack position is nearly the same as the tensile residual hydrostatic stress σ_H^{RS} peak position (see column (j) where the tensile hydrostatic residual stress in axial radial plane $\sigma_H^{RS\_XY}$ reaches peak, compared to column (b)), except for cases (1) and (2). By observation of column (k), for all cases, it can be seen that at depths ranging from 0.18 mm to 0.31 mm in the case depth, the compressive residual shear stress $\boldsymbol{\tau_{max}^{RS\_XY}}$ is greater than the limit of 100 MPa under compression, so the case depths are safe and the nucleation crack potential in the over-tempering region is high. Columns (f) and (a) show that nucleation cracks in the over-tempering region remain within the range of 0.10-0.31 mm, below the case depth.

In presence of RS in the rolling part, the nucleation crack location, the maximal loading has to be considering the amplitude of $\tau_{max}^{RS\_XY}$. This factor of $\tau_{max}^{RS\_XY}$ decides the nucleation crack position and the maximal loading under pure rolling contact conditions. These $\tau_{max}^{RS\_limit}$ value limits present as a half of the difference between the axial residual stress value and the radial residual stress in the maximal shear stress plane (due to rolling load) value. These figures are considerably observed in two specific depths, ranging from 0.24-0.31 mm below the contact surface, and from 0.10-0.31 mm below the case depth in the over-tempering region. For increasing the maximal loads under heat treatment induction, the residual stress in part have to

insure that: the axial residual stress under compression in case depth, in the region of 0.24-0.31 mm below the surface contact, must be increased, while the difference of axial residual stress under tension and radial residual stress under tension in the over-tempering region, at a depth 0.10-0.31 mm below case depth, must be reduced.

4.4.2 Nucleation cracks as a function of case depth and $\sigma_H^{T\_RS}$ peaks

Figure 4-3 shows the overall view of nucleation crack positions and case depth thicknesses. In case of 100 MPa of tensile hydrostatic RS with case depth thickness lower than the **1.0 mm**, the nucleation crack will appear in the over-tempering region and their depth depends almost linearly on this region. The case depth nucleation cracks stay in the area of 0.26-0.31 mm below the contact surface. The over-tempering region nucleation will generate cracks at different distances from those in the case depth, depending on the intensity of the tensile hydrostatic stress peaks: the higher the peak intensity, the deeper below the case depth the nucleation point will be (for 100 MPa, 0.81 mm; for 200 MPa, 1.43 mm and for 250 MPa, 1.41 mm). Whereas the softer material layer in the part represents the weaker region in terms of fatigue properties using the maximum shear stress criterion; the tensile residual stress present in this region strongly influences the position of the nucleation crack position and the performance of the treated surface.

To better understand the relation of case depth thickness and nucleation crack position Figure 4.3 should have considered with Figure 4.2. With the case depth thickness greater than 1.2 mm, the compressive residual hydrostatic stresses reach low values in the transformed region. This results in crack nucleation according to the B criterion (limits by torsion fatigue limit of the hard material - 60 HRC) in the case depth. On the other hand, with a thin case depth thickness inferior than 1.2 mm, they are two possibilities: or the compressive residual hydrostatic stresses below the surface are significant and failure will happen in the over-tempered region according to the B criterion (limits by torsion fatigue limit of the soft material - 38 HRC), or the compressive residual hydrostatic stresses below the surface are an similar to the one found for large case depth and failure will happen in the over-tempered region according to the B

criterion value then this later reduce successful the maximal shear stress below the contact surface due to rolling load but the over-tempering region approaches more the contact surface (cause of thin case depth thickness) then the tensile residual hydrostatic stress in over-tempering region will be act to Dang Van limit (A) under a low rolling load.

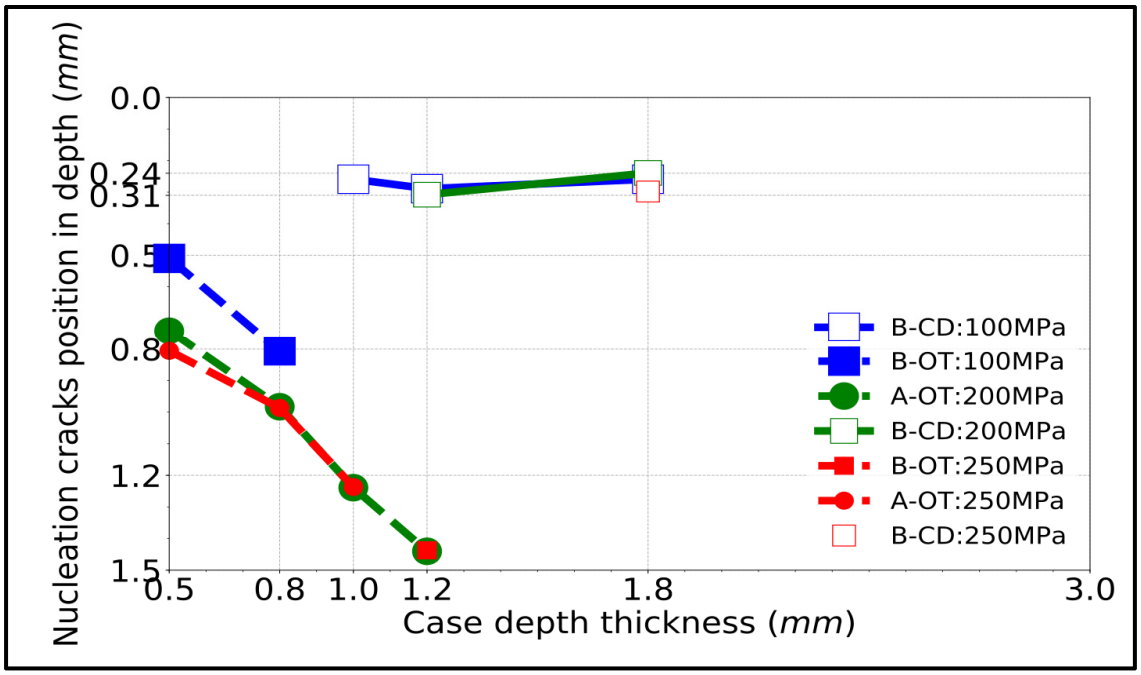

Figure 4-3 Function of nucleation crack position as a functions of case depth thickness (mm). B- Torsional fatigue limit criterion; A- Dang Van limit; filled marker: nucleation crack in over-tempering region; blank marker: nucleation crack in case depth; blue: 100 MPa of $\sigma_H^{T\_RS}$ peaks; green: 200 MPa of $\sigma_H^{T\_RS}$ peaks; red: 250 MPa of $\sigma_H^{T\_RS}$ peaks

4.4.3 Nucleation crack location as a function of τ_{max}^{RS} at nucleation point

Figure 4-4 shows an overall view of the nucleation crack position in relation to maximal shear residual stress in the axial radial plane at nucleation crack position and tensile hydrostatic stress peaks of 100 MPa, 200 MPa and 250 MPa.

In the case of the maximal compressive residual stress at the nucleation crack point (in the left of Figure 4-4), the compressive maximal residual shear stress $\tau_{max}^{RS\_XY}$ does not significantly affect the nucleation crack position in the case depth.

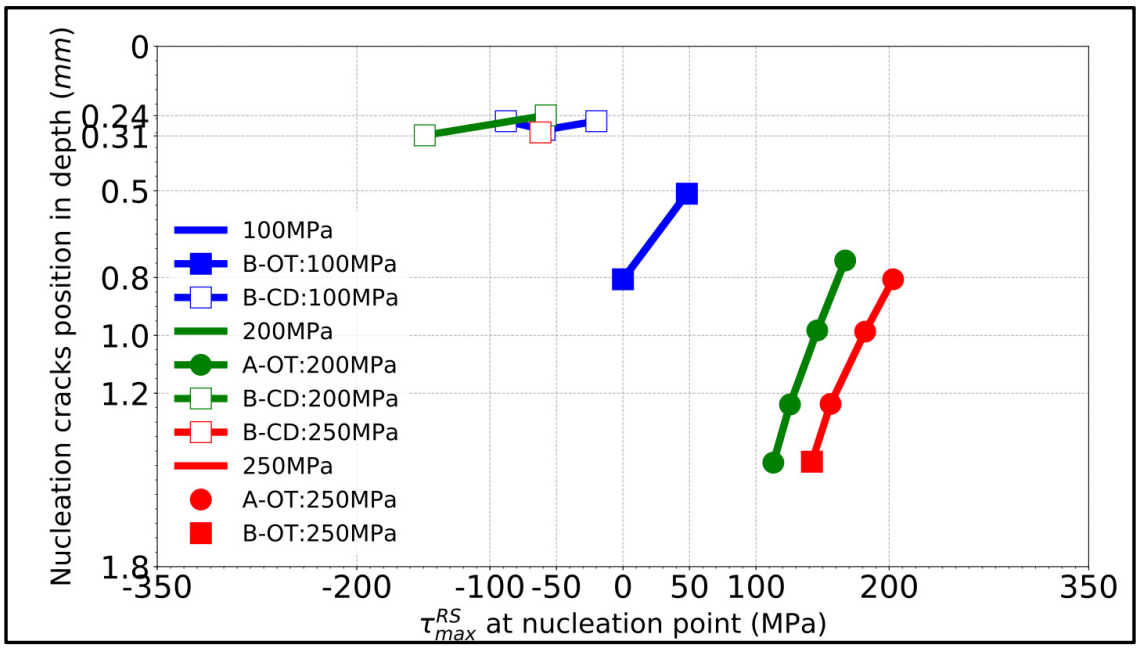

Figure 4-4 Nucleation cracks position in depth vs. maximal residual shear stress at nucleation point $\tau_{max}^{RS\_XY}$. B- Torsional fatigue limit criterion; A- Dang Van limit; filled marker: nucleation crack in over-tempering region; blank marker: nucleation crack in case depth; blue: 100 MPa of $\sigma_H^{T\_RS}$ peaks; green: 200 MPa of $\sigma_H^{T\_RS}$ peaks; red: 250 MPa of $\sigma_H^{T\_RS}$ peaks

For the tensile maximal residual shear stress (in right of Figure 4-4), the peaks of σ_H^{RS} increases (increases from the blue line, 100 MPa, to the red line, 200 MPa), the nucleation cracks occur deeper in the over-tempering region. For each line (same σ_H^{RS}peaks), the more the τ_{max}^{RS} at nucleation crack point under tension increases, the more the nucleation crack position in over-tempering region moves up to the case depth. On the other hand, for the nucleation crack position in the over-tempering region, the more the case depth thickness decreases, the more the shallowness of the nucleation crack point increase, up to case depth/over-tempering adjacent. Under the σ_H^{RS} peak of 100 MPa (the inclined blue line), it can be seen that when the case depth decreases from 0.8 mm to 0.5 mm, the τ_{max}^{RS} at nucleation crack point increases

from 0 to 50 MPa (approximately). The same observations can be made for the inclined green line (σ_H^{RS} peaks of 200 MPa). When the case depth decreases from 1.2 mm to 0.5mm, the τ_{max}^{RS} at nucleation crack point increases from 113 MPa to 167 MPa, approximately.

4.4.4 Nucleation crack position as a function of tensile residual hydrostatic stress σ_H^{RS} at nucleation point

Figure 4-5 shows an overall view of the nucleation crack position in relation to tensile hydrostatic residual stress at nucleation point, the case depth effect on nucleation point in over-tempering region and the compressive hydrostatic residual stress effect on the nucleation point in case depth.

In the case of the compressive hydrostatic residual stress at the nucleation crack point (in the left of Figure 4-5), the nucleation cracks will occur at depths ranging from 0.24-0.31 mm below the contact surface. For many cases of nucleation in the case depth, the compressive hydrostatic residual stress does not significantly affect the nucleation crack position.

For the tensile hydrostatic residual stress (in the right of Figure 4-5), the more the σ_H^{RS} peaks increase (from the blue line, 100 MPa, to the red line, 200 MPa), the nucleation cracks will occur deeper in the over-tempering region (below the case depth). For high tensile hydrostatic residual stress (200 MPa and 250 MPa), the nucleation crack position depends on the peak σ_H^{RS} figure. This means that the nucleation crack points will occur at the peak σ_H^{RS} position. In these cases of nucleation cracking in the over-tempering region, the nucleation crack positions depend on case depth thicknesses and tensile hydrostatic residual stress σ_H^{RS}peak positions.

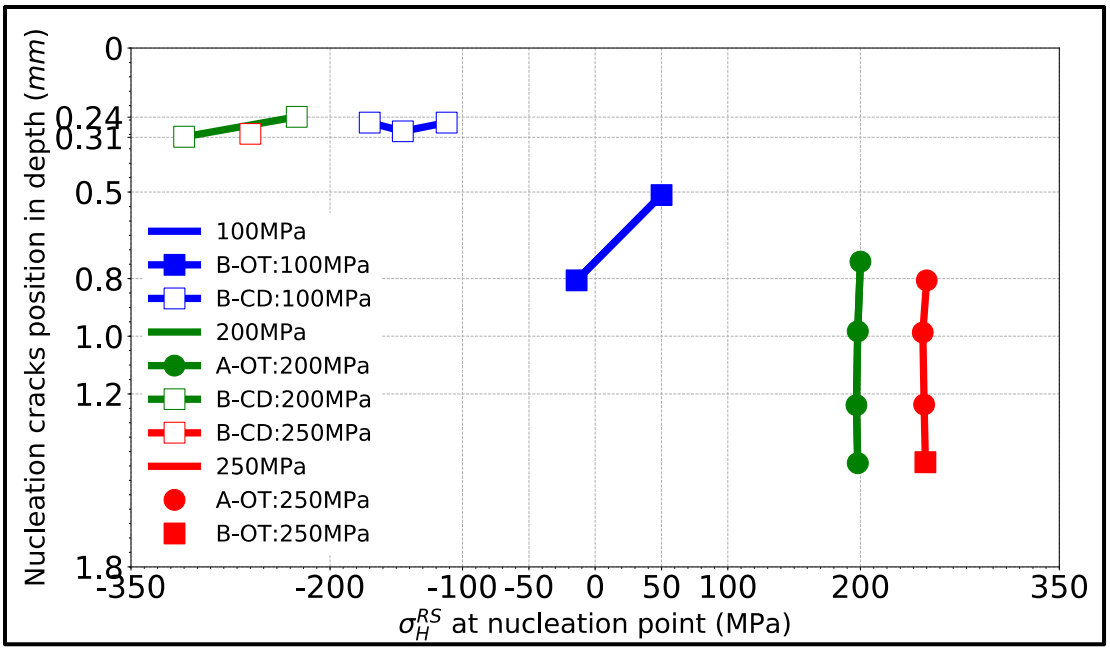

Figure 4-5 Nucleation crack position as a function of hydrostatic residual stress at nucleation point. B- Torsional fatigue limit criterion; A- Dang Van limit; filled marker: nucleation crack in over-tempering region; blank marker: nucleation crack in case depth; blue: 100 MPa of $\sigma_H^{T\_RS}$ peaks; green: 200 MPa of $\sigma_H^{T\_RS}$ peaks; red: 250 MPa of $\sigma_H^{T\_RS}$ peaks)

4.4.5 Maximal pressure as a function of case depth and tensile hydrostatic RS peaks

Figure 4-6 shows the variation of maximum pressures for different tensile hydrostatic stresses as a function of case depth thickness. Figure 4-6 shows that the maximum pressure in all cases tends towards a stable limit of 2.64 GPa for large case depths. The maximum pressure is 3.14 GPa for a 1.2 mm case depth and 200 MPa of tensile residual hydrostatic stress peaks.

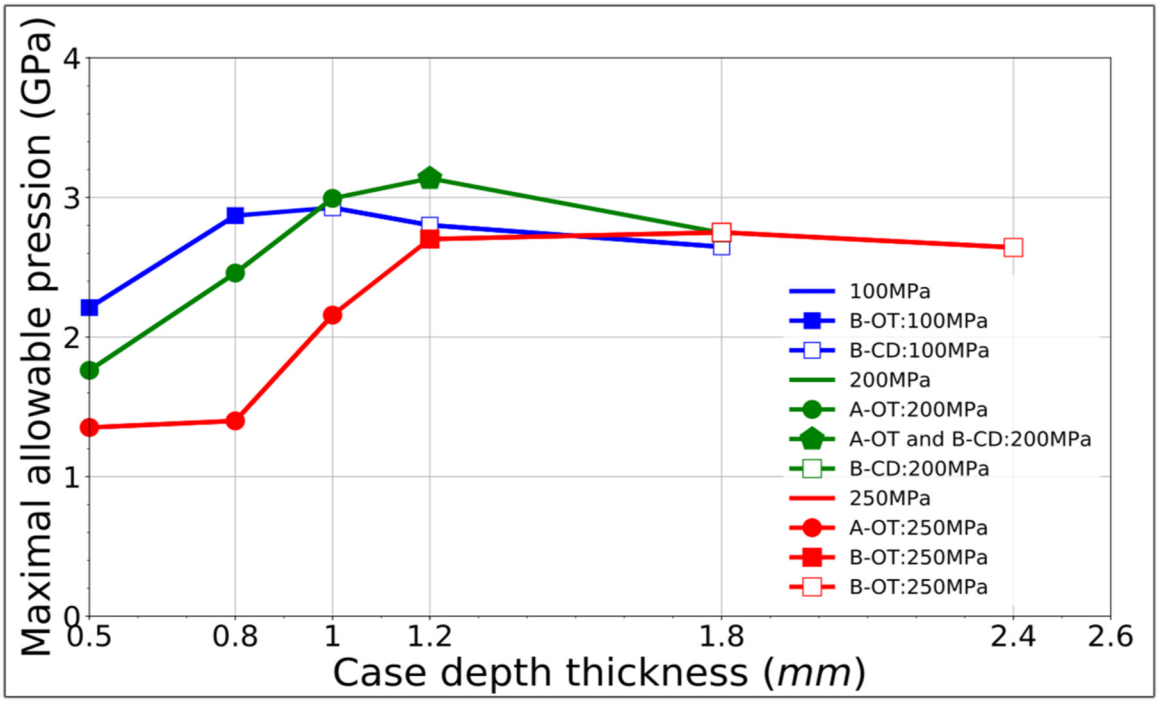

Figure 4-6 Maximum pressure (GPa) as a function of hydrostatic residual stress at nucleation point. B- Torsional fatigue limit criterion; A- Dang Van limit; filled marker: nucleation crack in over-tempering region; blank marker: nucleation crack in case depth; blue: 100 MPa of $\sigma_H^{T\_RS}$ peaks; green: 200 MPa of $\sigma_H^{T\_RS}$ peaks; red: 250 MPa of $\sigma_H^{T\_RS}$ peaks)

The Figure 4-6 shows that the optimum maximal contact pressure is for a case of 1.2 mm and 200 MPa in tensile hydrostatic stress peaks. The optimum pressure is 3.14 GPa. This figure demonstrates that the maximal pressure depends on the residual stress in piece and the case depth thickness. With the thin case depth, the maximal pressure varies with a large amplitude from 1.3 GPa to 2.8 GPa thanks to the RS in compression presence in the piece in case depth. The tension hydrostatic stress in the over-tempering region approaches the crack nucleation condition with Dang Van criterion (A). In the large case depth (greater than 1.2 mm), the low compressive residual hydrostatic stress at case depth could not be enough to reduce the maximal shear stress due to rolling contact load. On the other hand, the tensile hydrostatic stress of over-tempering region is far enough below the contact surface then the maximal shear stress nucleation type will appear in case depth according to the B criterion (maximum shear stress).

Figure 4-7 shows the maximum allowable evolution for different tensile hydrostatic stresses as a function of case depth thickness. In all cases, the maximum load as a function of case depth thickness reaches a local optimum before tending to decrease. In the case of 100 MPa of $\sigma_H^{T\_RS}$ peak, the maximal loads decrease after reaching the local optimum and merely to a stable limit of 1750 MPa in increasing case depth thickness greater than 0.8 mm. In the case of a 200 MPa of $\sigma_H^{T\_RS}$ peak, the local optimum of maximal loading is 2170 N. In the case of a 250 MPa of $\sigma_H^{T\_RS}$ peak, the local optimum of maximal loading is 2170 N at a case depth of 1.8 mm. With $\sigma_H^{T\_RS}$ peaks of 200 MPa, the case depth of 1.2 mm is the optimal thickness which also gives the absolute maximum load of 2170 N, (see Figure 4-7).

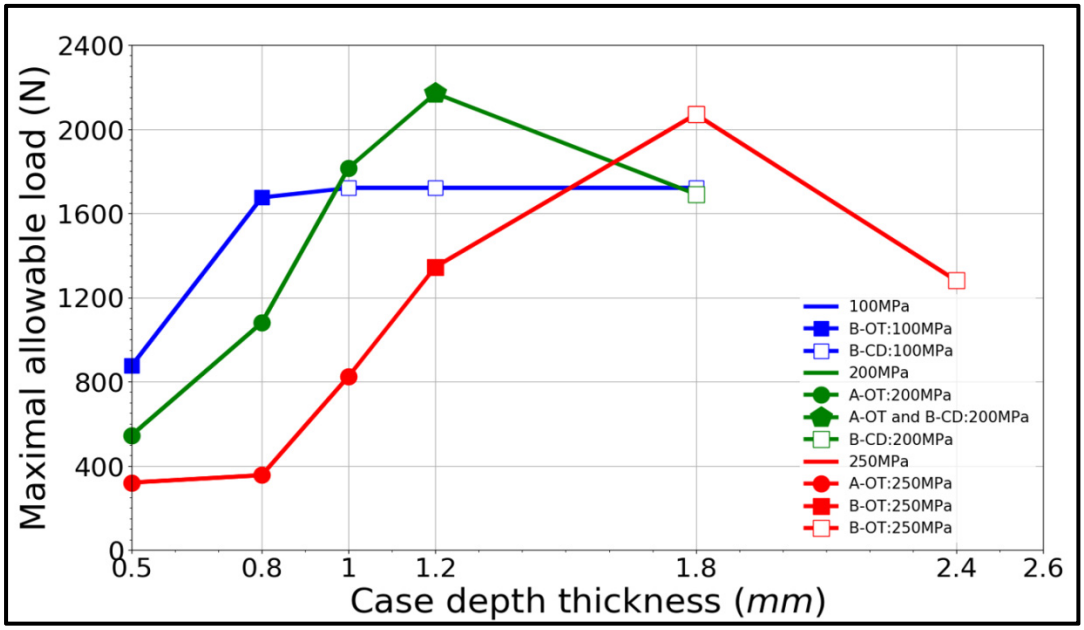

Figure 4-7 Maximum loads (N) as a function of case depths and tensile hydrostatic stress peaks (MPa). B- Torsional fatigue limit criterion; A- Dang Van limit; filled marker: nucleation crack in over-tempering region; blank marker: nucleation crack in case depth; blue: 100 MPa of $\sigma_H^{T\_RS}$ peaks; green: 200 MPa of $\sigma_H^{T\_RS}$ peaks; red: 250 MPa of $\sigma_H^{T\_RS}$ peaks)

4.4.6 Maximal load as a function of tensile residual hydrostatic stress peaks

Figure 4-8 also shows the maximum load of all cases is 2170 N with a case depth of 1.2 mm and 200 MPa tensile hydrostatic stresses.

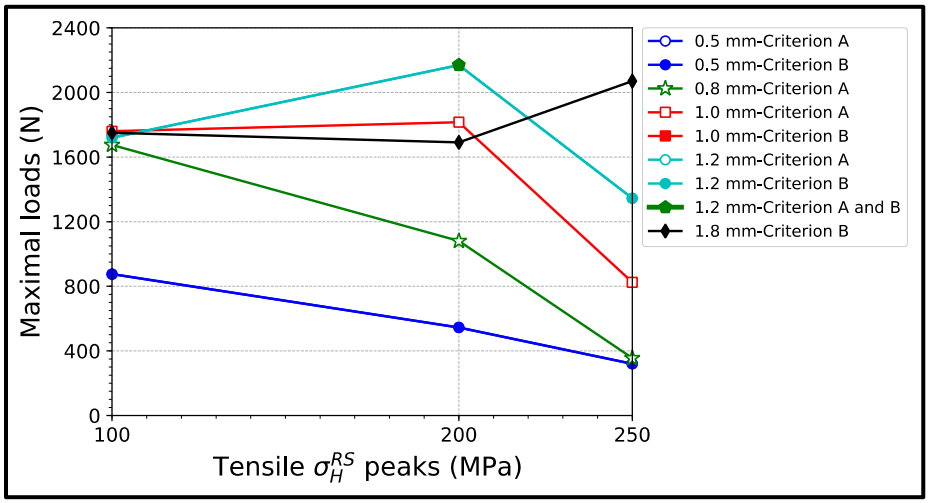

Figure 4-8 Maximum loads (N) as a function of case depths and tensile residual hydrostatic stress

Figure 4-8 and Figure 4-7 show the optimum maximal load for samples with 100 MPa in tensile hydrostatic stress peaks reach a plateau at 1.8 GPa. In the cases of 200 MPa in tensile hydrostatic stress peak, the maximal pressures vary from 1.8 GPa to 3.14 GPa. For higher tensile hydrostatic stress, the maximal pressure variation is reduced to 1.35 GPa to 2.75 GPa.

4.5 Comparison of induction hardening optimum case and through hardening (60 HRC)

Figure 4-9 compare the stress' evolution below the contact surface for 1.2 mm of case depth and 200 MPa in tensile hydrostatic stress peak and the through hardening of 60 HRC without RS. The induction hardening allows 1.65 times more loading than through hardening 60 HRC case (3.75 times than an initial homogenous part of 48 HRC). The compressive residual

stresses move the loading surface point toward the higher compressive hydrostatic stress, allowing the part to resist to higher loads than homogeneous case.

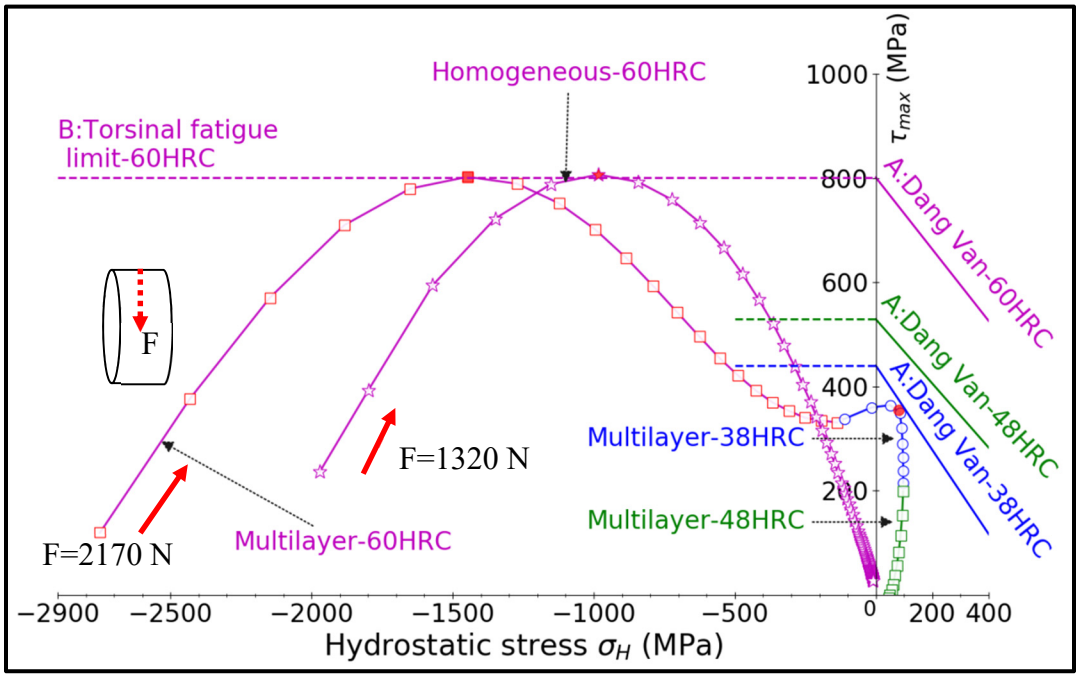

Figure 4-9 Evolution of stresses when applying the critical loading condition on a multilayer cylinder with the residual stress gradient typical of induction hardening, corresponding to maximum loadings of 2170 N and through hardening of 60 HRC (homogeneous case without RS)

Table 4-5 shows the maximal loadings, maximal pressures, reached fatigue criteria of two these cases. In the induction the nucleation crack is in over-tempering region by tensile hydrostatic stress (A) and is in case depth by maximal shear stress limit of 801 MPa (B).

Table 4-5 Maximal loading in induction hardening optimum case and homogeneous part of 60 HRC without RS

	Induction hardening optimum case (1.2 mm CD, 200 MPa $\sigma_H^{T\_RS}$ peak	Homogenous case without RS, 60 HRC
Loads (N)	2170	1320
Maximum pressure, p_0 (GPa)	3.14	2.56
Maximum shear stress, τ_{Max} (MPa)	801	801
Nucleation depth (mm) (criterion B)	0.298	0.248
l_{min}	$3.24\ 10^{-2}$	0.447
l_{min} position (mm) in depth	1.44	0.452
σ_H max on loading (MPa) (at l_{min})	198≈ 200	-538
Shakedown value , $\frac{p_o}{\tau_e}$	3.91	3.19
Failure criteria	A or B	B

4.6 Conclusion

The optimum maximal contact pressure is reached for case of 1.2 mm of case depth thickness and 200 MPa in tensile hydrostatic stress peaks, the optimum pressure is 3.14 GPa. This chapter shows that the maximal contact pressure not only depend on surface hardness (chapter 3) but also depends on induction hardening case depth. The maximal contact pressure depends on the compressive hydrostatic residual stress near the contact surface, on the thickness of case depth, and the tensile hydrostatic residual stress in over-tempering region. Thin case depths contain a significant compressive residual stress at surface and high tensile hydrostatic stress, the later reacting with rolling loads to nucleate cracks in the over-tempering region by Dang Van nucleation type (A). Thick case depths (typically greater than 1.2 mm) contain less important compressive residual stress at surface. The over-tempering region being far from the surface contact, nucleation does not happen in this region but rather in case depth because the compressive residual stress does not reduce enough the shear stress generated by the rolling load. Crack nucleates according to maximal shear stress type (B) in case depth. Exceptionally, in the cases of 100 MPa in tensile hydrostatic stress peaks with thin case depths of 0.5 mm and 0.8 mm, the nucleation crack occurs at maximal shear stress in over-tempering region.

With induction hardening treatment, if the case depth is optimising as proposed in our study (1.2 mm with 200 MPa peaks of tensile hydrostatic stress), the maximal load allowable will increase by 3.75 times compare to an untreated part (at 48 HRC).

CONCLUSIONS

On effect of residual stress on maximum allowable loading:

The effects of induction hardening on Rolling Contact Fatigue (RCF) were successfully studied using FEA simulations for the frictionless contact condition. Two cylinders were put into contact using finite element analysis (FEA) in which residual stress and hardness gradients were introduced. A multiaxial fatigue model built based on the shakedown limit and a combination of a Dang Van criterion and torsional endurance limit was used to understand the impact of two aspects (residual stress and hardness variation) on the contact performance, and in particular, the maximum possible loading that prevents crack nucleation and propagation before 10^6 cycles.

For the material behaviour, it was considered that in higher negative hydrostatic stress conditions, the maximum shear stress value preventing crack nucleation is equal to the torsion endurance limit of the material and, in the condition of tensile hydrostatic stress, the model results in higher material hardness, increasing maximum loadings and deeper crack positions in the over-tempering region.

Deeper nucleation depths were actually found when the material hardness gradient generated after induction hardening was added to the model: nucleation therefore occurs in the over-tempered region of the part, in particular because torsion endurance limits are significantly lower in this region. In this maximal loading investigation case of (section 3.2), the nucleation mechanisms were predicted to activate according to the maximum shear stress limit but the Dang Van fatigue criterion was almost reached in this over-tempering region. A somewhat deeper location (in the over-tempered region) was predicted in this case and for some conditions, the tensile residual stress peak present in the over-tempered region was the key parameter promoting failure according to the Dang Van criterion.

The positive hydrostatic component introduced by the tensile peak of the residual stress profile reduces the distance to the Dang Van criterion, and can become the most critical parameter controlling the contact behaviour if the shakedown limit is not as conservative as the one proposed in the present work. Consequently, and in order to have a predictive model, a careful adjustment of the maximum shear stress fatigue limit in negative hydrostatic conditions has to be run; however, even with the present conservative hypothesis, the induction hardened component was found to have a maximum allowable loading, which was 2.4 times higher than that obtained with a non-treated one at 48 HRC.

On the effect of residual shear stress on nucleation crack positions:

The thinner the case depth, the residual stress in compression in case depth becomes higher. The compressive maximal residual shear stress does not significantly affect nucleation crack positions at case depth; the tensile maximal residual shear stress affects nucleation crack positions in the over-tempering region. The more the increase of the latter under tension, the shallower the nucleation cracks in the over-tempering region / case depth adjacent will be.

In case depth, the maximal compressive residual shear stress plays an important role in reducing the maximal shear stress, the higher this residual stress, the higher the maximal loading will be. The maximal compressive residual shear limit is -100 MPa under compression in case depths while the maximal tensile residual shear is 110 MPa for the over-tempering region in AISI 4340. In the case depth region, the compressive hydrostatic residual stress does not also affect nucleation crack positions, but in the over-tempering region, if the tensile hydrostatic residual stress peak is higher, the nucleation crack position will be deeper and farther from the below case depth adjacent. Under high tensile hydrostatic residual stress peak (such as 200 or 250 MPa), the nucleation crack will occur at tensile hydrostatic residual stress peak positions, below the case depth. The nucleation crack positions in the over-tempering region depend on the case depth thickness; the more the increase in case depth thickness, the deeper the nucleation crack positions.

Under pure rolling conditions, depending on maximal residual shear stress and maximal rolling load, nucleation cracks will appear in case depth, at a depth of 0.24-0.31 mm below the surface, and in the over-tempering region at a depth of 0.10-0.31 mm below case depth.

RECOMMENDATIONS

This work helps **to understand the effect of residual stress** on rolling contact fatigue under pure rolling conditions. This study successfully built a pure rolling model but this model could be made more realistic by introducing a contact surface sliding friction coefficient to observation a complete area contacts outside of the pitch line on contact flank gear. It is expected that the sliding effect will move the nucleation crack region closer to the contact surface in the case depth, due to higher applied stresses. Micropitting (of about 0-100 μm in depth) near the pitch line could also be generated by the sliding effect. The cylinder's radiuses could also be changed to simulate different points of the pitch line as the residual stress field varies from one location to the next in an induction hardened gear.

Future work should also be undertaken in order to validate the methodology and calibrate the material fatigue data (in particular the material behavior in the compressive hydrostatic regions). Rolling contact fatigue tests have been run under well controlled conditions. This will require the design and manufacturing of a dedicated rig and adequate cylinders, together with the development of proper surface treatments.

This study is based on a FEA simulation using the mechanical and fatigue data of AISI 4340 for a million cycles life. This methodology and this FEA modeling could adapt to another material and a new data extend to new level high cycle fatigue.

For the first time the minimum distance of the studied point to Dang Van limit was used to quantify fatigue properties in the non-proportional behaviour case of rolling contact. This work also has investigated for the first time the effect of tensile residual stress in surface treated parts. The consequence of the over-tempering region generated by induction hardening on rolling contact fatigue was also introduced for the first time in a rolling fatigue contact model.

APPENDIX I

CONVERGENCE STUDY

Maximal pressure error

Figure-A I-1 shows maximum pressure contact calculation errors from equation (2.10) for simulation by ANSYS software by variation of contact element size. The contact element size of 0.08 mm gives the maximum pressure is also close to the analysis results and reduces much more time of simulation than the 0.06 mm element size.

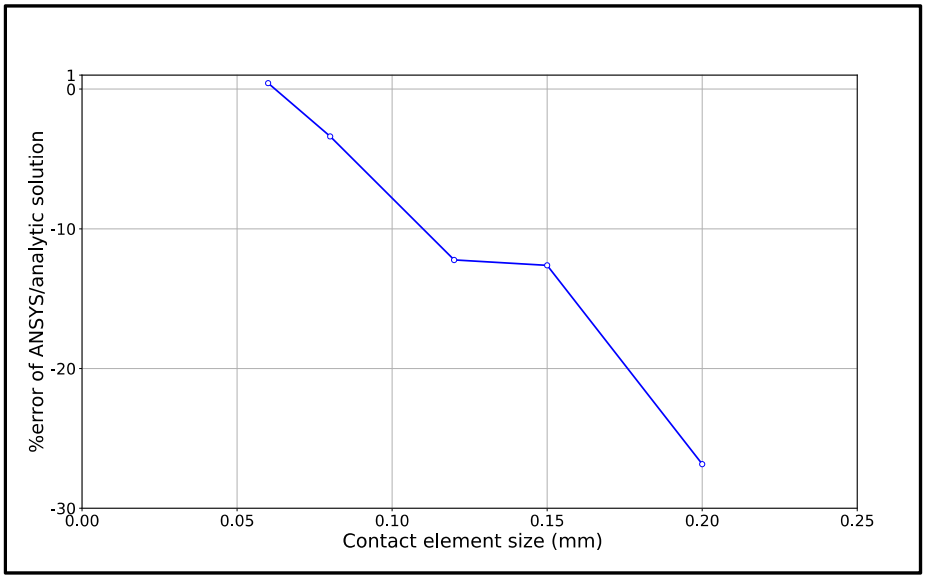

Figure-A I-1 Maximum pressure error of ANSYS in analysis as a function of contact element size

Mesh size

Figure-A I-2 presents the convergence study on the internal stress evolution in terms of shear stress versus hydrostatic stress for various mesh sizes. These variables were chosen for the optimization as they are the ones that define the critical condition for the onset of nucleation

crack fatigue 0.08 mm has been defined as the optimum size for the meshing in the contact region.

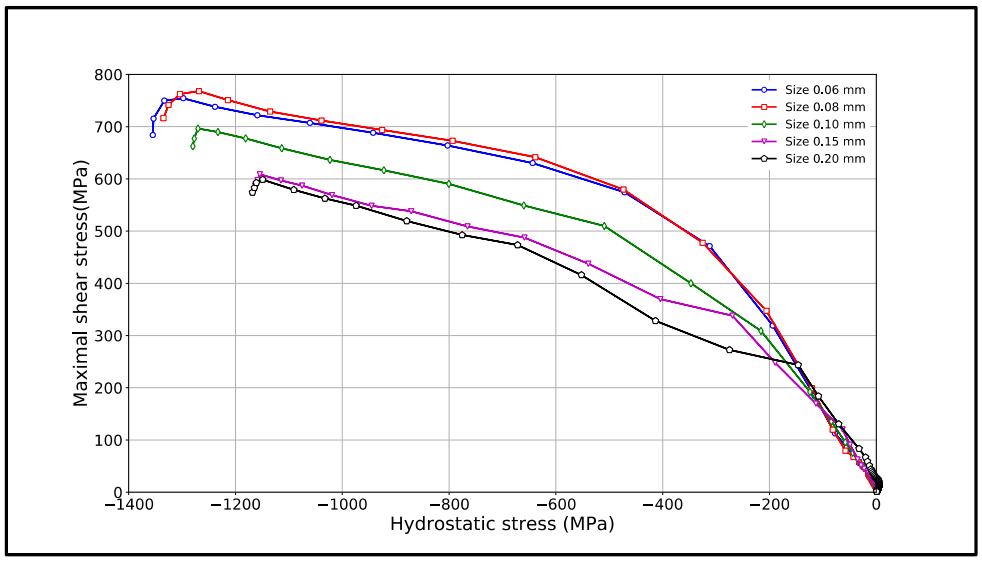

Figure-A I-2 Convergence study of the shear stress versus hydrostatic stress below the contact point

Validation of the stress field

The maximum principal stress distribution below the contact center point was studied against convergence as a function of mesh size. The resulting stress distribution is given in Figure-A I-3 below.

Figure-A I-3 shows the maximum principal stress convergence study, and demonstrates that with a mesh size of 0.08 mm in the contact region (surface and subsurface contact), the modeling is convergent.

The stress distribution obtained by the finite element analysis (FEA) simulation was compared to the ideal case calculated by the Hertz theory, and results are displayed in Figure-A I-3. The calculated stress distribution agrees well with the well-known theoretical stress profile.

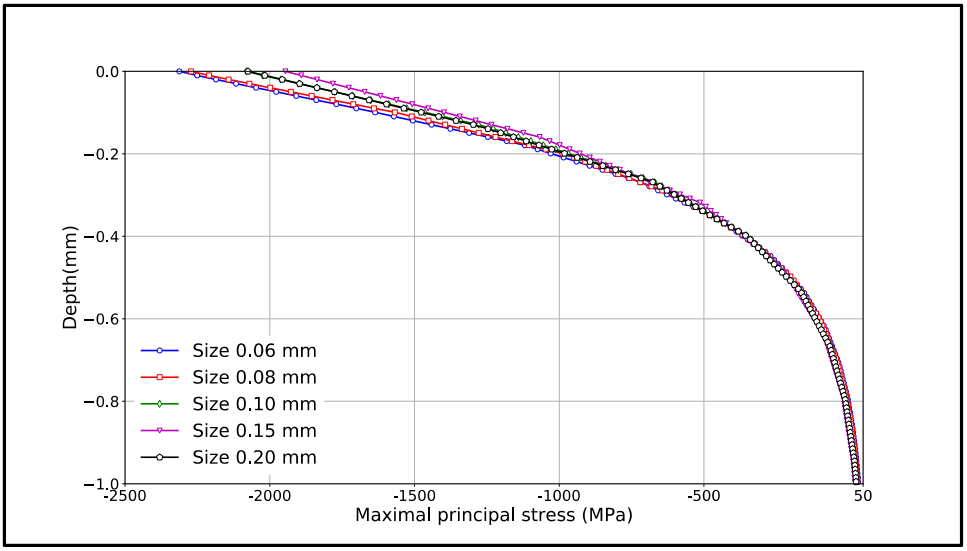

Figure-A I-3 Maximum principal stress at contact surface, at center contact by function of contact element size of two parallel cylinders

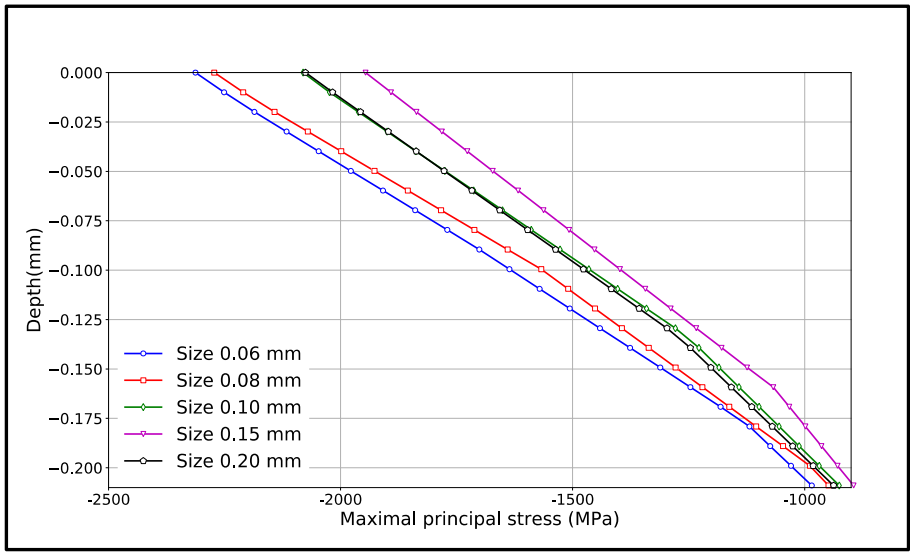

Figure-A I-3 Zoom out of maximum principal stress at contact surface, at center contact by function of contact element size

APPENDIX II

NUCLEATION CRACK REGION IN CASE OF 38 HRC, 48 HRC, 60 HRC AND 3 LAYERS

a) Without Residual Stress

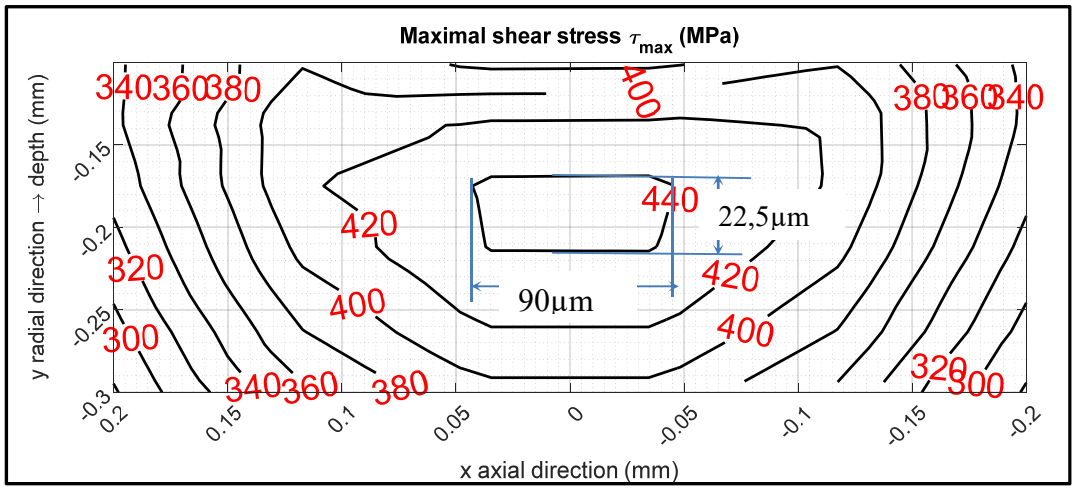

Figure-A II-1 Nucleation crack region of 38 HRC under 420 N, criterion B is reached at 440 MPa at a depth of 0.174 mm

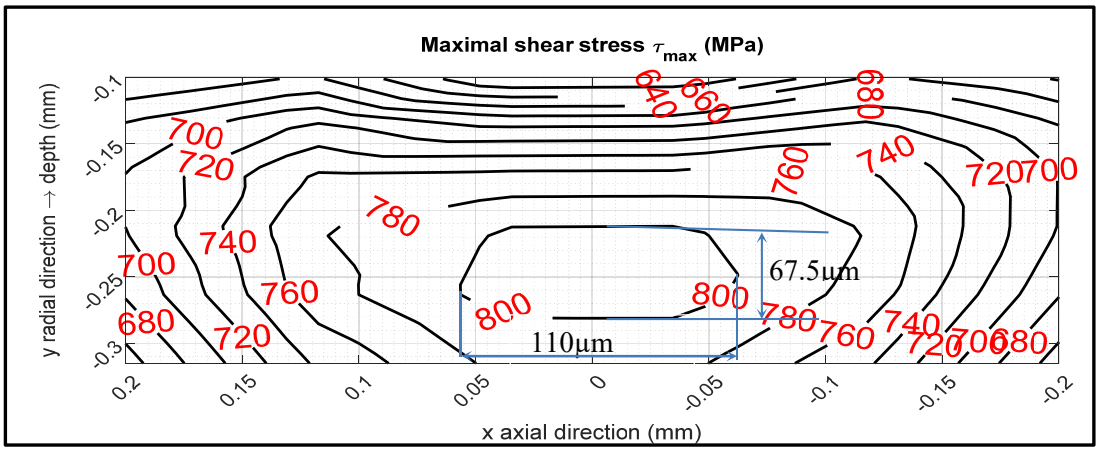

Figure-A II-2 Nucleation crack region of 60 HRC under 1320 N, criterion B is reached at 801 MPa at a depth of 0.248 mm

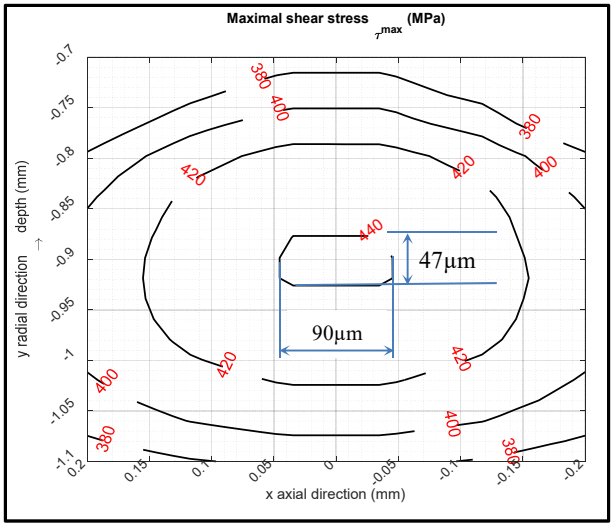

Figure-A II-3 Nucleation crack region of 3 layers under 1420 N in the over-tempering region at a depth of 0.894 mm, criterion B is reached at 440 MPa

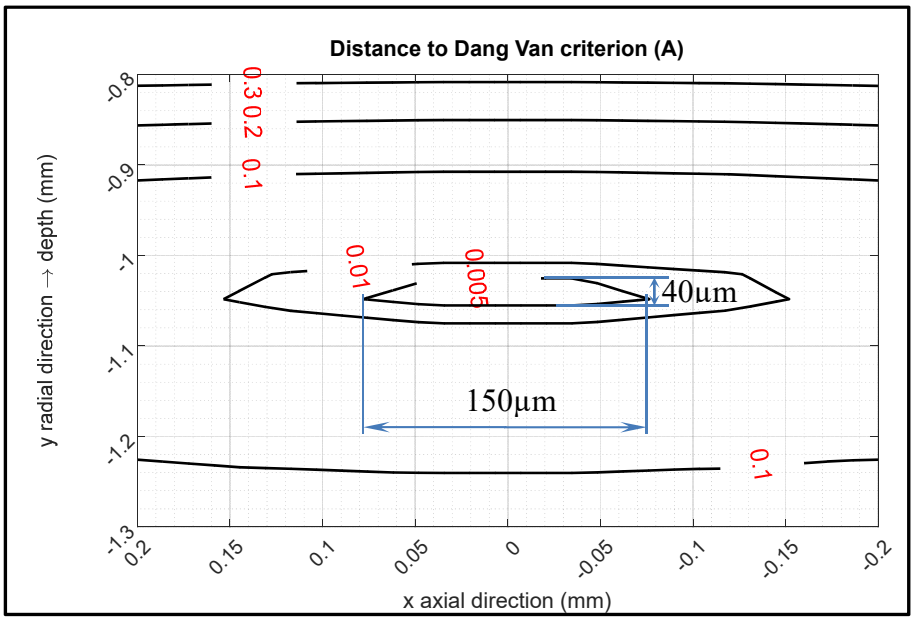

Figure-A II-4 Nucleation crack region of 3 layers under 1420 N in the over-tempering region at a depth of 0.1.043 mm of minimal distance $l_{min} = 0.005$, criterion A is reached at $l_{min} = 0.00273$

b) With residual stress

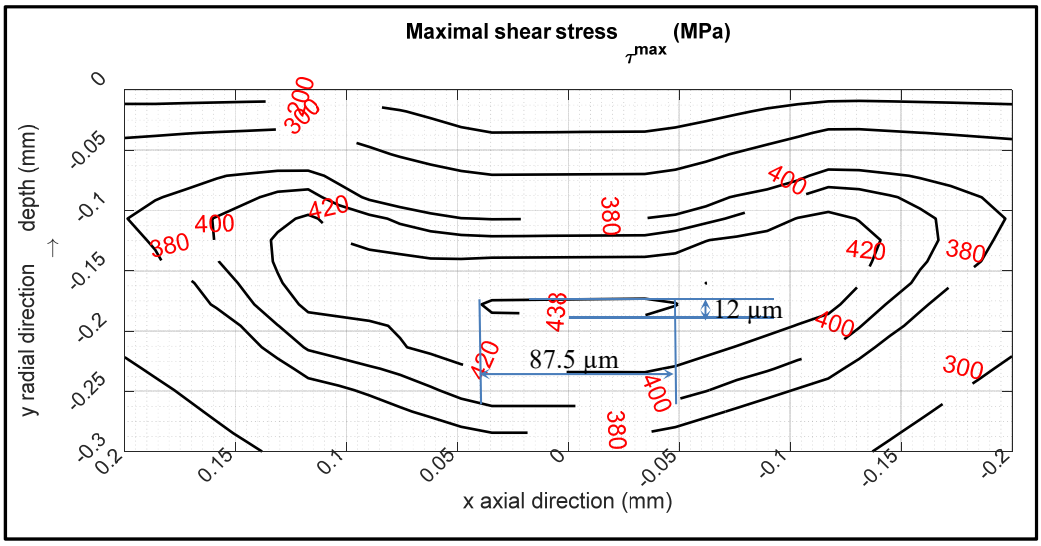

Figure-A II-5 Nucleation crack region of 38 HRC of 438 MPa under 840 N at a depth of 0.174 mm, criterion B is reached at 440 MPa

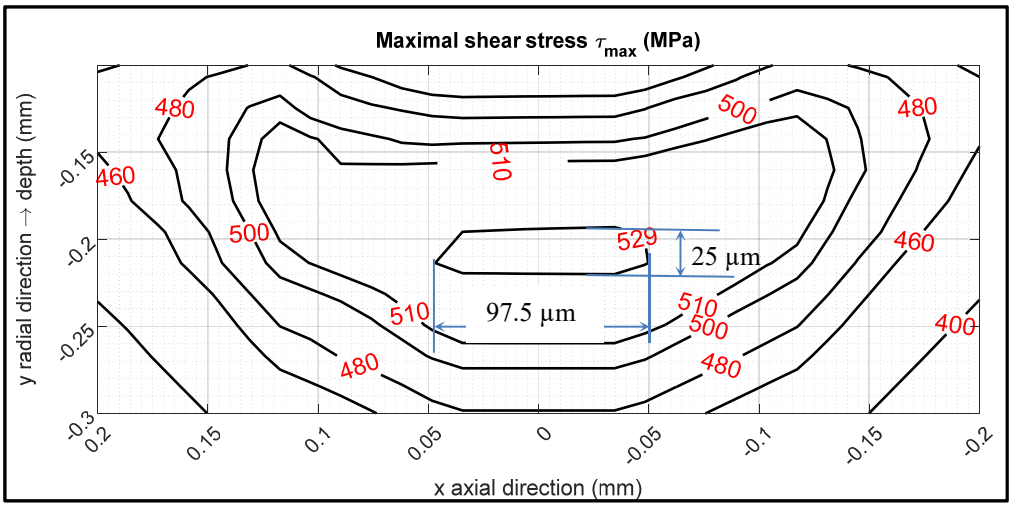

Figure-A II-6 Nucleation crack region of 48 HRC of 529 MPa under 1130 N at a depth of 0.199 mm, criterion B is reached at 529 MPa

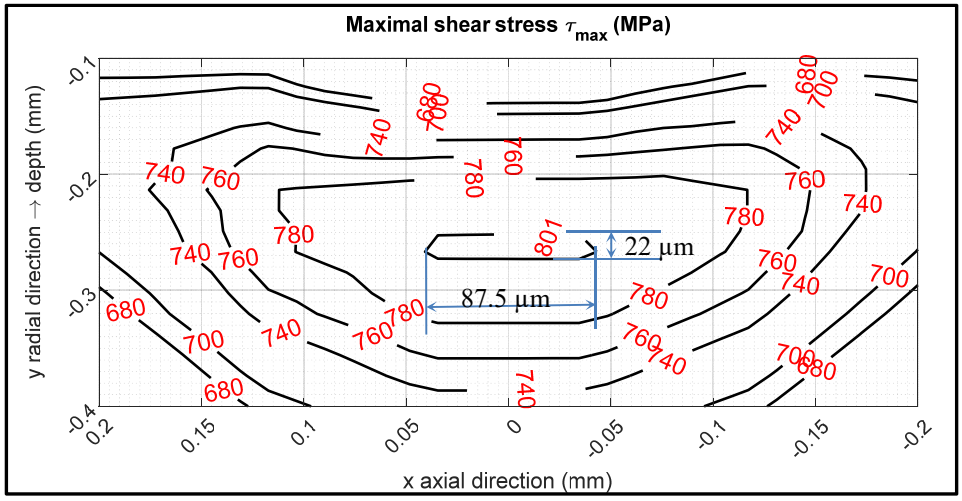

Figure-A II-7 Nucleation crack region of 60 HRC of 801 MPa under 2345 N at a depth of 0.273 mm, criterion B is reached at 801 MPa

APPENDIX III

RESIDUAL STRESS DUE TO INDUCTION HARDENING IN VARIATION OF CASE DEPTH THICKNESSES AND TENSILE HYDROSTATIC RS PEAKS

With a focus on studying the influence of case depth (CD) thickness in the tensile hydrostatic stress constant of 100 MPa, 200 MPa and 250 MPa, the Figures below show the varying of residual stresses (hydrostatic residual stress, maximal residual shear stress, axial residual stress) as a function of case depth and tensile hydrostatic residual stress peaks.

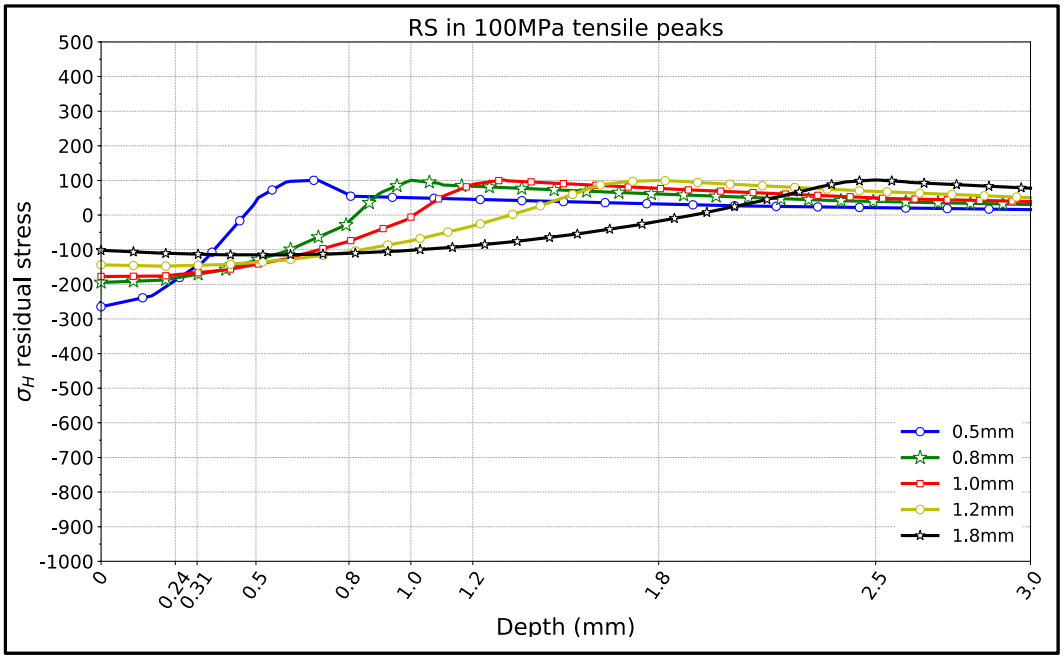

Figure-A III-1 Hydrostatic residual stress variation as a function of case depth, with 100 MPa tensile peaks

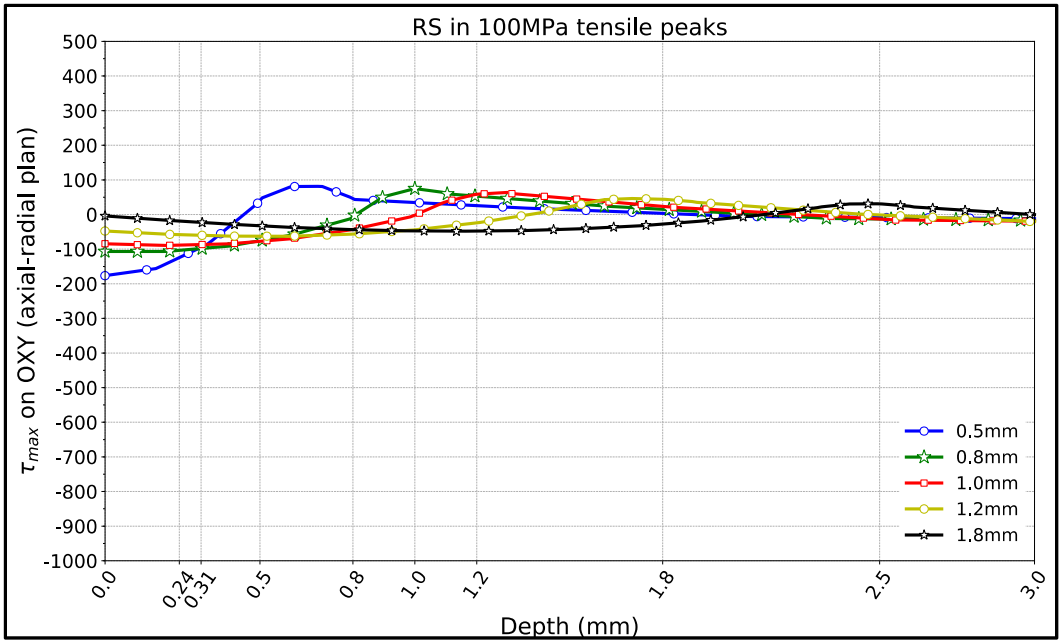

Figure-A III-2 Maximum residual shear stress in axial radial plane with 100 MPa tensile peaks, as a function of case depth

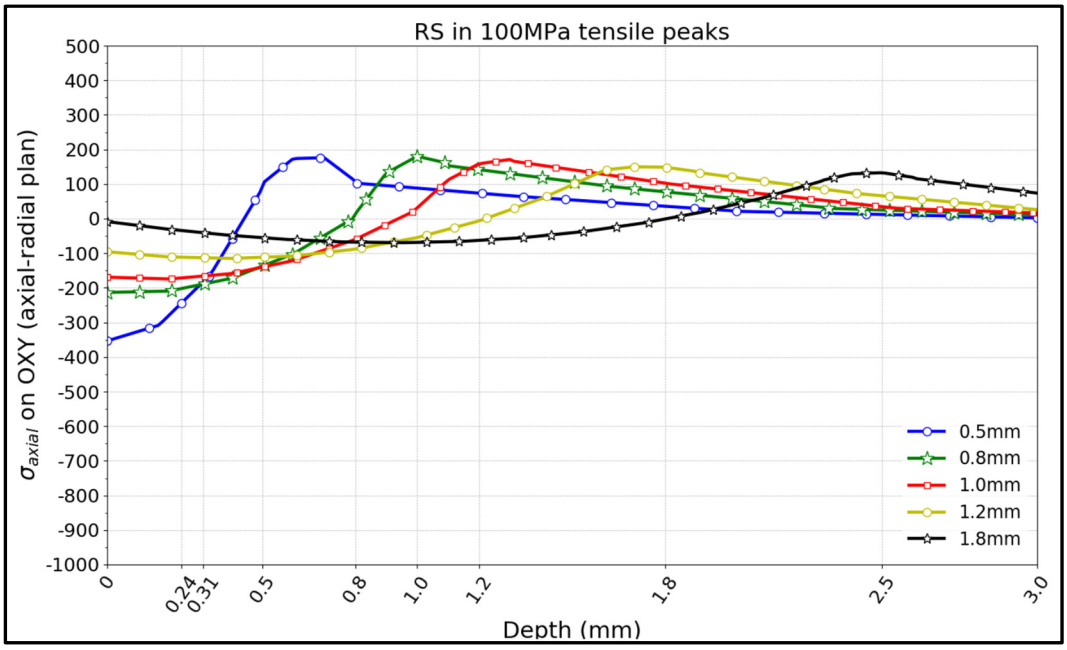

Figure-A III-3 Axial residual stress in axial -radial plane without loading, as a function of case depth, with 100 MPa tensile peaks

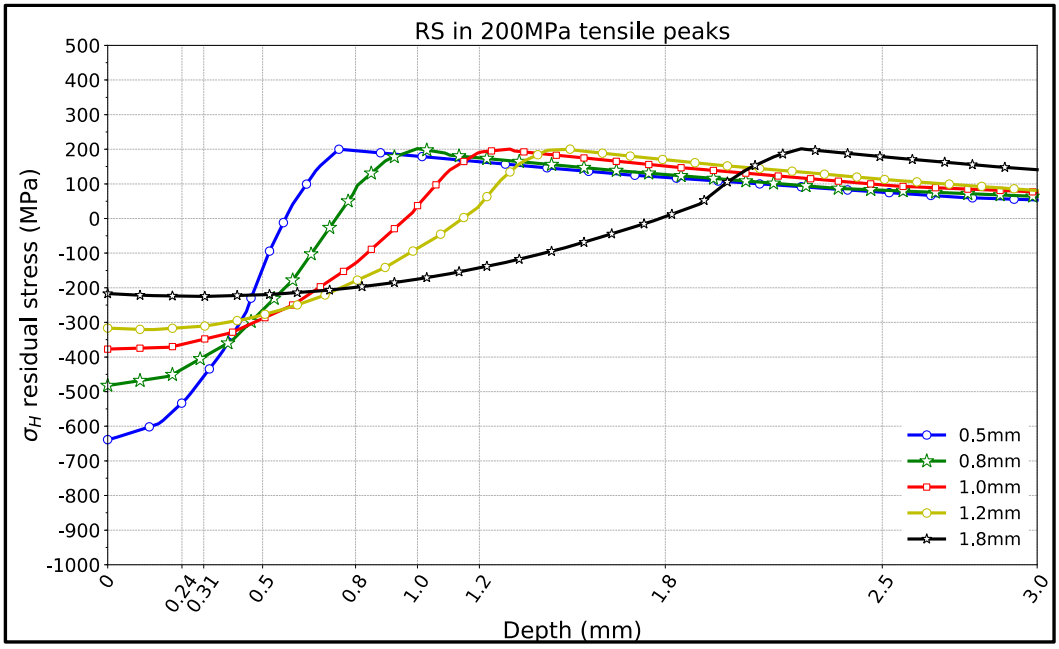

Figure-A III-4 Hydrostatic residual stress variation as a function of case depth, with 200 MPa tensile peaks

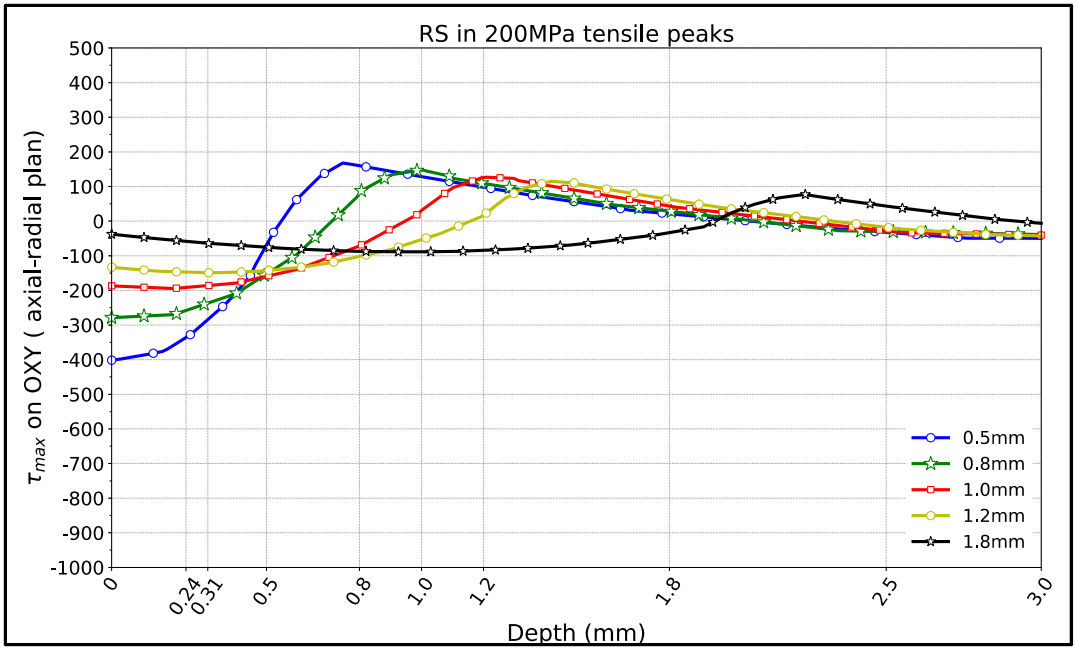

Figure-A III-5 Maximum residual shear stress in axial radial plane with 200 MPa tensile peaks, as a function of case depth

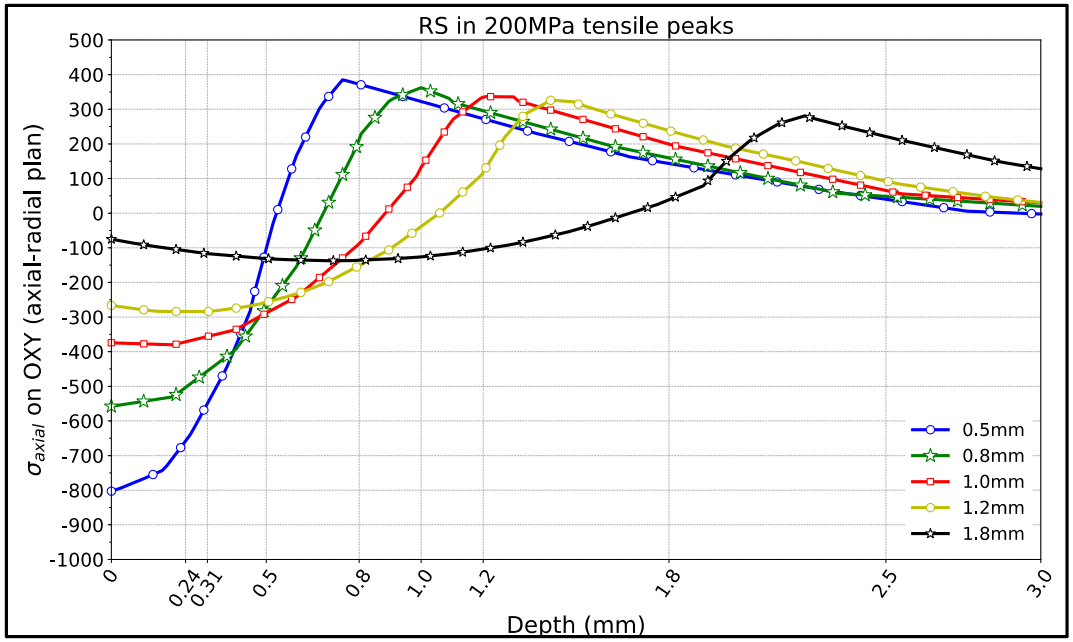

Figure-A III-6 Axial residual stress in axial -radial plane without loading, as a function of case depth, with 200 MPa tensile peaks

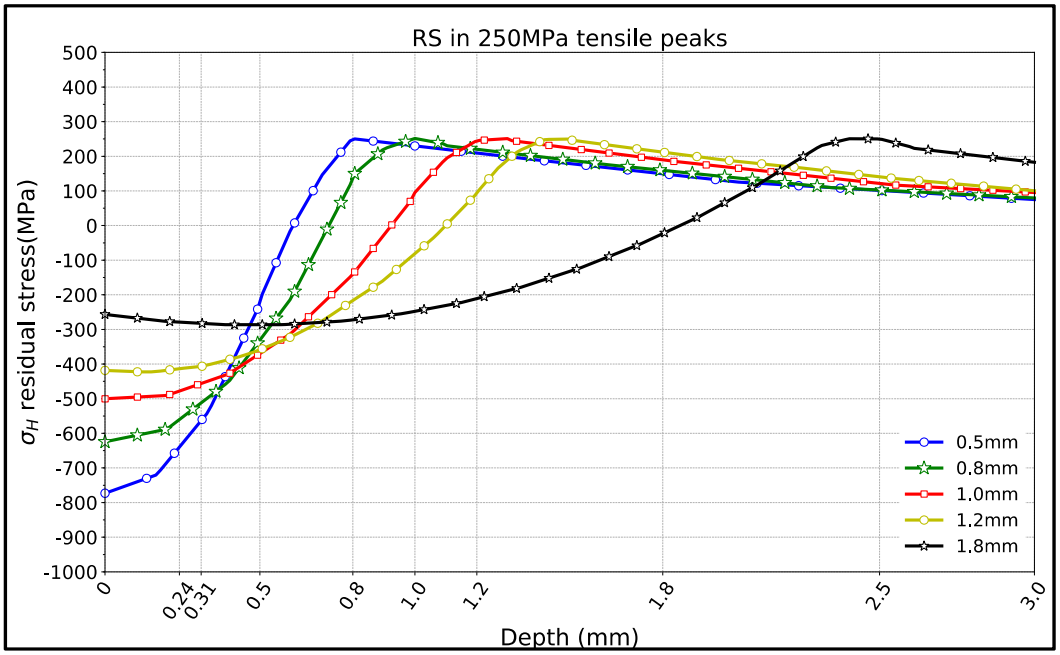

Figure-A III-7 Hydrostatic residual stress variation as a function of case depth, with 250 MPa tensile peaks

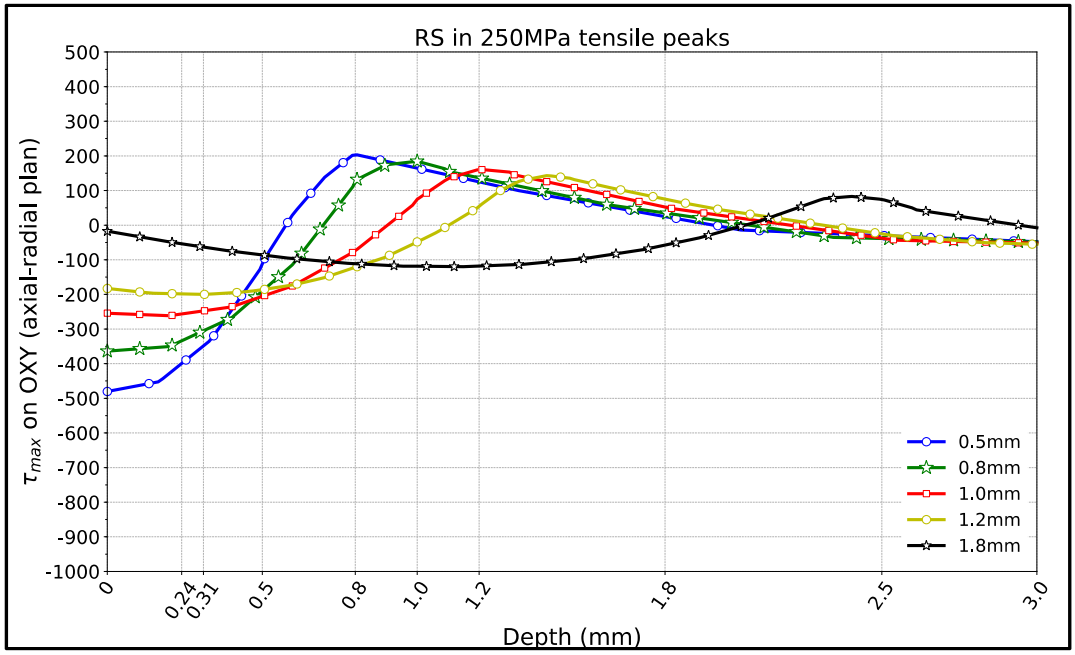

Figure-A III-8 Maximum residual shear stress in axial radial plane with 250 MPa tensile peaks, as a function of case depth

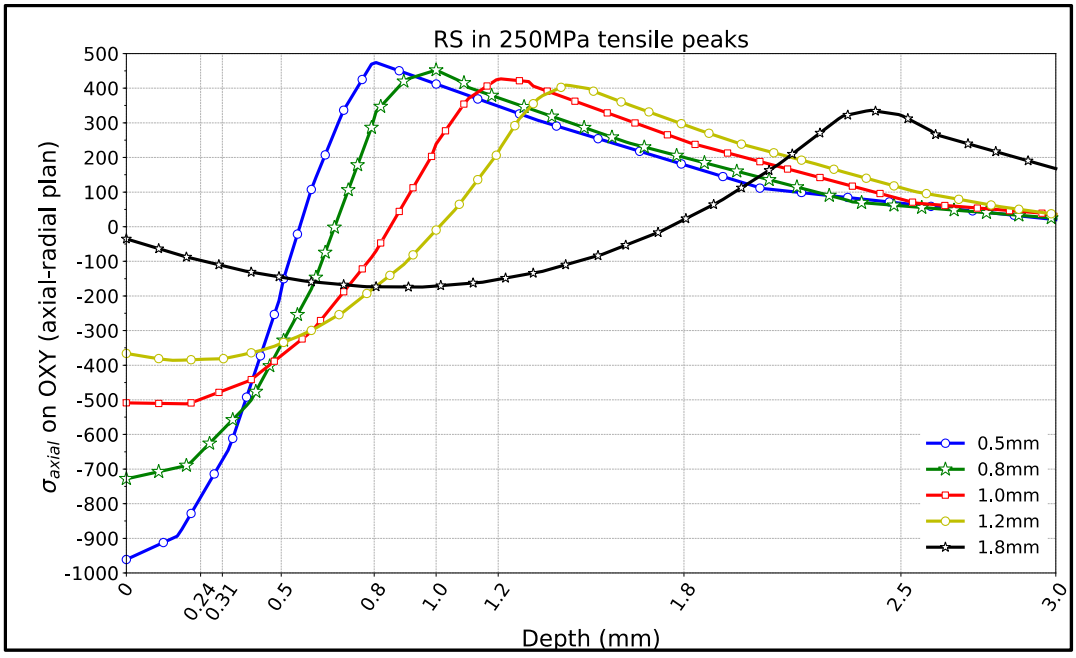

Figure-A III-9 Axial residual stress in axial -radial plane without loading, as a function of case depth, with 250 MPa tensile peaks

APPENDIX IV

MAXIMUM COMPRESSIVE RESIDUAL STRESS

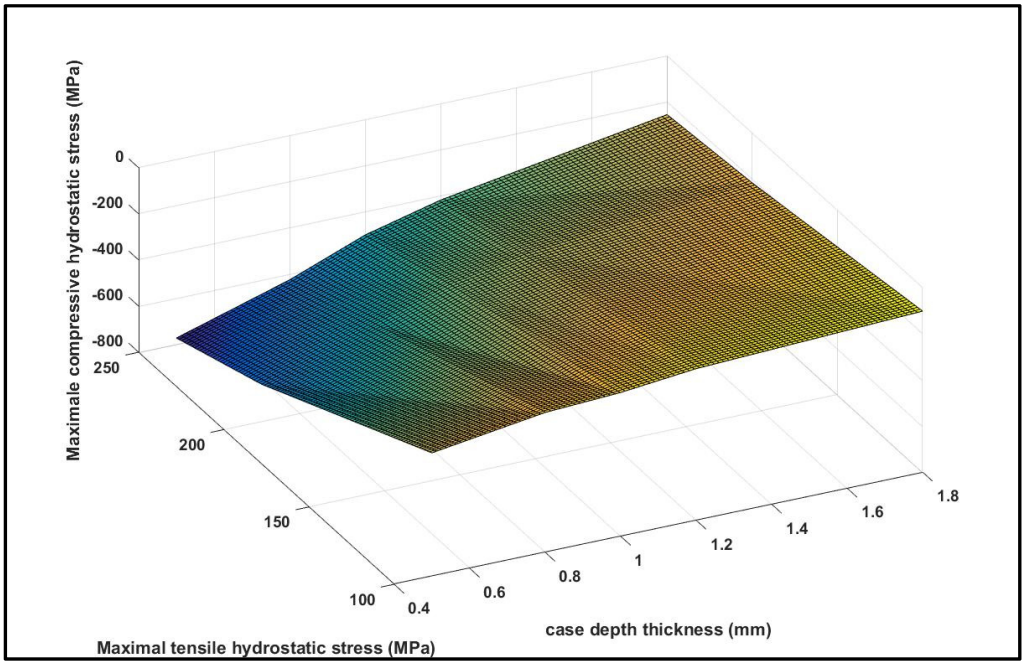

Figure-A IV-1 Maximum compressive residual stresses in variation of case depth thickness and tensile residual stress peaks (MPa)

APPENDIX V

MAXIMUM CONTACT PRESSURE

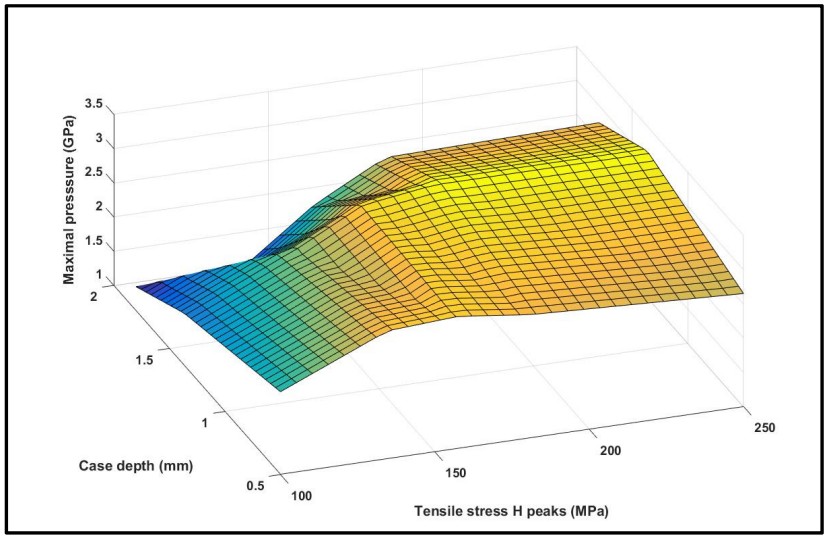

Figure-A V-1 Maximum pressure in contact as a function of case depth and tensile hydrostatic stress peaks

APPENDIX VI

NUCLEATION CRACK DEPTH

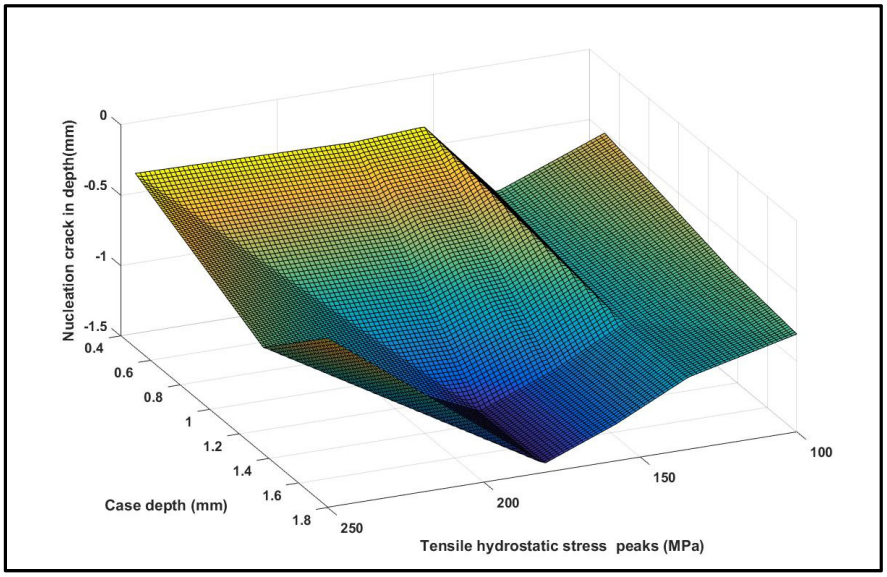

Figure-A VI-1 Nucleation crack in depth as a function of case depth and tensile hydrostatic stress peaks

APPENDIX VII

MAXIMAL LOADING

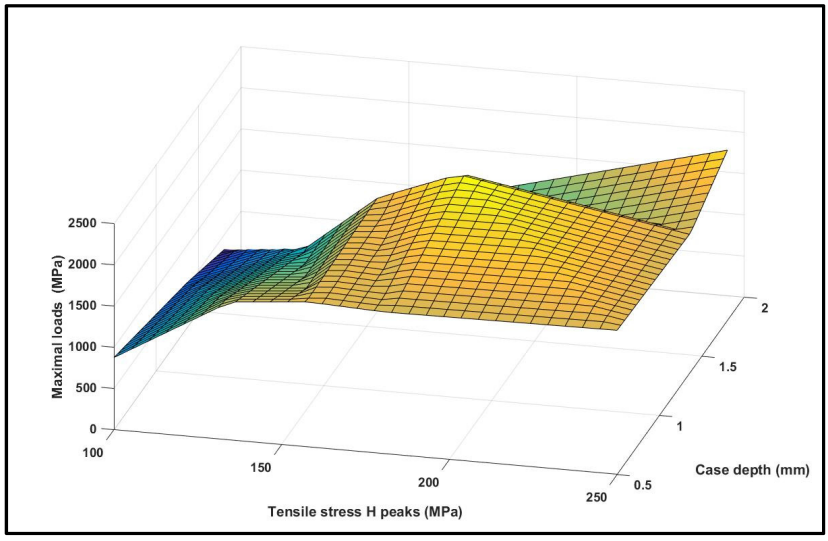

Figure-A VII-1 Maximum loads as a function of tensile hydrostatic stress and case depth thickness

APPENDIX VIII

FLAMANT'S SOLUTION

1. Hypothesis

For an isotropic, homogeneous and elastic material half-space, the stress due a line load of intensity "q" per unit length acting as a circle isobar stress under the contact surface and the polar origin coordinate is the loading point.

2. Equilibrate load

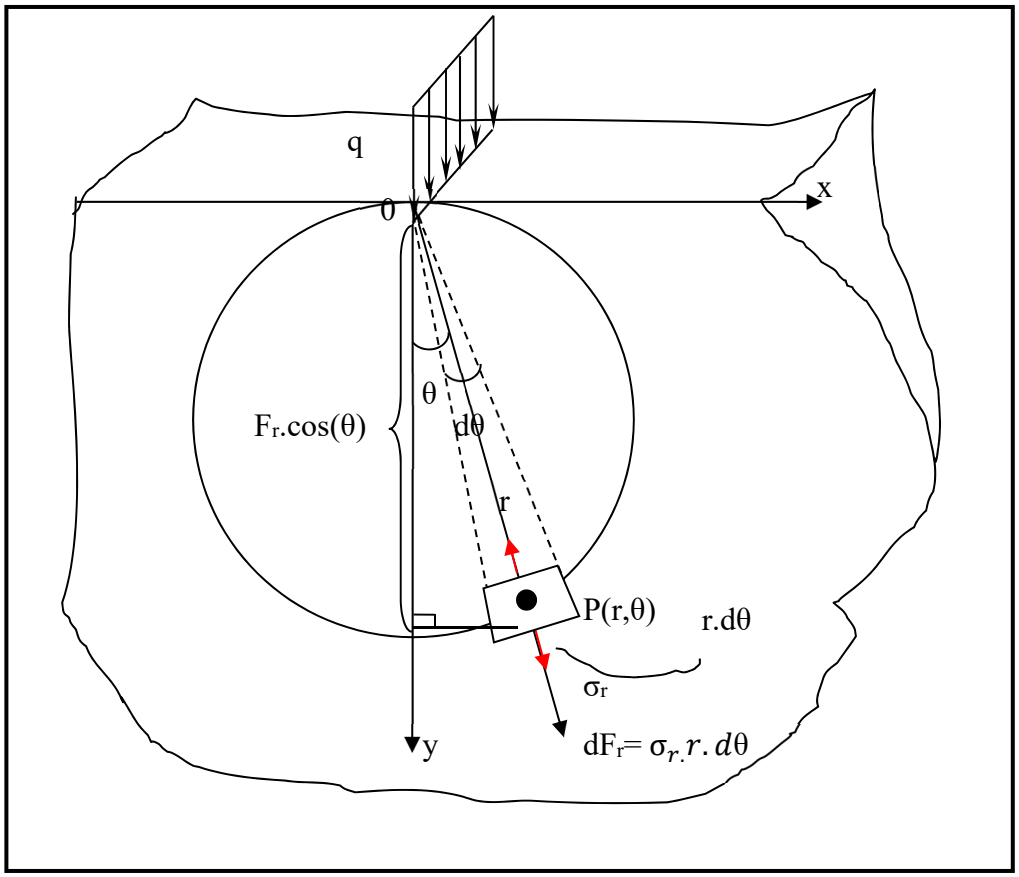

Figure-A VIII-1 Stresses due to a vertical line load in polar coordinate (0, r)

Equilibrate equation by efforts in vertical direction projection

$$\sum Y = 0 \rightarrow q = \int_{-\frac{\pi}{2}}^{\frac{\pi}{2}} F_r.\cos(\theta) = 2\int_0^{\frac{\pi}{2}} \sigma_r.r.\cos(\theta).d\theta \quad (1)$$

3.Stress function in polar coordinate

Stress function in polar coordinate:

$$\Phi = C.r.\theta.\sin(\theta) \quad (2)$$

In the polar coordinate system, the stress distribution in polar coordinate is as follows:

$$\begin{cases} \sigma_r = \frac{1}{r}\frac{\partial\Phi}{\partial r} + \frac{1}{r^2}\frac{\partial^2\Phi}{\partial\theta^2} \\ \sigma_\theta = \frac{\partial^2\Phi}{\partial r^2} \\ \tau_{r\theta} = \frac{1}{r^2}\frac{\partial\Phi}{\partial\theta} - \frac{1}{r}\frac{\partial^2\Phi}{\partial r\partial\theta} \end{cases} \quad (3)$$

with r is radius from polar origin, θ angle is from the y axe to study point, vary from -$\frac{\pi}{2}$ to $\frac{\pi}{2}$ (rad).

$$\frac{\partial\Phi}{\partial r} = C.\theta.sin\theta$$

$$\frac{\partial\Phi}{\partial\theta} = C.r.sin\theta + C.r.\theta.\cos(\theta)$$

$$\frac{\partial^2\Phi}{\partial\theta^2} = C.r.\cos(\theta) + C.r.\cos(\theta) - C.r.\theta.sin(\theta) = C.r.(2.cos(\theta) - \theta.sin(\theta))$$

$$\frac{\partial^2\Phi}{\partial r^2} = 0$$

$$\frac{\partial^2\Phi}{\partial r\partial\theta} = C.sin(\theta) - C.\theta.\cos(\theta) = C.(\sin(\theta) + \theta.\cos(\theta))$$

$$\boxed{\sigma_\theta = \frac{\partial^2\Phi}{\partial r^2} = 0} \quad (4)$$

$$\sigma_r = \frac{1}{r}\frac{\partial\Phi}{\partial r} + \frac{1}{r^2}\frac{\partial^2\Phi}{\partial\theta^2} = \frac{1}{r}.C.\theta.\sin(\theta) + \frac{1}{r^2}.C.r.(2.\cos(\theta) - \theta.\sin(\theta)) = \frac{2.C.\cos(\theta)}{r}$$

$$\boxed{\sigma_r = \frac{2.C.\cos(\theta)}{r}} \quad (5)$$

$$\tau_{r\theta} = \frac{1}{r^2}.C.r.(\theta.\cos(\theta) + \sin(\theta)) - \frac{1}{r}.C.(\sin(\theta) + \theta.\cos(\theta) = 0$$

$$\tau_{r\theta} = 0 \qquad (6)$$

4. Finding the coefficient C of stress function Φ

$$q = 2\int_0^{\frac{\pi}{2}} \frac{2.c.\cos(\theta)}{r}.r.\cos(\theta).d\theta$$

$$q = 2\int_0^{\frac{\pi}{2}} \cos^2(\theta).d\theta$$

With $\cos^2(\theta) = \frac{1}{2}(1+\cos 2\theta)$

$q = 2\int_0^{\frac{\pi}{2}}(1 + cos2\,\theta).d\theta = 2.C.(\theta + \frac{sin2\theta}{2})\Big|_0^{\pi/2} = C.\pi$

$$C = \frac{q}{\pi} \qquad (7)$$

Replace (7) au (2):

$$\Phi = \frac{q}{\pi}.r.\theta.\sin(\theta) \qquad (8)$$

5.Convert the polar coordinate to rectangular coordinate

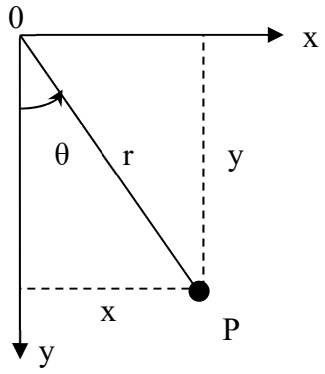

x=r.sinθ

y=r.cosθ

$r^2 = x^2+y^2$ r=$\sqrt{x^2+y^2}$

θ=$tan^{-1}\frac{x}{y}$

$$\begin{cases} \frac{\partial}{\partial x} = \frac{\partial r}{\partial x}\frac{\partial}{\partial r} + \frac{\partial \theta}{\partial x}\frac{\partial}{\partial \theta} \\ \frac{\partial}{\partial y} = \frac{\partial r}{\partial y}\frac{\partial}{\partial r} + \frac{\partial \theta}{\partial y}\frac{\partial}{\partial \theta} \end{cases} \quad (9)$$

$$\frac{\partial r}{\partial x} = \frac{x}{r} \quad (10)$$

$$\frac{\partial \theta}{\partial x} = (\arctan\left(\frac{x}{y}\right)' = \frac{1}{1+\frac{x^2}{y^2}}\left(\frac{x}{y}\right)' = \frac{y}{x^2+y^2} = \frac{r.cos\theta}{r^2} = \frac{cos\theta}{r} \quad (11)$$

$$\frac{\partial r}{\partial y} = \frac{x}{r}cos\theta \quad (12)$$

$$\frac{\partial \theta}{\partial y} = \arctan\left(\frac{x}{y}\right)' = \frac{1}{1+\frac{x^2}{y^2}}\left(\frac{x}{y}\right)'|y \quad = -\frac{x}{x^2+y^2} = -\frac{r.sin\theta}{r^2} \quad (13)$$

$$= -\frac{sin\theta}{r}$$

Introduce the (10), (11), (12), (13) in to (9):

$$\boxed{\begin{cases} \frac{\partial}{\partial x} = \frac{\partial r}{\partial x}\frac{\partial}{\partial r} + \frac{\partial \theta}{\partial x}\frac{\partial}{\partial \theta} = sin\theta\frac{\partial}{\partial r} + \frac{cos\theta}{r}\frac{\partial}{\partial \theta} \\ \frac{\partial}{\partial y} = \frac{\partial r}{\partial y}\frac{\partial}{\partial r} + \frac{\partial \theta}{\partial y}\frac{\partial}{\partial \theta} = cos\theta\frac{\partial}{\partial r} - \frac{sin\theta}{r}\frac{\partial}{\partial \theta} \end{cases}} \quad (14)$$

Stresses distribution in rectangular coordinate:

$$\sigma_x = \frac{\partial^2 \Phi}{\partial y^2} = \frac{\partial}{\partial y}\left(cos\theta\frac{\partial \Phi}{\partial r} - \frac{sin\theta}{r}\frac{\partial \Phi}{\partial \theta}\right) \quad (15)$$

$$\sigma_y = \frac{\partial^2 \Phi}{\partial x^2} = \frac{\partial}{\partial x}\left(sin\theta\frac{\partial \Phi}{\partial r} + \frac{cos\theta}{r}\frac{\partial \Phi}{\partial \theta}\right) \quad (16)$$

$$\tau_{xy} = -\frac{\partial^2 \Phi}{\partial x \partial y} = -\left(cos\theta \frac{\partial \Phi}{\partial r} - \frac{sin\theta}{r}\frac{\partial \Phi}{\partial \theta}\right) \quad (17)$$

$$\frac{\partial \Phi}{\partial r} = \frac{q}{\pi}\theta sin\theta \qquad \text{With } \Phi = \frac{q}{\pi}.r.\theta.\sin(\theta) \quad (18)$$

$$\frac{\partial \Phi}{\partial \theta} = \frac{q}{\pi} r(sin\theta + \theta.cos\theta) \quad (19)$$

$$\sigma_x = \frac{\partial^2 \Phi}{\partial y^2} = \frac{\partial}{\partial y}\left(cos\theta \frac{q}{\pi}\theta sin\theta - \frac{sin\theta}{r}\frac{q}{\pi} r(sin\theta + \theta.cos\theta)\right)$$

$$\sigma_x = \frac{\partial}{\partial y}\left(\frac{q}{\pi}(-sin^2\theta)\right) = cos\theta \frac{\partial(\frac{q}{\pi}(-sin^2\theta))}{\partial r} - \frac{sin\theta}{r}\frac{\partial(\frac{q}{\pi}(-sin^2\theta))}{\partial \theta} = \frac{2q}{\pi r} cos\theta.sin^2\theta$$

$$\boxed{\sigma_x = \sigma_r sin^2\theta} \quad (20)$$

$$\sigma_y = \frac{\partial^2 \Phi}{\partial x^2} = \frac{\partial}{\partial x}\left(sin\theta \frac{q}{\pi}\theta sin\theta + \frac{cos\theta}{r}\frac{q}{\pi} r(sin\theta + \theta.cos\theta)\right)$$

$$\sigma_y = \sigma_r cos^2\theta \quad (21)$$

$$\sigma_y = \frac{2q}{\pi r} cos\theta.cos^2\theta$$

$$\tau_{xy} = -\frac{\partial^2 \Phi}{\partial x \partial y} = -\frac{\partial}{\partial x}\left(cos\theta \frac{\partial \Phi}{\partial r} - \frac{sin\theta}{r}\frac{\partial \Phi}{\partial \theta}\right) = \frac{2q}{\pi r} cos\theta.sin\theta.cos\theta$$

$$\tau_{xy} = \frac{2q}{\pi r} sin\theta \quad (22)$$

6.Results

Stresses due to a line load at surface in rectangular coordinates:

$$\sigma_x = \sigma_r sin^2\theta$$

$$\sigma_y = \sigma_r cos^2\theta$$

$$\tau_{xy} = \frac{2q}{\pi r} sin\theta.cos\theta$$

With $\sigma_r = \frac{2.q.\cos(\theta)}{\pi r}$

$\sin\theta = x/r$

$\cos\theta = y/r$

$r^2 = x^2 + y^2$

$$\sigma_r = \frac{2.q.y}{\pi(x^2 + y^2)^2}$$

$$\sigma_x = \sigma_r sin^2\theta = \frac{2qx^2y}{\pi(x^2+y^2)^2}$$

$$\sigma_y = \sigma_r cos^2\theta = \frac{2qy^3}{\pi(x^2+y^2)^2}$$

$$\tau_{xy} = \frac{2q}{\pi r} sin\theta.cos\theta = \frac{2qxy^2}{\pi(x^2+y^2)^2}$$

LIST OF BIBLIOGRAPHICAL REFERENCES

Abersek B., Flasker J., Glodez S., 2004, "Review of mathematical and experimental models for determination of service life of gears, Engineering Fracture Mechanics 71, p. 439–453.

Akata E., Altinbalik M. T. and Can Y., 2004, "Three-point load application in single tooth bending fatigue test for evaluation of gear blank manufacturing methods", International Journal of Fatigue 26, p. 785-789.

Alban L. E., 1984, "Number 1 Gear failure-tooth bending fatigue", SAE Technical paper series, sept 10-13.

Alban L. E., 1986, "Systematic Analysis of Gear Failures", ASM, Metal Park, Ohio 44073, p. 85-127.

Alfredsson B. and Olsson M., 1998, "Standing contact fatigue", Department of Solid Mechanics, Royal Institute of Technology, KTH, SE-100 44 Stockholm, Sweden.

ANSYS Inc., 2017, "ANSYSVR Academic Research Mechanical, Release 17.2, Help System, ANSYS Mechanical Documentation," ANSYS, Canonsburg, PA.

Antoine J. F., Visa C., Sauvey C., Abba G., 2006, « Approximate Analytical Model for Hertzian Elliptical Contact Problems », Transaction of ASME, Vol.128, July 2006, p.660-664.

Anup S. Pandkar, Nagaraj Arakere, and Ghatu Subhash, 2015, "Ratcheting-based microstructure-sensitive modeling of the cyclic hardening response of case-hardened bearing steels subject to Rolling Contact Fatigue", International Journal of Fatigue, Volume 73, ISSN 0142-1123, p. 119-131.

Baïlon J. P. and Dorlot J. M., 2000, " Des Matériaux", 3ème édition, Presses internationales Polytechnique.

Belfiore N. P., Ianniello F., Natali S., Casadei F., and Stocchi D., 2006, "The development of a feasible method for the Tribological characterization of gear teeth surface treatments", Tribology International 39, p. 789-795.

Bernasconi. A., Davoli. P., Filippini. M., and Foletti. S., 2005, "An Integrated Approach to Rolling Contact Sub-Surface Fatigue Assessment of Railway Wheels," Wear, 258(7–8), p. 973–980.

Bhattacharyya A., Pandkar A., Subhash G., and Arakere N., 2015, "Cyclic Constitutive Response and Effective S–N Diagram of M50 NiL Case-Hardened Bearing Steel

Subjected to Rolling Contact Fatigue", ASME. J. Tribol. 2015;137(4):041102-041102-15. doi:10.1115/1.4030689.

Brewe D. E.,and Hamrock B. J., 1977, "Simplified solution of elliptical contact deformation between two Elastic solids, Journal of Lubrication Tech, 99(4), p.485-487.

Burn D. J., and Parry D. J. S. C., 1964, "Effect of Large Hydrostatic Pressures on the Torsion Fatigue Strength of Two Steels," J. Mech. Eng. Sci., 6(3), p. 293–308.

Cavallaro G. P., Wilks T. P., Subramanian C., Stratford K. N., French P., and Allison J. E., 1995, "Bending fatigue and contact fatigue characteristics of carburized gear", Surface and Coating Technology 71, p. 182-192.

Ciavarella M., Monno F., and Demelio G., 2006, "On the Dang Van Fatigue Limit in Rolling Contact Fatigue," Int. J. Fatigue, 28(8), p. 852–863.

Constantinescu A., Dang Van K., and Maitournam H. M., 2003, "A Unified Approach for High and Low Cycle Fatigue Based on Shakedown Concept," Fatigue Fract. Eng. Mat. Struct., 26(6), p. 561–568.

Coy J. J., and Zaretsky E. V., 1975, "Life Analysis of Helical Gear Sets Using Lundberg-Palmgren Theory," National Aeronautics and Space Administration, Washington, DC, Technical Report No. NASA TN D-8045.

Cram W. D., 1961, "Experimental Load-stress factors", in Handbook of Mechanical Wear, Clipson and live Colwell, eds. Univ. of Mich. Press: Ann Arbor, p. 56-91.

Crehu A. R. D., 2014, "Tribological analysis of White Etching Crack (WEC) failures in Rolling Element Bearings", Ph.D. dissertation, INSA de Lyon, France. http://theses.insa-lyon.fr/publication/2014ISAL0116/these.pdf

Crossland B., 1954, "The Effect of Fluid Pressure on the Shear Properties of Metals," Proc. Inst. Mech. Eng., 168(1), p. 935–946.

Dahlberg J. and Alfredsson B., 2008, "Surface stresses at an axisymmetric asperity in a rolling contact with traction", International Journal of Fatigue (30), p. 1606-1622.

Dang Van K., and Maitournam H. M., 2002, "On Some Recent Trends in Modeling of Contact Fatigue and Wear in Rail," Wear, 253(1–2), p. 219–227.

Denis S., 1997. « Prévision des contraintes résiduelles induites par traitement thermique et thermochimique ». La Revue de Métallurgie-CIT/Science et Génie des Matériaux, Février, p. 157-176.

Denis S., Archambault P., Gautier E., Simon A., and Beck G, 2002, « Prediction of residual stress and distortion of ferrous and non-ferrous metals: current status and future developments ». Journal of Materials Engineering and Performance, vol. 11, no 1, p. 92-102.

Denis S., Zandona M., Mey A., Boufoussi M., and Simon A., 1993, « Calculation of internal stresses during surface heat treatment of steels ». In European Conference on Residual Stresses. (Frankfurt, Germany, 1992): DEM Informationsgesselscaft mbH.), p. 1011-1020.

Desimone H., Bernasconi, A., and Beretta S., 2006, "On the Application of Dang Van Criterion to Rolling Contact Fatigue," Wear, 260(4–5), p. 567–572.

Dudragne. G., Fougeres R., and Theolier M., 1981, "Analysis Method for Both Internal Stresses and Microstructural Effect Under Pure Rolling Fatigue Conditions," ASME J. Lubr. Technol., 103(4), p. 521–525.

Durban C., 1997, « Analyse et optimisation des paramètres influant sur le calcul prévisionnel des contraintes résiduelles conséquentes au chauffage superficiel par induction suivi d'une trempe ». Thèse de doctorat en mécanique, Bordeaux, École Nationale Supérieure d'Arts et Métiers, p- 171.

Ekberg A., Bjarnehed H., and Lunden R., 1995, "A Fatigue Life Model for General Rolling Contact With Application to Wheel/Rail Damage," Fatigue Fract. Eng. Mater. Struct., 18(10), p. 1189–1199.

Ferguson B. L., and Li Z., 2012, "Stress and Deformation During Induction Hardening of Tubular Products," 6th International Quenching and Control of Distortion Conference American Society for Metals, Chicago, IL, Sept. 9–13, p. 34–44.

Fernandes P. J. L., 1997, "Surface contact fatigue failures in gears", Engineering Failure Analysis, Vol.4, No.2, p. 99-107.

Flavenot J. F., and Skalli N., 1984, "A Critical Depth Criterion for the Evaluation of Long-Life Fatigue Strength Under Multiaxial Loading and a Stress Gradient," Fifth European Conference on Fracture (ECF5), Lisbon, Portugal, Sept. 17–21, p. 335–344.

Glaeser W. A., and Shaffer S. J., Battelle Laboratories, 1996, "Contact Fatigue," ASM Handbook, Vol. 19, Fatigue and Fracture ASM Handbook Committee, Materials Park, OH, p. 331–336.

Glodez S., Abersek B., and Flasker J., 2003, "Evolution of the service life of gear in regard to bending fatigue in a gear tooth Root", Trans. Tech. Publications, Switzerland, Key Engineering Materials Vol. 251-252, p. 297-302.

Glodez S., Abersek B., Flasker J., and Ren Z., 2004,“Evaluation of the service life of gears in regard to surface pitting”, Engineering Fracture Mechanics 71, p. 429–438.

Greenwood J. A. and Tripp J. H., 1967, “The Elastic Contact of Rough Spheres”, Journal of Applied Mechanic, p.15 3-159.

Grum J., 2007, “Overview of residual stresses after induction surface hardening”, Int. J. Materials and Product Technology, Vol. 29, Nos. 1-4.

Halme J., and Andersson P., 2009, “Rolling Contact Fatigue and Wear Fundamentals for Rolling Bearing Diagnostics—State of the Art,” Proc. Inst. Mech. Eng. Part J: J. Eng. Tribol., 224(4), p. 377–393.

Harris T. A., and McCool J. I., 1996, “On the Accuracy of Rolling Bearing Fatigue Life Prediction,” ASME J. Tribol., 118(2), p. 297–309.

Harris T. A., and Yu W. K., 1999, “Lundberg-Palmgren Fatigue Theory: Considerations of Failure Stress and Stressed Volume,” ASME J. Tribol., 121(1), p. 85–89.

Hertz H. R., Jones D. E. and Schott G. A., 1881, “On the contact of elastic solids”, chapter 5 and 6, Journal fur die reined und angewandte Mathematik, 92, p. 156-171,.

Hömberg D., Liu Q., Montalvo-Urquizo J., Nadolski D., Petzold T., Schmidt A., and Schulz A., 2016, “Simulation of Multi-Frequency-Induction Hardening Including Phase Transitions and Mechanical Effects,” Finite Elem. Anal. Des., 121, p. 86–100.

Johnson K. L., 2004, Contact Mechanics, Cambridge University Press, Cambridge, UK.

Kadin Y., 2015, “Modeling of Hydrogen Transport in Static and Rolling Contact,” Tribol. Trans., 58(2), p. 260–273.

Kim T. Y., and Kim H. K., 2014, “Three-Dimensional Elastic-Plastic Finite Element Analysis for Wheel-Rail Rolling Contact Fatigue,” Int. J. Eng. Technol., 6(3), p. 1593–1600.

Koibuchi K., Hayama T., and Kawai S., 1982, “Residual stress and fatigue strength of surface hardened components”, Mechanical Engineering Res. Lab, Hitachi Ltd, Tsuchiura, Ibaraki, Japan, ISBN 0080275990, p. 413-419. https://www.shotpeener.com/library/pdf/1981056.pdf

Korsunsky A. M., James K. E., Aylott C. and Shaw B. A., 2003, “Residual stresses in an induction hardened gear tooth mapped by synchrotrons X-ray diffraction”, Journal of Neutron Research, 114, p. 241-245.

Lefebvre D. F., 1989, “Hydrostatic Pressure Effect on Life Prediction in Biaxial Low-Cycle Fatigue,” Biaxial and Multiaxial Fatigue, EGF3, Mechanical Engineering Publications, London, UK, p. 511–533.

Lechun Xie, Palmer D., Otto F., Wang Z., Wang Q. J., 2015, “Effect of Surface Hardening Technique and Case Depth on Rolling Contact Fatigue Behavior of Alloy Steels”, Tribology Transactions, 58:2, p.215-224. DOI: 10.1080/10402004.2014.960957

Lundberg G., and Palmgren A., 1952, “Dynamic Capacity of Roller Bearing,” Acta Polytech. Scand., Mech. Eng. Ser., 2(4), p. 1–52.

Markegård L. and Kristoffersen H., 2006, “Optimized Properties of Car Components – an explanation of how Residual Stress is created during surface hardening”, EFD Induction, www.ivf.se.

Mobasher Moghaddama S., Bomidi J. A. R., Sadeghi F., Weinzapfel N., and Liebel A., 2014, “Effect of Compressive Stresses on Torsional Fatigue,” Tribol. Int., 77, p. 196–200.

Morrison R. A., 1968, “Load/life curves for gear and Cam materials”, Machine Design, v.40, p. 102-108, Aug. 1.

Muro H., Tsushima T., and Nagafuchi M., 1975, “Initiation and Propagation of Surface Cracks in Rolling High Hardness Steel,” Wear, 35(2), p. 261–282.

Nakamura H., “Induction hardening and fatigue strength”, Quarterly reports/Railway Technical Research Institute, Vol. 4, p. 17-27, ISSN 0033-9008, 1960

Nemkov V., Goldstein R., Jackowski J., Ferguson L., and Li Z., 2013, “Stress and distortion evolution during induction case hardening of tube”, J. Mater. Eng. Perform., 22(7), p. 1826–1832.

Nguyen Hoa Ngan, and Bocher Philippe, 2018, “Finite Element Analysis Simulation of the Effect of Induction Hardening on Rolling Contact Fatigue”, Journal of Tribology, ASME, Vol. 140, Issue 6, p. 061404-061404-10.

Nguyen Hoa Ngan, and Beauregard Yvan, 2015, «Analysis of the stress in thread fastener by finite elements to predict the contact damage », In 62nd CASI Aeronautics Conference and AGM 3rd GARDN Conference (Montréal, QC, Canada, May 19-21, 2015) Canadian Aeronautics and Space Institute.

Nicholas T., 1996, “On the use of the Goodman diagram for high cycles fatigue design”, International Journal of fracture 80, p. 219-235.

Norton R. L., 2006, “Machine Design -An Integrated Approach”, Third Edition, Prentice Hall, ISBN 0-13-048190-8.

Palin-Luc T., Coupard D., Dumas C., and Bristiel P., 2011, “Simulation of Multiaxial Fatigue Strength of Steel Component Treated by Surface Induction Hardening and Comparison with Experimental Results,” Int. J. Fatigue, 33(8), p. 1040–1047.

Parrish G., Ingham D. W., and Chaney M., 1998, “The Submerged Induction Hardening of Gears”, Heat Treatment of metals, 2, p. 43-50.

Pazdanowski M., 2014, “Residual Stresses as a Factor of Railroad Rail Fatigue,” Technical Transaction, Civil Engineering, 4-B/2014, p. 39–46. https://suw.biblos.pk.edu.pl/downloadResource&mId¼1231348

Popinceau N. G., Gafitanu M. D., Nastase H., Diaconescu E. N., and Cretu S. S., 1972, “A study of rolling bearing fatigue life with mineral oil lubrication”, Wear, p. 21-48.

Reitinger B., Berer T., Helm O., and Burgholzer P., 2008, “Alteration of the Elastic Properties of Steel and Cast Iron Caused by Hardening,” First International Symposium on Laser Ultrasonic: Science, Technology and Applications, Montreal, QC, Canada, July 16–18.

Romanowicz P., 2017, “Numerical Assessments of Fatigue Load Capacity of Cylindrical Cram Wheel Using Multiaxial High-Cycle Fatigue Criteria,” Arch. Appl. Mech., 87(10), p. 1707–1726.

Rudnev V., Loveless D., Cook R., and Black M., 2003, Handbook of induction heating, 1st edition. Coll. « Manufacturing engineering and materials processing », 61, New York (NY) USA: Marcel Dekker, p. 777.

Sadeghi F., Jalalahmadi B., Slack T. S., Raje N., and Arakere N. K., 2009, “A Review of Rolling Contact Fatigue,” ASME J. Tribol., 131(4), p. 041403.

Savaria V., 2014, “Contraintes Résiduelles Et Leurs Impacts Sur L’amorçage De Fissures En Fatigue De Flexion Dans Des Engrenages Aéronautiques Durcis Superficiellement Par Induction,” PhD. dissertation, Ecole de technologie supérieure, Montréal, QC, Canada.

Savaria V., Florent F., and Bocher P., 2016, “Predicting the Effects of Material Properties Gradient and Residual Stresses on the Bending Fatigue Strength of Induction Hardened Aeronautical Gear,” Int. J. Fatigue, 82, p. 70–84.

Shaw B. A., Aylott C., O’Hara P., and Brimble K., 2003, “The role de constraint residual on the fatigue strength of high performance gearing”, International Journal of Fatigue (25), p. 1279-1283.

Shepelyakovskii K. Z., 1998, “New induction hardening technology”, Advanced materials & Processes 10/98, p. 225-227.

Shipley E. E., 1974, “Failure Modes in Gears,” Gear Manufacture and Performance (Materials/metalworking technology series, Vol. 1), Guichelaar, P. J., Levy, B. S., and Parikh, N. M., eds., American Society for Metals, Metals Park, OH, p.107–135.

Shotter B. A., 1961, “Gear Tooth pitting and fatigue strength”, The Engineer, Technical contributors section, No 24.

Sraml M., and Flasker J., 2007, “Computational approach to contact fatigue damage initiation analysis of gears teeth flanks”, Int. J. Adv. Manuf. Technol. Vol. 31, p. 1066-1075.

Sraml M., Flasker J., and Potrc I., 2003, “Numerical procedure for predicting the rolling contact fatigue crack initiation”, International Journal of Fatigue 25, p. 585–595.

Tallian T. E., 1982, “A Unified Model for Rolling Contact Life Prediction,” ASME J. Lubr. Technol., 104(3), p. 336–346.

Tjernberg A., 2002, « Fatigue lives for induction hardened shafts with subsurface crack initiation ». Engineering Failure Analysis, vol. 9, no 1, p. 45-61.

Townsend D. P., Turza A., and Chaplin M., 1995, “The surface fatigue life of contour induction hardened AISI 1552 Gear”, Army Research Laboratory, NASA, Technical Memoradunm 107017, Technical Report, ARL-TR-808.

Townsend D. P., 1995, “The Surface Fatigue Life of Contour Induction Hardened AISI 1552 Gear,” National Aeronautics and Space Administration, Washington, DC, Technical Report No. ARL-TR-808.

Van Lieshout P. S., Den Besten J. H., and Kaminski M. L., 2017, “Validation of the corrected Dang Van multiaxial fatigue criterion applied to turret bearings of FPSO offloading buoys,” Ships and Offshore Structures Journal (Taylor & Francis), 12(4), p. 521–529.

Yonetani S. and Isoda S., 1989, “Effect of Residual Stress on Fatigue Strength of Induction Hardened Specimens of a Medium Carbon Steel,” Tetsu-to-Hagane (J. Iron Steel Inst. Jpn.), vol. 75, p. 1362–1369.

Zaretsky E. V., Parker R. J., Anderson W. J., and Miller S. T., 1965, “Effect of Component Differential Hardness on Residual Stress and Rolling-Contact Fatigue,” Scientific and Technical Information Division, National Aeronautics and Space Administration, Washington, DC, Technical Report No. NASA TN D-2664.

Zaretsky E. V., Poplawski J. V., and Peters S. M., 1995, “Comparison of Life Theories for Rolling-Element Bearings,” National Aeronautics and Space Administration, Washington, DC, Technical Report No. N95-26774.